UNIVERSIDAD POLITÉCNICA DE MADRID
ESCUELA TÉCNICA SUPERIOR DE INGENIEROS AERONÁUTICOS

THE INTERACTION OF RIBLETS WITH WALL-BOUNDED TURBULENCE

LA INTERACCIÓN DE LOS MICROSURCOS CON LA TURBULENCIA DE PARED

Tesis Doctoral

Ricardo García Mayoral
Ingeniero Aeronáutico

Madrid, Mayo 2011

DEPARTAMENTO DE MOTOPROPULSIÓN Y TERMOFLUIDODINÁMICA
ESCUELA TÉCNICA SUPERIOR DE INGENIEROS AERONÁUTICOS

THE INTERACTION OF RIBLETS WITH WALL-BOUNDED TURBULENCE

LA INTERACCIÓN DE LOS MICROSURCOS CON LA TURBULENCIA DE PARED

Autor
Ricardo García Mayoral
Ingeniero Aeronáutico

Director de Tesis
Javier Jiménez Sendín
Doctor Ingeniero Aeronáutico

Madrid, Mayo 2011

We are all agreed that your theory is crazy.
The question that divides us is whether it is crazy
enough to have a chance of being correct.
N. Bohr

And the colored girls go doo do doo do doo ...
L. Reed

Index

Acknowledgements

As I now stand in front of this finished manuscript, I cannot help but think of those people that have brought me to this point in life. My first thoughts must be for my advisor, Professor Jiménez. I could not express in this small space how deeply I am indebted to him. Through his guidance and example I have learned what a live dedicated to research should be: curiosity, imagination, ambition, enthusiasm, tenacity and critical judgment, non the least towards one's own thinking. Javier has been a scientific father for me, as he was for others before, and will be for more to come. I hope to continue pursuing the standard of excellence that I have learned from him.

I have shared this experience with my colleagues in the Fluid Mechanics Group, who were always keen to support and encourage me, have fruitful discussions, or simply lend a hand when I was stuck. In order of appearance (roughly), they were Juan Carlos, Mark, Oscar, Sergio, Guillem, Samuel, Yoshi, Jorge, Isabel, Álvaro, Pablo, Juan, Ayse, Adrian and Florian. I specially thank Ayse for the careful proofreading of this thesis. The senior members of the Group, Vassilis and Rafa, have generously offered me their advice at all times.

Finally, there are those that have not had a direct implication in this work, but have given me their love and emotional support. They did so even when what they received in return was bad temper and a horrible sense of humour, and in spite of my habit of vanishing from the face of the Earth for months, or even years. I could not have finished this thesis without them. The list would be too long, but some I have already named, and I would like to mention here my parents Luisa and Alfredo in the first place, and also Adriana, Alberto, Amapola, Clara, Dani, David Casas, David Martinez, Diego, Elena, Eva, Fani, Félix, Gloria, Joan, Jose, Laura, Leo, Linda, Lola, Luis, Macarena, Marcos, María, Mariano, Merche, Nuria, Pablo, Roberto, Silvia, and the whole Sagres clan. María made the path with me in the final years and stood by my side through the final frenzy, all the time showing me what a meaningful existence is.

Nomenclature

Mathematical operators

$(\cdot)^+$	Variable in wall-units, normalized using u_τ and ν
$(\cdot)'$	Root mean square of $(\cdot)$
$(\cdot)_{\min}$	Minimum of $(\cdot)$
$(\cdot)_{\max}$	Maximum of $(\cdot)$
$(\cdot)_{\text{opt}}$	Optimum of $(\cdot)$
$\langle(\cdot)\rangle$	Average of $(\cdot)$ in time and in the homogeneous spatial directions
$\langle(\cdot)\rangle_c$	Average of $(\cdot)$ conditioned to the position over the riblet and to the mean direction of the overlying crossflow

Greek symbols

α	Riblet peak angle
δ	Flow thickness, half-width for channels
Δ	Generic increment
Δh	Protrusion height, $\Delta_u - \Delta_w$
Δ_u	Virtual origin of the streamwise flow
Δ_w	Virtual origin of the crossflow
Δx	Grid size in the streamwise direction, in terms of collocation points
Δy	Grid size in the wall-normal direction
Δz	Grid size in the spanwise direction, in terms of collocation points
κ	von Kármán constant
λ_x	Wavelength in the streamwise direction
λ_z	Wavelength in the spanwise direction
ν	Kinematic viscosity
μ_0	Constant of proportionality between the protrusion height Δh^+ and the shift in the velocity profile ΔB

ρ	Density
τ	Shear stress
τ_{uv}	Reynolds stress
τ_{tot}	Total shear stress
τ_{visc}	Viscous stress
τ_w	Kinematic skin friction
τ_{w0}	Kinematic skin friction of the reference smooth wall
ω_x	Vorticity in the streamwise direction

Roman symbols

A_g	Groove cross-section
B	Near-wall intercept and wake component of the mean velocity profile
c_f	Skin friction coefficient, $2/U_\delta^{+2}$
c_{f0}	Skin friction coefficient for the reference smooth channel
C_u	Advection velocity of u-structures
C_v	Advection velocity of v-structures
C_w	Advection velocity of w-structures
CFL	Courant-Friedrichs-Lewy number
CFL_C	Convective CFL number
CFL_V	Viscous CFL number
DR	Drag reduction, $-\Delta\tau_w/\tau_{w0}$
E_{pp}	Spectral density of the pressure fluctuations
E_{uu}	Spectral density of the streamwise velocity
E_{uv}	Spectral density of the Reynolds stress
E_{vv}	Spectral density of the wall-normal velocity
E_{ww}	Spectral density of the spanwise velocity
h	Riblet height, or groove depth
k_x	Wavenumber in the streamwise direction
k_z	Wavenumber in the spanwise direction
L_x	Length of the channel in the streamwise direction
L_y	Width of the channel
L_z	Length of the channel in the spanwise direction
ℓ_g	Square root of groove cross-section
m_ℓ	Viscous drag-reduction slope, when the riblet size is expressed as ℓ_g^+

m_s	Viscous drag-reduction slope, when the riblet size is expressed as s^+
N_r	Number of riblets
N_x	Number of collocation points in the streamwise direction
N_y	Number of collocation points in the wall-normal direction
N_{zc}	Number of collocation points in the spanwise direction for the central block
N_{zr}	Number of collocation points in the spanwise direction for the wall blocks
p	Pressure
p_ℓ, P_x	Mean pressure gradient in the streamwise direction
R	Geometric radius
Re	Reynolds number
Re_τ	Friction Reynolds number, $\mathrm{Re}_\tau = \delta^+$
Re_z	Reynolds number based on the transverse shear, $s^2 S_z/\nu$
s	Riblet spacing
S_x	Uniform shear in the streamwise direction
S_z	Uniform shear in the spanwise direction
t	Time
t_r	Riblet thickness
u	Velocity in the streamwise direction
$\boldsymbol{u}$	Velocity vector containing u, v, and w
u_τ	Friction velocity
U	Mean velocity profile
U_c	Centerline velocity
U_δ	Outer velocity
U_∞	Free-stream velocity
U_0	Mean slip velocity at $y = 0$. For the Taylor–Green vortex flow, initial maximum of the velocity
v	Velocity in the wall-normal direction
w	Velocity in the spanwise direction
x	Streamwise direction
y	Wall-normal direction. In riblet channels, $y = 0$ represents the riblet-peak plane
z	Spanwise direction

Resumen

El propósito de esta tesis es dar respuesta a la pregunta ¿por qué dejan de ser eficaces los microsurcos a partir de un tamaño determinado?

Los microsurcos, *riblets* en inglés, son una rugosidad estriada, alineada en la dirección media del flujo turbulento sobre la superficie, especialmente diseñados para reducir el rozamiento entre ésta y el flujo. Están inspirados en superficies biológicas, como los dentículos ordenados de la piel de los tiburones de gran velocidad, y fueron objeto de un gran número de investigaciones en los años ochenta y noventa. Aunque se comprobó que la reducción de la resistencia depende del tamaño de los microsurcos, escalado en unidades de pared, los mecanismos físicos implicados no se habían explicado completamente hasta ahora. Se comprendía cómo interactúan los microsurcos de tamaño infinitesimal con el flujo turbulento, produciendo un cambio en la resistencia proporcional a su tamaño, pero éste no es el régimen de interés práctico. El comportamiento óptimo se da para tamaños mayores, para los que el comportamiento lineal ya se ha perdido, pero antes de que los microsurcos empiecen a adoptar un carácter de rugosidad común y aumenten la resistencia. Este régimen, que es el más relevante desde el punto de vista tecnológico, ha sido justo el peor comprendido, y hemos centrado nuestro estudio en él. Nuestros esfuerzos han seguido tres direcciones básicas.

En primer lugar, hemos analizado los datos experimentales disponibles, buscando identificar características comunes en el régimen óptimo de las distintas geometrías de microsurcos existentes. Este estudio nos ha llevado a proponer una nueva escala de longitud, la raíz cuadrada de la sección del surco, para sustituir a la tradicional longitud de espaciado entre microsurcos. Escalando las dimensiones de los microsurcos con esta magnitud, el tamaño para el que colapsa el comportamiento lineal se hace prácticamente universal. Ésto sugiere que el comienzo del colapso está relacionado con un valor del área concreto para la sección del surco.

En segundo lugar, hemos realizado un conjunto de simulaciones numéricas directas sobre microsurcos de tamaños que cubren todo el rango de reducción de la resistencia. Así, hemos podido reproducir la transición gradual entre los distintos regímenes. El análisis

espectral de los flujos ha sido particularmente fructífero, ya que ha hecho posible la identificación de rollos transversales justo encima de los microsurcos, que comienzan a aparecer cuando el tamaño de los microsurcos se aproxima al óptimo. Ésta es una característica del flujo bastante sorprendente, no por la singularidad del fenómeno, que ya había sido observado anteriormente para otros tipos de superficies complejas y porosas, sino porque la mayoría de los estudios previos se habían centrado en el detalle del flujo sobre cada microsurco como unidad. La originalidad de nuestro tratamiento ha proporcionado las herramientas adecuadas para capturar estructuras coherentes con un soporte transversal más amplio, que interactúan con los microsurcos no de forma individual, sino colectiva. También hemos comprobado que estas estructuras coherentes son responsables del incremento de la resistencia tras el colapso del régimen viscoso.

Finalmente, hemos analizado la estabilidad del flujo con un modelo simplificado, que vincula la apariencia de los rollos a una inestabilidad de tipo Kelvin–Helmholtz, como sucede también en el flujo sobre doseles vegetales y superficies porosas. A pesar de que el modelo refleja la presencia de microsurcos sólo de forma general y promediada, consigue capturar los atributos esenciales del colapso del régimen viscoso, y proporciona una justificación teórica para el escalado con la sección del surco.

Summary

The purpose of this thesis is to give answer to the question: why do riblets stop working for a certain size?

Riblets are small surface grooves aligned in the mean direction of an overlying turbulent flow, designed specifically to reduce the friction between the flow and the surface. They were inspired by biological surfaces, like the oriented denticles in the skin of fast-swimming sharks, and were the focus of a significant amount of research in the late eighties and nineties. Although it was found that the drag reduction depends on the riblet size scaled in wall units, the physical mechanisms implicated have not been completely understood up to now. It has been explained how riblets of vanishing size interact with the turbulent flow, producing a change in the drag proportional to their size, but that is not the regime of practical interest. The optimum performance is achieved for larger sizes, once that linear behavior has broken down, but before riblets begin adopting the character of regular roughness and increasing drag. This regime, which is the most relevant from a technological perspective, was precisely the less understood, so we have focused on it. Our efforts have followed three basic directions.

First, we have re-assessed the available experimental data, seeking to identify common characteristics in the optimum regime across the different existing riblet geometries. This study has led to the proposal of a new length scale, the square root of the groove cross-section, to substitute the traditional peak-to-peak spacing. Scaling the riblet dimension with this length, the size of breakdown of the linear behavior becomes roughly universal. This suggests that the onset of the breakdown is related to a certain, fixed value of the cross-section of the groove.

Second, we have conducted a set of direct numerical simulations of the turbulent flow over riblets, for sizes spanning the full drag reduction range. We have thus been able to reproduce the gradual transition between the different regimes. The spectral analysis of the flows has proven particularly fruitful, since it has made possible to identify spanwise rollers immediately above the riblets, which begin to appear when the riblet size is close to the optimum. This is a quite surprising feature of the flow, not because of the uniqueness

of the phenomenon, which had been reported before for other types of complex and porous surfaces, but because most previous studies had focused on the detail of the flow above each riblet as a unit. Our novel approach has provided the adequate tools to capture coherent structures with an extended spanwise support, which interact with the riblets not individually, but collectively. We have also proven that those spanwise structures are responsible for the increase in drag past the viscous breakdown.

Finally, we have analyzed the stability of the flow with a simplified model that connects the appearance of rollers to a Kelvin–Helmholtz-like instability, as is the case also for the flow over plant canopies and porous surfaces. In spite of the model emulating the presence of riblets only in an averaged, general fashion, it succeeds to capture the essential attributes of the breakdown, and provides a theoretical justification for the scaling with the groove cross-section.

Chapter 1

Introduction

The present thesis is a study on the interaction of surface geometry manipulations with the overlying turbulent flow, when those manipulations are designed to reduce the drag force that the surface exerts on the flow, constituting a form of passive flow control. Some of the results presented in this thesis have been published in García-Mayoral & Jiménez (2011*b*) and García-Mayoral & Jiménez (2011*a*).

A popular type of surface manipulation is directional roughness, in the form of small two-dimensional protrusions aligned with the flow, which are known as *riblets*. They have been one of the few turbulent-drag-reduction techniques successfully demonstrated not only in theory, but also in practice, both in the laboratory and in full aerodynamic configurations.

Riblets of very different geometries have been tested in wind tunnels, demonstrating drag reductions of the order of 10% over flat plates. Walsh & Lindemann (1984) tested several shapes, including triangular, notched-peak, sinusoidal, and U-shaped riblets, obtaining maximum drag reductions of 7–8% for riblet spacings of approximately 15 wall units. A fairly broad early review was that of Walsh (1990*b*), and more recent ones are those of Choi (2000), who emphasizes the work of the ERCOFTAC drag reduction group, and Bushnell (2003), which is oriented towards drag reduction techniques for aircraft. In his review on turbulent flows over rough walls, Jiménez (2004) viewed drag reduction by riblets as a transitional roughness effect.

Riblet experiments have also been conducted in oil channels, which allow larger riblet dimensions and better control of the geometry, although typically at lower Reynolds numbers and shorter development lengths than wind tunnels. For example, Bechert *et al.* (1997*b*) conducted extensive tests on blade-shaped and trapezoidal-groove riblets, and proposed the latter as a compromise between optimum performance and practical fabri-

cation and maintenance.

Off-design conditions have also been considered. We will discuss the consequences of yaw and tip erosion, but we should mention here the effect of adverse pressure gradients, first reviewed by Walsh (1990*b*). Although that condition is probably not the deciding factor in many practical applications, because the skin friction of adverse-pressure-gradient boundary layers tends to be low, pressure gradients of either sign are present over large areas of most practical configurations, and their effect on riblets remains uncertain. Walsh (1990*b*) found that riblet performance improved under adverse pressure gradients, but mentioned contradictory results by other authors, which he justified by the difficulty of using drag balances under those conditions. Coustols & Savill (1992) summarized the results of several previous investigations, and concluded that the pressure gradients typically found over aircraft wings, whether adverse or favorable, had relatively little effect on the performance of riblets. Later, Debisschop & Nieuwstadt (1996) tested riblets in a wind tunnel with dimensionless adverse pressure gradients an order of magnitude larger than those discussed in Walsh (1990*b*), and found that the maximum drag reduction of triangular riblets could increase from roughly 7% to 13%.

Riblets have been used successfully to reduce the overall drag of airfoils (Lee & Jang, 2005) and aircraft (Viswanath, 2002), with optimum riblet spacings of the order of 30-70 μm. Szodruch (1991) reports on the flight tests of a commercial aeroplane (Airbus 320) with riblets over 70% of its surface, and estimates an overall 2% drag reduction, based on the fuel savings obtained. A summary of those tests, including maintenance and durability issues, can be found in Robert (1992). The discrepancy between the optimum laboratory performance and full configurations is probably to be expected from any method based on the reduction of skin friction. Not all the drag of an aircraft is friction (Roskam, 1987), and much of the latter is distributed over three-dimensional or geometrically complex areas where drag control is difficult to optimize. Note that those limitations might not apply to configurations that are very different from commercial aircraft, such as gliders or other high-performance vehicles.

There is anecdotal evidence of the successful use of riblets in applications other than aircraft, particularly in sporting events in which cost and maintenance considerations are less important than in commercial aviation. The hull of the USA challengers in the America's Cup 1987 and 2010 sailing competitions were fitted with riblets, which had been banned by the regulations in intervening years. Both challengers won the Cup, although it is impossible to determine whether riblets had any real role. Riblets were also used in the 1984 Olympic rowing events, but they were subsequently forbidden in official

racing, together with all other devices that "modify the properties of the boundary layer". Racing swimsuits produced by Speedo, TYR and Arena in the early 2000s also employed riblet patterns on the surface to reduce passive drag in competitive swimming (Krieger, 2004), claiming a drag reduction of up to 4%. Much of that improvement was however most likely due to the reduction of form drag, whose contribution in human swimming is much larger than that of friction (Marinho *et al.*, 2009). Speedo's latest model, the Fastskin LZR Racer, seems to have dropped riblets completely and turned its focus solely on reducing form drag (Matthews, 2008).

A recurrent theme of riblet research has been the motivation by biological surfaces, which are often geometrically complex. Bruse *et al.* (1993) conducted oil channel tests on shark-skin replicas, hairy surfaces based on the ideas of Kramer (1937), and riblets with adjustable geometry, and Bechert *et al.* (1997*a*) reviewed the drag reduction properties of biological surfaces and their replicas. More recently, Itoh *et al.* (2006) tested the flow over seal fur, obtaining drag reductions of up to 12%, with a dependence on mean hair separation similar to that of riblets with s^+. These hairy surfaces exploit the effect of anisotropic porosity, instead of the directional roughness of conventional riblets. The permeability in the streamwise direction generates a slip effect that could in principle reduce friction and even lead to the relaminarization of the flow (Hahn *et al.*, 2002). On the other hand, wall-normal transpiration induces a Kelvin-Helmholtz-related instability that manifests itself in a well defined range of streamwise wavelengths if the transpiration is strong enough (Kong & Schetz, 1982; Jiménez *et al.*, 2001), and that tends to increase drag. If the anisotropy of the porosity results in slip dominating over transpiration, the net effect could be the drag reduction observed in hairy surfaces.

Another approach to the design of riblets attempts to combine the drag reduction properties of riblets with those of spanwise oscillation of the wall (Jung *et al.*, 1992). Viotti *et al.* (2009) suggested that the oscillating effect could also be produced by imposing at the wall a spanwise velocity profile constant in time, but sinusoidal in the streamwise direction. This kind of velocity distribution could be achieved by implementing three-dimensional riblets, with a slight alternative misalignment with the flow, inducing some coherent streamwise-varying spanwise velocity in the vicinity of the wall. Sha *et al.* (2005) measured the drag reduction of zigzag riblets, and Kramer *et al.* (2010) did the same for sinusoidal riblets, but neither achieved results better than those for straight riblets with the same section. The range of oscillation wavelengths and amplitudes tested is however too narrow for that statement to be considered conclusive.

The physical mechanism of the drag reduction by riblets has been investigated in detail,

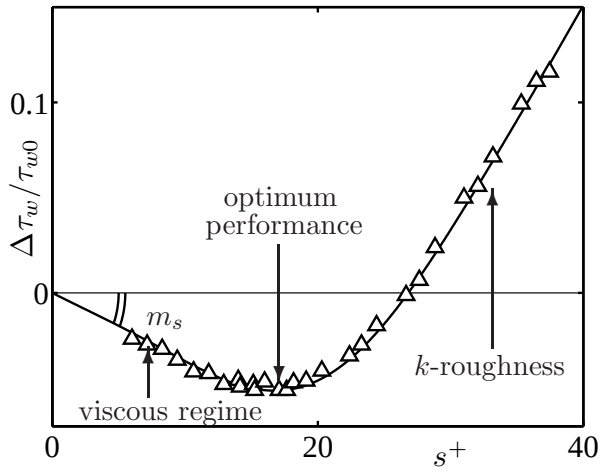

Figure 1.1: Effect of the peak-to-peak distance, s^+, on the skin friction of a triangular riblet with 60° peak sharpness, from Bechert *et al.* (1997*b*).

although some aspects remain controversial. In particular, mean and local velocity profiles and turbulent statistics within and above the riblet grooves have been reported for experiments in wind tunnels (Choi, 1989; Vukoslavcevic *et al.*, 1992; Park & Wallace, 1994; Lee & Lee, 2001), water channels (Suzuki & Kasagi, 1994), and numerical experiments (Choi *et al.*, 1993; Chu & Karniadakis, 1993; Goldstein *et al.*, 1995; Goldstein & Tuan, 1998; El-Samni *et al.*, 2007; García-Mayoral & Jiménez, 2011*b*).

Early in the investigation of riblets, Walsh & Lindemann (1984) showed that the Reynolds number dependence of the effect of a given riblet geometry on the skin friction could be approximately expressed in terms of the riblet dimensions expressed in wall units, $L^+ = Lu_\tau/\nu$, where ν is the kinematic viscosity, and $u_\tau = \sqrt{\tau_w}$ is the friction velocity defined in terms of the kinematic skin friction τ_w. Throughout this thesis the fluid density will be taken as constant and equal to unity. A popular measure of the riblet size L is the groove spacing s, but other dimensions, such as the depth h, have also been used. The dependence of the performance of a particular riblet geometry on the rib spacing is sketched in figure 1.1. We will refer to the limit of very small riblets as the 'viscous' regime, which is formally $s^+ \ll 1$ but in practice $s^+ \lesssim 10 - 15$. In this viscous regime, the reduction in drag is proportional to the riblet size. However, as the riblets get larger and their effect saturates, a minimum drag is reached when the viscous regime 'breaks down,' for an optimum spacing s^+_{opt}. While the viscous limit is fairly well understood and quantified (Bechert & Bartenwerfer, 1989; Luchini *et al.*, 1991), the mechanism of its breakdown has remained controversial, in spite of having been the subject of several studies (Choi *et al.*, 1993; Goldstein & Tuan, 1998). For a given riblet geometry, the spacing

of breakdown limits the optimum performance, so we will attempt to clarify how it is related to that geometry. This clarification may provide the base for the design of surfaces with larger critical sizes than the ones available at present, and consequently with better peak performances.

1.1 The viscous regime

In the viscous regime of small s^+, the contribution of the nonlinear terms to the interaction of the flow with the riblets is negligible and, if τ_{w0} is the skin friction for a smooth wall, the drag reduction $DR = -\Delta\tau_w/\tau_{w0}$ depends linearly on s^+, as mentioned above. The linearity of this regime was recently verified experimentally by Grüneberger & Hage (2011). The regime eventually breaks down for typical spacings $s^+_{\rm opt} \approx 10 - 20$, for which drag reduction is maximum. For even larger riblets, the reduction ultimately becomes a drag increase and follows a typical k-roughness behavior (Jiménez, 2004). The optimum performance of each riblet geometry can roughly be estimated as the product of the breakdown size $s^+_{\rm opt}$ and the slope of the drag curve in the viscous regime,

$$m_s = -\left.\frac{\partial(\Delta\tau_w/\tau_{w0})}{\partial s^+}\right|_{s=0} = -\left.\frac{\Delta\tau_w/\tau_{w0}}{s^+}\right|_{s^+\ll 1}. \tag{1.1}$$

Both m_s and $s^+_{\rm opt}$ depend on the geometry, but the qualitative behavior is always as just described.

The analysis of the available experimental evidence suggests that the viscous and breakdown regimes are essentially unrelated phenomena. For example, blade thickness has a strong effect on the viscous performance of thin-blade riblets without appreciably changing their groove geometry, as shown in figure 1.2(a) for progressively thicker blades (1–4%), with fairly different viscous slopes and very similar breakdown spacings. Conversely, figure 1.2(b) is a compilation of drag curves for riblets with similar m_s but different geometries, whose optimum spacings vary widely. To separate the two effects as much as possible, when focusing on the breakdown mechanism we will often use drag curves normalized so that their initial viscous slopes are unity.

It is widely believed that the drag-reduction properties of riblets in the viscous regime are well described by the concept of 'protrusion height', which was initially introduced by Bechert & Bartenwerfer (1989) as an offset between the virtual origin seen by the mean streamwise flow and some notional mean surface location. The correct form was given by Luchini *et al.* (1991), who defined it as the offset between the virtual origins of the streamwise and spanwise flows. From here on, we will denote the streamwise,

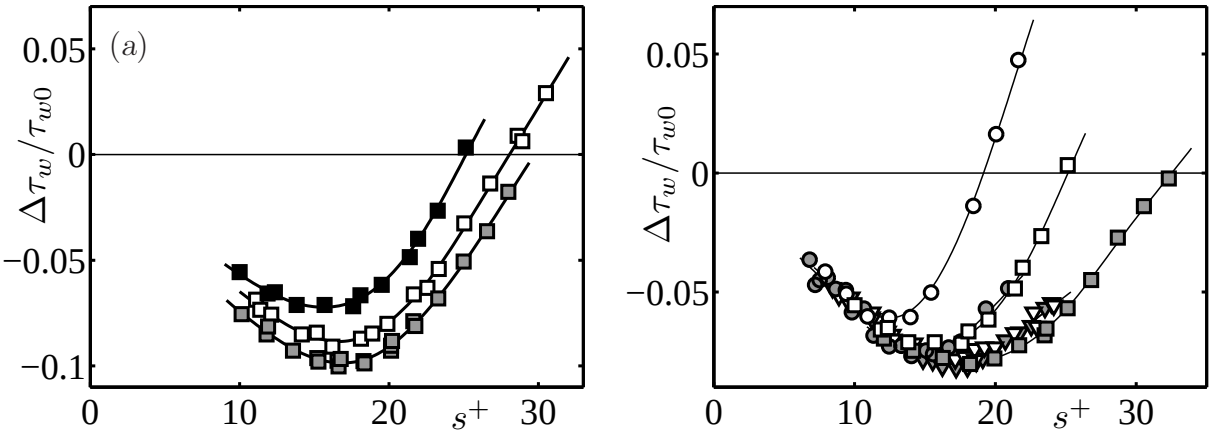

Figure 1.2: Drag reduction curves of various riblets, adapted from Bechert *et al.* (1997*b*). (*a*) Blades with fixed height-to-spacing ratio, $h/s = 0.5$, and different tip width, t/s. ■, $t/s = 0.04$; □, $t/s = 0.01$; ■, $t/s = 0.02$ with improved blade alignment and groove impermeability. (*b*) Riblets with approximately equal viscous slope m_s. ■, blades with $h/s = 0.4$ and $t/s = 0.01$; □, blades with $h/s = 0.5$ and $t/s = 0.04$; ●, scalloped groves with $h/s = 0.7$ and $t/s = 0.015$; ○, scalloped groves with $h/s = 1.0$ and $t/s = 0.018$; ▼, trapezoidal riblets with tip angle 30°; ▽, trapezoidal riblets, 45°.

wall-normal and spanwise coordinates by x, y and z respectively, and the corresponding velocity components by u, v and w. The origin for y will be taken at the top of the riblet tips.

There is a thin near-wall region in turbulent flows over smooth walls where viscous effects are dominant, nonlinear inertial effects can be neglected, and the mean velocity profile is linear. Its thickness is 5–10 wall units (Tennekes & Lumley, 1972). From the point of view of a small protrusion in this layer, the outer flow can be represented as a time-dependent, but otherwise uniform shear. Riblets destroy that uniformity near the wall but, if $s^+ \ll 1$, the flow still behaves as a uniform shear for $y \gg s$. A further simplification is that the problem decouples into two two-dimensional sub-problems in the z–y cross plane, because the equations of motion are locally linear, the riblets are uniform in the streamwise direction, and the outer shear varies only slowly with x when compared to its variations in the cross plane. The first sub-problem is the longitudinal flow of u, driven by a streamwise shear that takes the form

$$u \approx S_x(x,t)\,(y + \Delta_u) \tag{1.2}$$

at $y^+ \gg 1$, and the other is the transverse flow of v and w, driven by

$$w \approx S_z(x,t)\,(y + \Delta_w) \quad \text{and} \quad v \approx 0. \tag{1.3}$$

Far from the wall, the effect of the riblets reduces to the 'virtual origins' Δ_u and Δ_w, which are different for the two flow directions, and are sketched in figure 1.3. What Bechert & Bartenwerfer (1989) and Luchini *et al.* (1991) suggested was that the 'protrusion height' between the two virtual origins, $\Delta h = \Delta_u - \Delta_w$, was the controlling parameter for the viscous drag reduction. Intuitively, if the virtual origin for the crossflow is farther into the flow than the one for the longitudinal one ($\Delta h > 0$), the spanwise flow induced by the overlying streamwise vortices is impeded more severely than over a smooth wall. The vortices are displaced away from the wall, and the turbulent mixing of streamwise momentum is reduced. Since this mixing is responsible for the high local wall shear (Orlandi & Jiménez, 1994), the result is a lower skin friction. This was verified by Jiménez (1994) by direct numerical simulations (DNSs) in which Δh was introduced independently of the presence of riblets.

The numerical calculation of Δh only requires the solution of the two stationary two-dimensional Stokes problems for Δ_u and Δ_w, which are computationally much less intensive than the three-dimensional, time-dependent, turbulent flow over ribbed walls. Note that the linearity of the Stokes problems implies that Δ_u, Δ_w and Δh are all proportional to the riblet size in the viscous regime, as observed in experiments.

1.2 The breakdown of the viscous regime

As s^+ increases, the predictions of the viscous theory break down, particularly the linear dependence on s of the drag. The theories proposed in the literature for this deterioration of performance fall in two broad groups, both of which focus on the behavior of the crossflow.

The first one is that the riblets lose effectiveness once s^+, which is used as a measure of the Reynolds number of the crossflow, increases beyond the Stokes regime. For example, Goldstein & Tuan (1998) suggested that the deterioration is due to the generation of secondary streamwise vorticity over the riblets, as the unsteady crossflow separates and sheds small-scale vortices that create extra dissipation. However, it is known that spanwise oscillations of the wall, which also presumably introduce unsteady streamwise vorticity, can decrease drag (Jung *et al.*, 1992), and that modifying the spanwise boundary condition to inhibit the creation of secondary wall vorticity increases drag (Jiménez, 1992; Jiménez & Pinelli, 1999). Both observations suggest that introducing small-scale streamwise vorticity near the wall decreases drag by damping the larger streamwise vortices of the buffer layer, and that inertial crossflow effects need not be detrimental to drag

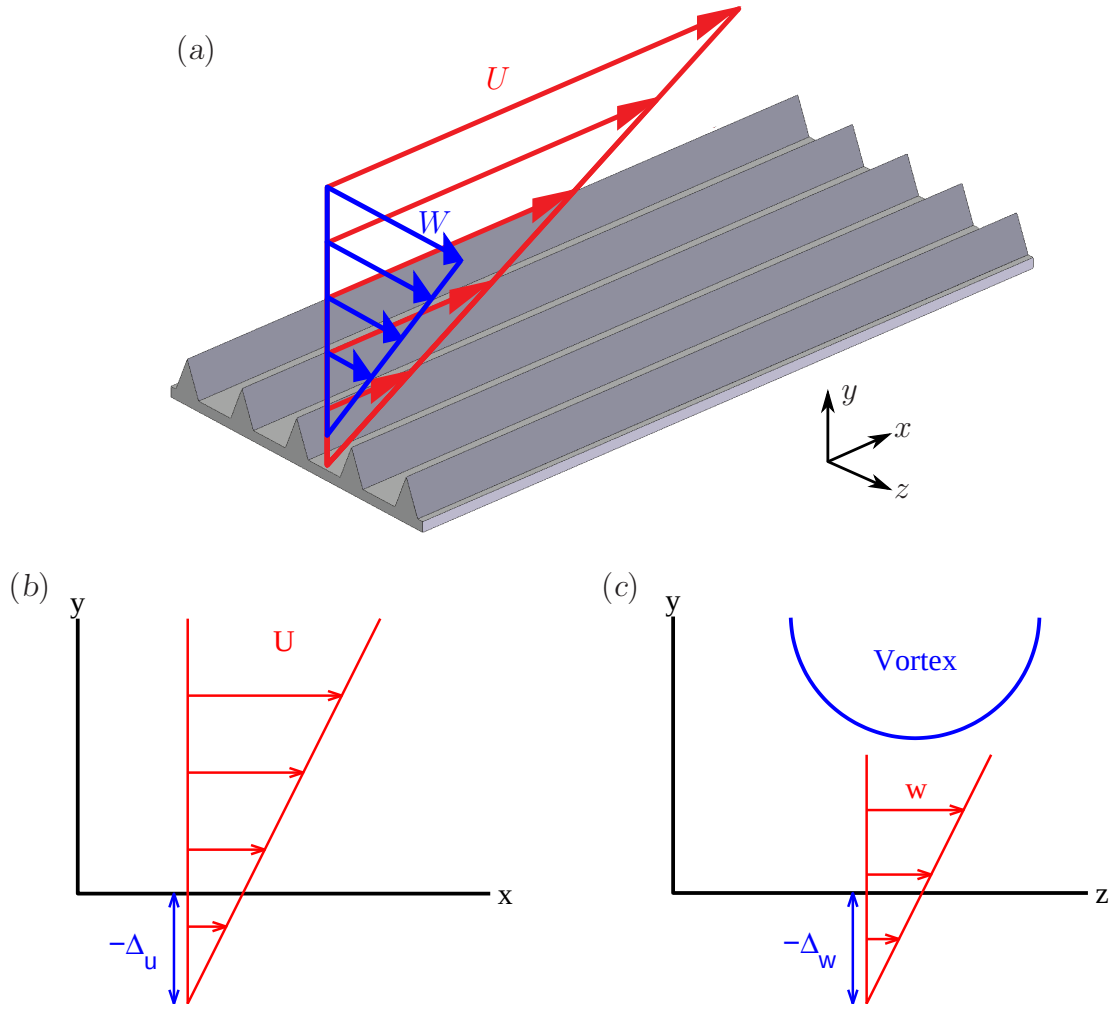

Figure 1.3: Definition of protrusion height $\Delta h = \Delta_u - \Delta_w$ as the offset between the virtual origins of the streamwise and spanwise flows.

reduction.

A related possibility that was considered during the course of the present thesis was that the concept of protrusion height could be extended beyond the strictly viscous regime, and that the observed deviations from linearity would be due to the increased importance of advection in the vicinity of the riblets. In that model, the flow far from the riblets would still be a uniform shear but, within the riblets, it would begin to feel the effects of the finite Reynolds number. If that were the case, the breakdown could still be estimated from simple two-dimensional calculations analogous to the viscous ones.

The second group of theories assumes that the observed optimum spacing is related to the scale of the turbulent structures in the unperturbed turbulent wall region. In that

group we could mention the observations by Choi *et al.* (1993), Suzuki & Kasagi (1994) and Lee & Lee (2001), that the streamwise turbulent vortices lodge within the riblet grooves for riblets in the early drag-degradation regime.

All those models result in optimum spacings of roughly the right order of magnitude, but they can be characterized as 'circumstantial' in the sense that they are based on observations at spacings for which the viscous regime has already broken down, rather than at those close to the deterioration. Moreover, although they suggest plausible reasons for why the Stokes regime fails beyond a certain riblet size, none of them provides convincing physical arguments for why that failure should lead to a drag increase. As a consequence, it is difficult to establish with certainty whether the observed phenomena are consequences or causes of the breakdown, and the ultimate reason for the observed degradation of the effectiveness of riblets has remained until now open.

1.3 Contents and organization of the thesis

Beyond this introduction chapter, the present thesis is organized into another seven. Chapter 2 reviews the existing experimental data on riblets and considers the suitability of the parameters traditionally used to scale the drag-reduction curves, proposing an alternative. Chapter 3 describes the numerical methods that have been used for simulations conducted during the course of the thesis, and provides the validation for those methods. Chapter 4 discusses results of Stokes simulations for the viscous regime, and the inability to explain the viscous breakdown of their extension into the nonlinear regime. Chapter 5 presents results from fully turbulent simulations at $\mathrm{Re}_\tau \approx 180$ for riblet sizes covering all the drag reducing regimes, and also discusses the relationship between the breakdown, the riblet size, and the overlying turbulent flow. Chapter 6 uses results at $\mathrm{Re}_\tau \approx 550$ to analyze the modulation with the Reynolds number of the riblet interaction with the flow. Chapter 7 proposes a linear stability model that captures the essential attributes of the breakdown, including an approximate justification for the size scaling parameter proposed in chapter 2. A chapter of conclusions and recommendations for future work is finally included.

The novel contributions of this thesis to the understanding of the physics of riblet-bounded turbulent flows are essentially contained in chapters 2, 5 and 7, and have been published in García-Mayoral & Jiménez (2011*b*).

Chapter 2

Scaling of drag reduction curves

As mentioned in the introduction, drag reduction curves generally represent the relative change in the wall friction, $DR = -\Delta\tau_w/\tau_{w0}$, as a function of the riblet spacing s^+. We will see in this chapter that neither expressing performance as DR nor the riblet size as s^+ are truly convenient choices. Concerning performance, DR depends, although weakly, on the Reynolds number. This dependence can be eliminated if results are expressed in terms of the shift of the logarithmic profile of the mean velocity, produced by riblets or any other surface manipulation. As for the riblet size, the spacings for the different drag reduction regimes, and particularly the optimum $s^+_{\rm opt}$, depend heavily on the particular riblet geometry. We will inquire whether it is possible to express the riblet size in terms of some other dimension, for which that geometry dependence is eliminated, or at least reduced.

2.1 Scaling of drag reduction with the shift of the logarithmic profile

The dependence of the drag reduction on the Reynolds number Re cannot be completely described by the variation of s^+ as depicted in figure 1.1. According to the classical theory of wall turbulence, surface manipulations only modify the intercept of the logarithmic velocity profile, while both the Kármán constant, $\kappa \approx 0.4$, and the 'wake' function are unaffected (Clauser, 1956). The free-stream velocity, U_δ, can be expressed as

$$U^+_\delta = \left(\frac{2}{c_f}\right)^{1/2} = \kappa^{-1}\log\delta^+ + B, \tag{2.1}$$

where $\delta^+ = {\rm Re}_\tau$ is the flow thickness in wall units, and B includes both the near-wall intercept and the contribution from the wake component. We will favor the notation ${\rm Re}_\tau$

when the intention is to characterize the turbulence of the flow, and δ^+ when implying a length scale, although both refer to the same quantity. Notice that the friction coefficient is defined as $c_f = 2\tau_w/U_\delta^2 = 2/U_\delta^{+2}$. We will use δ loosely to refer to the flow thickness, and when referring to our results it will always represent the channel half-width. In the same way, U_δ will be the mean velocity at the central plane of the channel, instead of the bulk velocity, to obtain friction coefficients whose definition resembles as closely as possible those in boundary layers, which are scaled with the free-stream velocity.

The main effect of a given ribbed surface is to change B (Choi, 1989), which is equivalent to the 'roughness function' used to characterize rough surfaces (Jiménez, 2004), but the resulting change of c_f also depends on the Reynolds number δ^+. For constant U_δ and small relative variations of the friction coefficient, it follows from (2.1) that

$$\frac{\Delta c_f}{c_{f0}} = \frac{\Delta \tau_w}{\tau_{w0}} = -\frac{\Delta B}{(2c_{f0})^{-1/2} + (2\kappa)^{-1}}, \tag{2.2}$$

where the first term in the denominator is due to the change of u_τ in U_δ^+, and the second one comes from the corresponding change in δ^+. If ΔB is positive, the logarithmic profile is shifted 'upwards' and friction is reduced, and *vice versa*. The classical theory of wall-turbulence suggests that the effect of riblets, at least if they are small with respect to δ, should be confined to the near-wall layer, and that any change in B should only depend on geometrical quantities scaled in wall units. It follows from (2.2) that, for a given ΔB, the drag reduction of any riblet will change with c_{f0}, even if s^+ remains constant. The c_{f0} weak $\mathrm{Re}^{-1/4}$ dependence (Dean, 1978) should be expected to have an impact on performance, so that DR curves for a given riblet at different Re were not equal, but proportional to each other. Therefore, comparison between measurements at different Reynolds numbers should be done in terms of the roughness function ΔB, not of $\Delta\tau_w/\tau_{w0}$, and the same is true when reducing experimental data to aeronautical applications (Spalart & McLean, 2011). For instance, the experiments of Walsh & Lindemann (1984) and Walsh (1990*b*) were conducted on boundary layers in a wind tunnel, at $c_f = 3.5 - 4 \times 10^{-3}$, while Bechert *et al.* (1997*b*) conducted theirs in an oil channel at lower Reynolds numbers, $c_f = 5.5 - 7.5 \times 10^{-3}$. For the same geometry, we could therefore expect the performance of Walsh's riblets to be about 20% worse than Bechert's.

The relation between ΔB and DR can in turn be used to obtain an expression relating the viscous slope m_s to the protrusion height $\Delta h/s$. Because of the linearity of the viscous regime, for small s^+ the change ΔB should be proportional to the protrusion height Δh^+,

$$\Delta B = \mu_0 \Delta h^+, \tag{2.3}$$

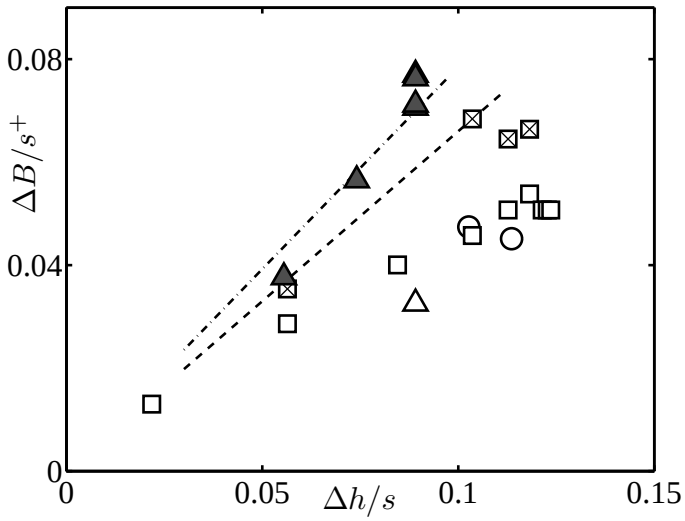

Figure 2.1: Experimental values of the viscous slope, as a function of the theoretical protrusion height. △, triangular riblets; ▽, notched top and flat valley riblets; ○, scalloped semicircular grooves; □, blade riblets. The solid symbols are results from Walsh & Lindemann (1984) and Walsh (1990*b*), and the open ones results from Bechert *et al.* (1997*b*). ----, line with slope $\mu_0 = 0.66$; –·– , $\mu_0 = 0.785$.

with a universal coefficient μ_0. That was tested by Jiménez (1994), who performed direct simulations of channels in which the protrusion effect was modeled independently of the presence of actual riblets, using the active control approach of Choi *et al.* (1994). His results were consistent with

$$\Delta B \approx 0.66 \Delta h^+, \tag{2.4}$$

which agrees well with a rapid-distortion model also in Jiménez (1994). The coefficient should nevertheless be treated with care, because of the very low Reynolds numbers at which the numerical experiments were conducted. Alternatively, Bechert *et al.* (1997*b*) proposed a simplified model that assumes a uniform translation of the viscous-sublayer velocity profile, according to which

$$\Delta B \approx 0.785 \Delta h^+. \tag{2.5}$$

The coefficients in (2.4) and (2.5) are too similar to determine from experimental data which one represents reality more accurately, but at any rate the viscous performance of the riblets would be given by

$$\Delta B|_{s^+ \ll 1} = \left(\mu_0 \frac{\Delta h}{s} \right) s^+. \tag{2.6}$$

Using (2.6), the coefficients in (2.4) and (2.5) are tested in figure 2.1 against the experiments of Walsh & Lindemann (1984), Walsh (1990*b*) and Bechert *et al.* (1997*b*).

However, the experimental scatter is too large to distinguish between the two coefficients, or even to decide on the applicability of (2.3). At least some of the scatter is due to experimental artifacts like the very different development lengths of the two set-ups. While Walsh's surfaces were covered with riblets over relatively large areas, and his boundary layers could be assumed to be at equilibrium, Bechert used relatively small patches of the order of a single boundary layer thickness. The effect on a boundary layer of a step change in the wall roughness was reviewed in Smits & Wood (1985). They concluded that the relaxation to the new equilibrium takes about 10–20 boundary layer thicknesses. Even perturbing the whole logarithmic layer requires $5 - 6\delta$. The effect of Bechert's riblets was therefore likely restricted to the near-wall region, suggesting that the second summand in the denominator of (2.2) should probably not be included when reducing them to ΔB. Another source of uncertainty is the different level of geometric control. The lower Reynolds number of Bechert's experiments meant that he could obtain optimum drag reductions for riblet spacings of the order of 5 mm, while the equivalent dimensions in Walsh & Lindemann (1984) and Walsh (1990*a*) were an order of magnitude smaller. The small sizes in Walsh's experiments led to relatively large machining defects, which, together with the smaller precision of his drag balance, is the cause of a larger scatter of his results when compared to those of Bechert. Nevertheless, the lesser geometric control was not always in the expected direction. For example, the open squares in figure 2.1 are blade riblets from Bechert *et al.* (1997*b*). Those with crosses were mounted on a different base than those without them, and they agree better with the theory. Bechert noted the discrepancy, and repeated a few experiments after sealing the riblet base, increasing the drag reduction by about one fifth (an example can be seen in figure 1.2(*a*)). Similar caveats apply to the other riblets in figure 2.1, including those that appear to agree with the theory.

However, if we believe the theoretical predictions in spite of the experimental ambiguities, (2.3) and (2.2) can be combined in a formula for the viscous drag-reduction slope m_s that only depends on Stokes calculations and the value of c_{f0},

$$m_s = \frac{\mu_0}{(2c_{f0})^{-1/2} + (2\kappa)^{-1}} \frac{\Delta h}{s}. \tag{2.7}$$

This equation can be used to convert, for any given riblet geometry, the theoretical protrusion height into the performance-relevant drag-reduction slope. The influence of the Reynolds number on riblet performance should be restricted to the change in c_{f0} in the denominator. As mentioned above, this influence can be eliminated by expressing the drag change in terms of ΔB, but alternatively it can be eliminated by expressing results

in terms of DR/m_s,

$$\frac{DR}{m_s} = \frac{\Delta B}{\mu_0 \left(\Delta h/s\right)}, \tag{2.8}$$

which in addition absorbs the dependence on the viscous performance of the particular riblet geometry, expressed through $\Delta h/s$.

2.2 Scaling of the riblet size of viscous breakdown

Historically, riblet size in drag curves has been expressed in terms of the spacing s^+. This choice captures the collapse of different experiments for each specific riblet geometry, so for instance the optimum performance is always obtained for a fixed $s^+_{\rm opt}$. However, the use of s^+ offers no particular advantage over other geometric parameters, such as for instance the groove depth h^+, which has also sometimes been used. In an attempt to identify what aspect of the riblet geometry is important for the viscous breakdown, we have investigated whether it was possible to find a different scale for the riblet dimension, for which the scatter of the frequently used $s^+_{\rm opt} \approx 15 \pm 5$ was substantially reduced, so the breakdown took place for an approximately fixed length value, common to any riblet shape. Figure 2.2(a) illustrates the variation of $s^+_{\rm opt}$ from one geometry to another. The figure portrays the optimum spacing for several experimental riblets against the ratio of the groove cross-section to the square of the spacing, A_g/s^2, which is a rough measure of the depth-to-width ratio of the groove. Although $s^+_{\rm opt}$ is always in the range $10-20$ mentioned above, it is clear that deeper grooves break down earlier, and achieve their optimum performance for narrower spacings. Note that this effect cannot be explained by any of the breakdown models discussed in §1.2. For example, the lodging of buffer layer vortices within the riblet grooves might qualitatively explain why the drag reduction breaks down for riblet spacings of the order of the vortex diameters, about 20 wall units according to Kim *et al.* (1987), but it does not explain why the groove depth affects $s^+_{\rm opt}$. A successful alternative should predict the location of the viscous breakdown and collapse as much as possible the different regimes in the experimental drag curves, at least for sizes not much larger than the optimum.

An empirical, non-exhaustive search among possible length scales for the riblet size gave as a result that the one that best captures the influence of both the riblet spacing and the groove shape is the square root of the groove cross-section, $\ell_g^+ = \sqrt{A_g^+}$. We portray in figures 2.2(b)–2.2(e) the histograms of the breakdown size for several riblets, expressed in terms of s^+, h^+, $\sqrt{s^+h^+}$, and ℓ_g^+. We have omitted experiments for which the optimum performance could not be clearly defined, such as the measurements for fibers

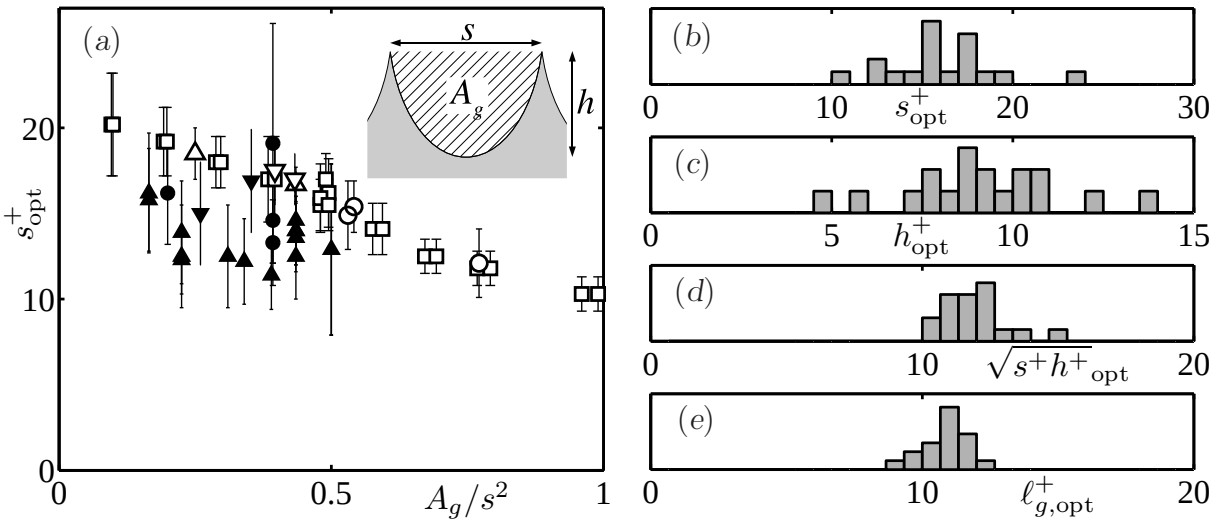

Figure 2.2: (*a*) Riblet spacing for maximum drag reduction, as a function of the relative groove cross-section A_g/s^2. The symbols are the same as in figure 2.1. Error bars have been estimated from the drag measurement errors given in the references. (*b–e*) Histograms of the optimum performance point, expressed in terms of the peak-to-peak spacing s, the groove depth h, their combination $\sqrt{sh}$, and the square root of the groove cross-section, $\ell_g = \sqrt{A_g}$. For several riblet geometries.

of Bruse *et al.* (1993), or those for seal fur of Itoh *et al.* (2006). Disregarding them, the histograms show that the optimum values of s^+ and h^+ have scatters of the order of 40%, while the scatter for ℓ_g^+ is only about 10%. The implied optimum is $\ell^+_{g,\rm opt} \approx L^+_{\rm opt} \pm 1$, with $L^+_{\rm opt} = 10.7$.

Scaling the whole drag-reduction curves requires both normalizing the riblet size with ℓ_g^+, and scaling the drag reduction with a redefined viscous slope m_ℓ,

$$m_\ell = -\left.\frac{\Delta\tau_w/\tau_{w0}}{\ell_g^+}\right|_{\ell_g^+\ll 1} = \frac{s}{\ell_g} m_s, \tag{2.9}$$

so that $DR = m_\ell \ell_g^+$ in the viscous regime, with the implication that DR/m_ℓ should be a 'universal' function of ℓ_g^+ in the full drag reducing range. Note that m_ℓ is a viscous quantity that can be computed from Stokes two-dimensional simulations, using the expression

$$m_\ell = \frac{\mu_0}{(2c_{f0})^{-1/2} + (2\kappa)^{-1}} \frac{\Delta h}{\ell_g}. \tag{2.10}$$

In practice, m_ℓ is often estimated directly from the experimental results for the smallest riblets, because of the uncertainty about the real geometry details like tip-rounding, which greatly affects the viscous performance.

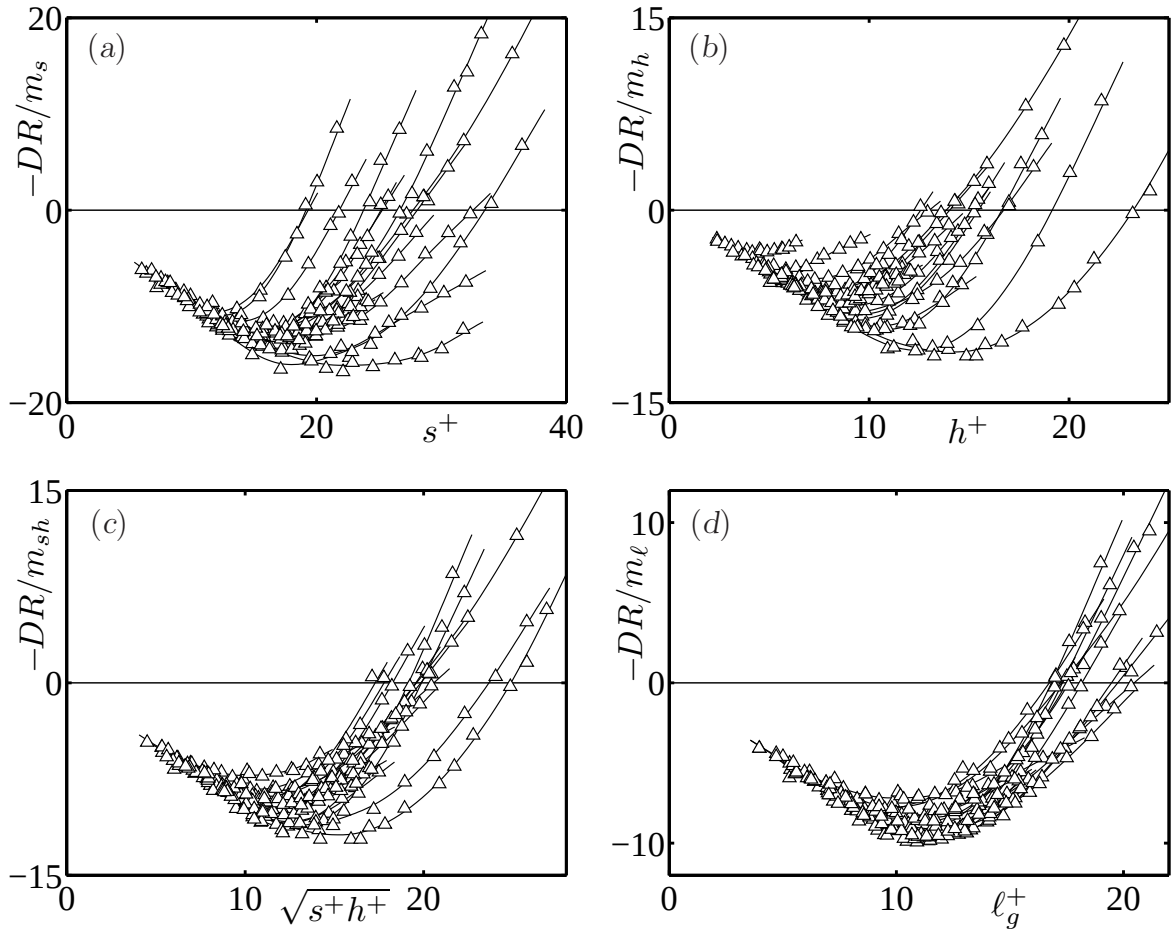

Figure 2.3: Drag reduction curves for several riblet geometries from Bechert *et al.* (1997*b*), reduced to a common viscous slope, as functions of (*a*) s^+, (*b*) h^+, (*c*) $\sqrt{s^+h^+}$, and (*d*) ℓ_g^+.

For s^+, h^+, and $\sqrt{s^+h^+}$, the analogous slopes m_s, m_h, and m_{sh} can be defined, and the influence of the viscous regime on the drag-reduction curve should, in principle, be limited to their values. In particular, since our interest is mostly on the riblet size at breakdown, we will generally use drag curves normalized with the viscous slopes, computed either directly from Stokes calculations or from the experiments, as proposed at the end of §2.1. This leaves out phenomena directly connected with the properties of riblets in the viscous regime that do not influence the mechanism of breakdown, such as the effect of tip rounding (Walsh & Lindemann, 1984; García-Mayoral & Jiménez, 2011*a*), which decreases the viscous slope but does not seem to modify the size for maximum performance. Note that the normalization does not modify the location of the optimum drag reduction, but that it simplifies its identification by removing the influence of all the other scaling parameters. This is done in figure 2.3 for a variety of riblet geometries and

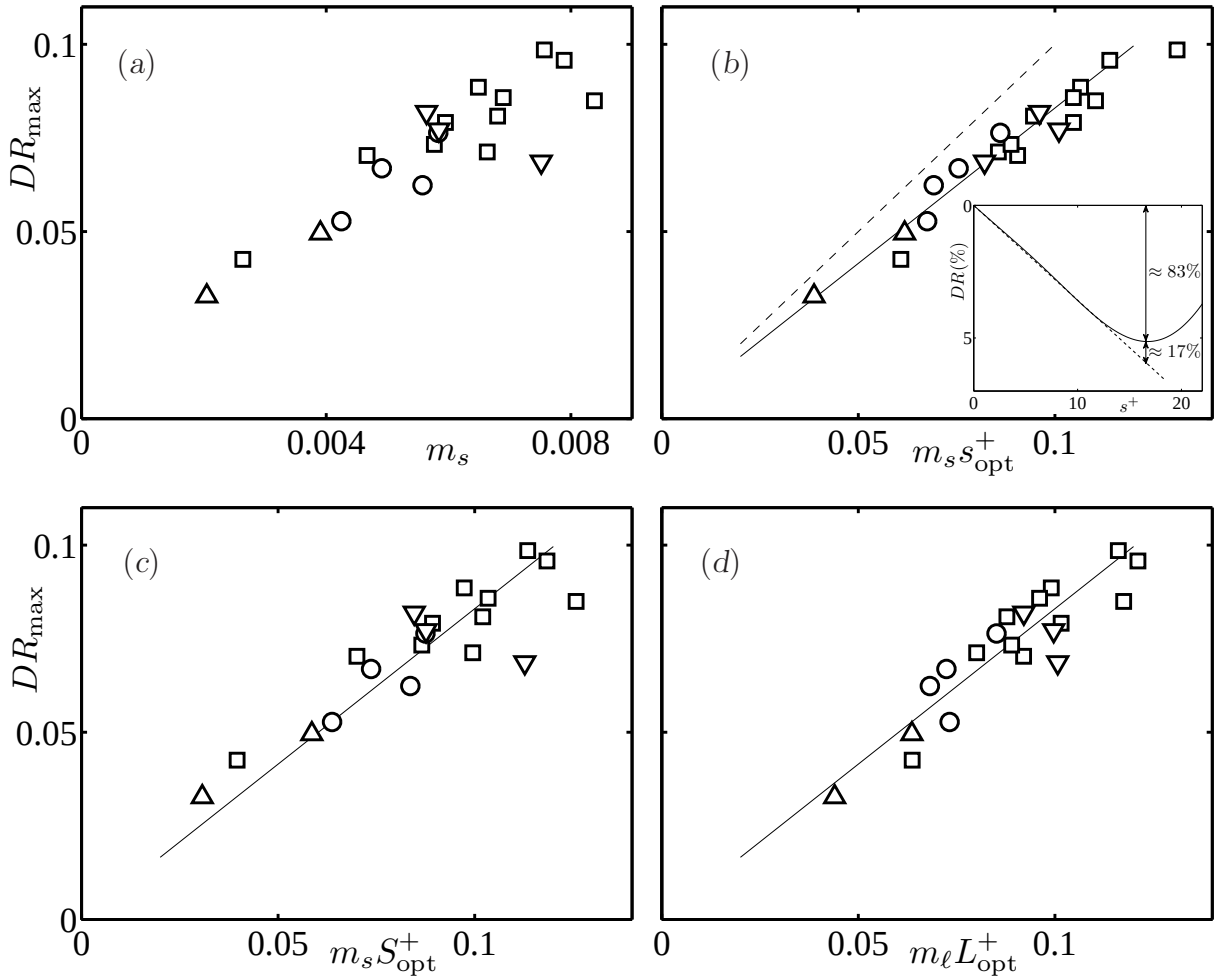

Figure 2.4: Values of $DR_{\max}$ compared with the predictions obtained using the values of the viscous slopes. (*a*) Direct comparison with m_s. (*b*) Comparison between actual values of $DR_{\max}$, represented by symbols, and those estimated by the extrapolation of the viscous regime into the optimum size, represented by the dashed line; the solid line is a linear fit with slope 0.83, and the inserted sketch illustrates how the real $DR_{\max}$ is roughly 0.83 times the result of the direct extrapolation. The last two panels are comparisons of $DR_{\max}$ with viscous estimates assuming (*c*) $s^+_{\rm opt} \approx S^+_{\rm opt} = 15$, and (*d*) $\ell^+_{g,\rm opt} \approx L^+_{\rm opt} = 10.7$. The symbols are the same as in figure 2.1.

for four different size measures, and it is clear that ℓ_g^+ provides the best collapse.

The scaling with ℓ_g^+ poses a significant advantage as a tool for engineering predictions, since it enables the estimation of $DR_{\max}$ with reasonable accuracy solely from viscous regime results, as evidenced in figure 2.4. The first panel portrays the optimum performance compared with the conventional viscous slope m_s, and shows that both quantities are only weakly correlated. An accurate estimation of $DR_{\max}$ would not only require

the value of m_s, but also the determination of the optimum spacing $s^+_{\rm opt}$. Figure 2.4(b) shows that $DR_{\rm max}$ is slightly lower than what would result from the direct extrapolation from the viscous regime into the optimum size, $DR_{\rm max} \approx m_s s^+_{\rm opt}$, but the difference is roughly geometry-independent, and the actual value of $DR_{\rm max}$ turns out to be roughly 83% of the result of that extrapolation, $DR_{\rm max} \approx 0.83 m_s s^+_{\rm opt}$. However, the latter expression is of little use for geometries that have not yet been tested in the laboratory, for which m_s could be estimated *a priori* but $s^+_{\rm opt}$ would need to be measured, with the only available estimate being the average $s^+_{\rm opt} \approx S^+_{\rm opt} = 15$ often mentioned in the literature. Figure 2.4(c) shows that the resulting estimate for the optimum performance, $DR_{\rm max} \approx 0.83\ m_s\, S^+_{\rm opt} = 12.45\ m_s$, can be quite inaccurate, obviously showing the same scatter as figure 2.4(a). On the other hand, the scaling with ℓ_g^+ leads to the estimate

$$DR_{\rm max} \approx 0.83\ m_\ell\, L^+_{\rm opt} = 8.9\ m_\ell, \tag{2.11}$$

shown in panel (d), which provides a better collapse.

Equation (2.11) can provide a reasonable estimate for $DR_{\rm max}$ from the value of the viscous slope m_ℓ only, which in turn can be calculated from Stokes computations for the protrusion height $\Delta h/\ell_g^+$ using (2.10). The approximation of (2.11) is quite accurate for conventional riblets, even for depth-to-width ratios as low as 0.2, with a scatter below 20%.

In spite of the good collapse of figures 2.3(d) and 2.4(d), it should be stressed that ℓ_g^+ may not be an adequate parameter to characterize the performance of unconventional geometries, such as the fibers and seal fur mentioned above, for which A_g is difficult to define, or the T-shaped riblets cited by Walsh (1990*b*). Taking the latter as example, it is clear that, as the wall-parallel segments of the T-fences widen and close into each other, the grooves become increasingly isolated from the overlying flow, while still maintaining the same ℓ_g^+. In the limit of fully sealed grooves, the geometry would behave as a flat surface, and modifying ℓ_g^+ would have no performance impact. The present rule can only be considered an empirical approximation, valid for geometries that are not too different from the experimental 'conventional' riblets –the triangular, trapezoidal, blade, and scalloped riblets frequently proposed in the literature, in which a groove fully exposed to the outer flow can clearly be defined.

It is therefore important to understand the nature of the viscous breakdown, to clarify the reason for the present collapse, and to find whether it can be extended to other geometries, either using ℓ_g^+ or other related parameter. For that purpose, we have conducted the DNS experiments described in chapters 5 and 6.

Chapter 3

Numerical methods

In this chapter we detail the numerical algorithms used in the present thesis to simulate the flow over riblets. A first family of methods, designed for two-dimensional flows, is used to obtain the protrusion height results presented in chapters 4 and 7. A second family is used for the DNS of fully-turbulent, three-dimensional flows. The results of those simulations are discussed in chapters 5 and 6. Validation test-cases are provided for both the two-dimensional and three-dimensional algorithms at the end of the present chapter.

3.1 Numerical methods for the calculation of two-dimensional flows over riblets

3.1.1 Flow driven by uniform shear

The purpose of this code is to simulate the flow over a ribbed surface with peak-to-peak distance s, under conditions of uniform shear given by equations (1.2) and (1.3) far from the wall. There is no mean pressure gradient along either x or z and, as discussed in §1.1, we neglect all the streamwise derivatives. Under those conditions the problem decouples into an equation for the streamwise velocity, and another one for the cross-flow, both of which involve only the $y-z$ plane. There are no convective terms involving u in the momentum equations for v and w, and the velocity scales for u and for the transverse velocities can be chosen independently. We assume constant density $\rho = 1$, and scale all the lengths with the riblet spacing s. The streamwise velocity u scales with sS_x, and the crossflow velocities v and w with sS_z. The pressure fluctuations scale with $\rho(sS_z)^2$. The flow is assumed periodic in z with wavelength s. A few simulations were done in boxes

including two riblets, to check the possibility of subharmonic bifurcations, but none were found. Although the solutions obtained are stationary, that character is not assumed *a priori*, and the crossflow could in principle shed unsteady vorticity for high enough Reynolds numbers.

Under those conditions, the non-dimensional Navier–Stokes equations are

$$\nabla \cdot \boldsymbol{u} = 0, \tag{3.1}$$

$$\frac{\partial \boldsymbol{u}}{\partial t} + \boldsymbol{u} \cdot \nabla \boldsymbol{u} = -\nabla p + \frac{\nu}{s^2 S_z} \nabla^2 \boldsymbol{u}, \tag{3.2}$$

where all the differential operators are restricted to the $z - y$ plane. The boundary conditions are

$$\left.\frac{\partial u}{\partial y}\right|_{y\to\infty} = 1, \qquad v|_{y\to\infty} = 0, \qquad \left.\frac{\partial w}{\partial y}\right|_{y\to\infty} = 1, \tag{3.3}$$

and no slip at the riblet surface.

The only flow parameter is the transverse Reynolds number, $\mathrm{Re}_z = s^2 S_z/\nu$, which is the square of the riblet spacing expressed in wall units based on the spanwise shear, s_z^+. At the wall, the spanwise shear is the streamwise vorticity, whose typical root mean square value is $\omega_x' \approx 0.25 \langle S_x \rangle$ (Kim *et al.*, 1987), providing an estimate $S_z \approx 0.25\, S_x$. For riblets of size past the viscous regime, $s^+ \approx 10 - 20$, it follows that

$$\mathrm{Re}_z \approx S_z^+ \, {s^+}^2 \approx 0.25 \, {s^+}^2 = 25 - 100, \quad \text{or} \quad s_z^+ = 5 - 10. \tag{3.4}$$

We have studied both the Stokes limit, $\mathrm{Re}_z = 0$, and non-zero Reynolds numbers in the range given by (3.4). Since the purpose of the latter simulations is to check the possibility of a two-dimensional mechanism for nonlinearity as mentioned in §1.2, the test would be whether the protrusion height degrades significantly within this range of Reynolds numbers.

The boundary conditions of uniform shear at $y \to \infty$ are numerically imposed far enough from the riblet surface for the flow to have reached uniformity. Depending on the riblet geometry, a distance between $0.8\, s$ and $1.7\, s$ above the riblet peaks proved to be sufficient in our simulations.

At the riblet surface, given the complexity and diversity of the riblet geometries investigated, we have chosen to impose the no-slip condition using an immersed-boundary technique, first proposed by Peskin (1972). This choice allows us to use a Cartesian uniform grid, and to simulate different geometries by changing only the module of the code that generates the coefficients needed for the equations at the boundary nodes. The immersed-boundary method implemented will be detailed in §3.3.

To discretize the convective, pressure, and viscous terms, we use a second-order, centered finite-difference scheme on a staggered grid (Ferziger & Perić, 1996). The integration in time is done using a fractional step, pressure correction method, in combination with a three substep Runge–Kutta, resulting in second-order accuracy in time (Le & Moin, 1991). The viscous terms are treated implicitly and the convective terms explicitly, so that the discrete form of (3.1)–(3.2) for the nth time step is

$$\begin{aligned}\left[1-\Delta t\frac{\beta_k}{\mathrm{Re}_z}\mathrm{L}\right]\boldsymbol{u}_k^n &= \boldsymbol{u}_{k-1}^n+\Delta t\left[\frac{\alpha_k}{\mathrm{Re}_z}\mathrm{L}\left(\boldsymbol{u}_{k-1}^n\right)-\gamma_k\mathrm{N}\left(\boldsymbol{u}_{k-1}^n\right)\right.\\ &\quad\left.-\zeta_k\mathrm{N}\left(\boldsymbol{u}_{k-2}^n\right)-\left(\alpha_k+\beta_k\right)\mathrm{G}\left(p^n\right)\right], \qquad k=1,2,3 \qquad (3.5)\\ \mathrm{L}\left(\phi^{n+1}\right) &= \frac{1}{\Delta t}\mathrm{D}\left(\boldsymbol{u}_3^n\right), \qquad (3.6)\\ p^{n+1} &= p^n+\phi^{n+1}, \qquad (3.7)\\ \boldsymbol{u}^{n+1} &= \boldsymbol{u}_3^n-\Delta t\mathrm{G}\phi^{n+1}, \qquad (3.8)\end{aligned}$$

where k is the Runge–Kutta substep, $\boldsymbol{u}_0^n=\boldsymbol{u}^n$, and D, G, L = DG, and N are the discretized divergence, gradient, Laplacian and nonlinear-convective operators. Note that continuity is only enforced at the last Runge–Kutta substep. The coefficients α_k, β_k, γ_k and ζ_k are those in Le & Moin (1991). Since $\partial v/\partial x=\partial w/\partial x=0$, the convective terms involving u in the equations for v and w vanish. The crossflow decouples from the streamwise flow, and it can be solved independently. The same does not hold for the streamwise equation, that requires the input from the crossflow. However, the equation for u is simpler, because it is a scalar that requires no continuity, nor a pressure correction substep.

To solve the discrete linear systems in equations (3.5) and (3.6), we take advantage of the periodicity of the problem in z, and perform fast Fourier transforms in that direction. The system then reduces to a set of tridiagonals that can be solved efficiently by LU decomposition. Given any variable ξ, for the z derivatives in the left-hand side of (3.5) and (3.6) we substitute the spectral operator

$$\mathcal{L}\left(\frac{\partial^2\xi}{\partial z^2}\right)=-k_z^2\mathcal{L}\left(\xi\right), \qquad (3.9)$$

where $\mathcal{L}$ denotes the Fourier transform and k_z the spectral wavenumber, by the approximation

$$\mathcal{L}\left(\frac{\partial^2\xi}{\partial z^2}\right)=2\,\frac{\cos\left(k_z\Delta z\right)-1}{\Delta z^2}\,\mathcal{L}\left(\xi\right). \qquad (3.10)$$

We thus sacrifice the spectral resolution of conventional Fourier methods, but preserve the consistency with the finite-difference discretization. For the temporal integration, we use

a variable time step, chosen so that the convective and viscous Courant–Friedrichs–Lewy numbers, CFL_C and CFL_V respectively, are

$$\mathrm{CFL}_C = \Delta t \left\| \frac{|v|}{\Delta y} + \frac{|w|}{\Delta z} \right\| \leq 0.5, \tag{3.11}$$

$$\mathrm{CFL}_V = \frac{\Delta t}{\mathrm{Re}_z \min\left(\Delta y^2, \Delta z^2\right)} \leq 2. \tag{3.12}$$

The Stokes regime

The above solution method needs to be modified slightly for the Stokes case, $\mathrm{Re}_z = 0$, for which results are discussed in the §4.1. The pressure is then scaled with $\rho\nu S_z$ instead of $\rho(sS_z)^2$, and equation (3.2) takes the form

$$\frac{\partial \boldsymbol{u}}{\partial t} = -\nabla p + \nabla^2 \boldsymbol{u}, \tag{3.13}$$

Having no convective terms, the streamwise flow and the crossflow are now fully decoupled and, since we are now only interested in the final stationary flow, we solve them separately. Since there are no explicit convective terms, we can use a simple implicit Euler algorithm for the velocity step. The fractional-step algorithm reduces then to

$$\begin{aligned}
[1 - \Delta t \mathrm{L}]\, \widehat{\boldsymbol{u}}^{n+1} &= \boldsymbol{u}^n - \Delta t \mathrm{G}\left(p^n\right), && (3.14)\\
\mathrm{L}\left(\phi^{n+1}\right) &= \frac{1}{\Delta t}\mathrm{D}\left(\widehat{\boldsymbol{u}}^{n+1}\right), && (3.15)\\
p^{n+1} &= p^n + \phi^{n+1}, && (3.16)\\
\boldsymbol{u}^{n+1} &= \widehat{\boldsymbol{u}}^{n+1} - \Delta t \mathrm{G}\phi^{n+1}. && (3.17)
\end{aligned}$$

Only the crossflow requires a pressure correction step, so for the streamwise flow the algorithm merely reduces to

$$[1 - \Delta t \mathrm{L}]\, u^{n+1} = u^n, \tag{3.18}$$

Note that the solution of the Stokes problem (3.13), which is normalized for unity shear at $y \to \infty$ in both the streamwise and transverse directions, only depends on the riblet geometry.

3.1.2 Flow driven by a uniform pressure gradient

We will see in chapter 7 that it is also useful to calculate the Stokes flow within a riblet groove driven by a uniform streamwise pressure gradient, $-p_\ell$, instead of the uniform shear of the above section. The momentum equations are still defined by (3.13), but $v = w = 0$,

so only the streamwise flow must be solved. The velocity u is normalized with $s^2 p_\ell/\rho\nu$, leading to

$$\frac{\partial \boldsymbol{u}}{\partial t} = 1 + \nabla^2 \boldsymbol{u}, \tag{3.19}$$

which can be solved using a slight modification of the algorithm (3.18), namely

$$[1 - \Delta t \mathrm{L}]\, u^{n+1} = u^n + \Delta t, \tag{3.20}$$

with no-slip conditions at the groove surface, again imposed using the immersed-boundary method detailed in §3.3, and $\partial u/\partial y = 0$ at the riblet-peak plane. The stationary solution required for the 'penetration length' of chapter 7 is obtained from the time evolution of (3.20), as the asymptotic final state.

3.2 Numerical method for the direct simulation of flows in ribbed channels

In this section we outline the method used to solve the incompressible Navier–Stokes equations in a parallelepiped that includes the walls of a ribbed channel, periodic in the two wall-parallel directions.

When the spacing between riblets is in the drag-reducing range, the accurate representation of the flow near the ribbed walls requires a finer grid than the one required for the body of the channel. To alleviate the computational cost, our grid is divided into three blocks, one near each wall in which the resolution is fine enough to represent the riblets, and a coarser central one in which the resolution is only enough to simulate the turbulence. The walls are modeled with the immersed-boundary technique detailed in §3.3.

The velocities and pressure are collocated and expanded in Fourier series along the two wall-parallel directions x and z. The differential operators are approximated spectrally along those directions, and the nonlinear terms are dealiased using the 2/3 rule. The spatial differential operators in y are discretized using second-order, centered finite-differences on a non-uniform grid. The grid spacing in y is coarsest at the center of the channel and finest near the walls, as shown in figure 3.1, remaining nearly constant within the riblet grooves. The number of x modes is set equal in the three blocks. In the central block of the grid, the resolution along z is just enough to capture the smallest turbulent scales, while the number of z modes in the blocks containing the walls is higher, to solve the flow around the riblets with sufficient accuracy. The required number of z-collocation

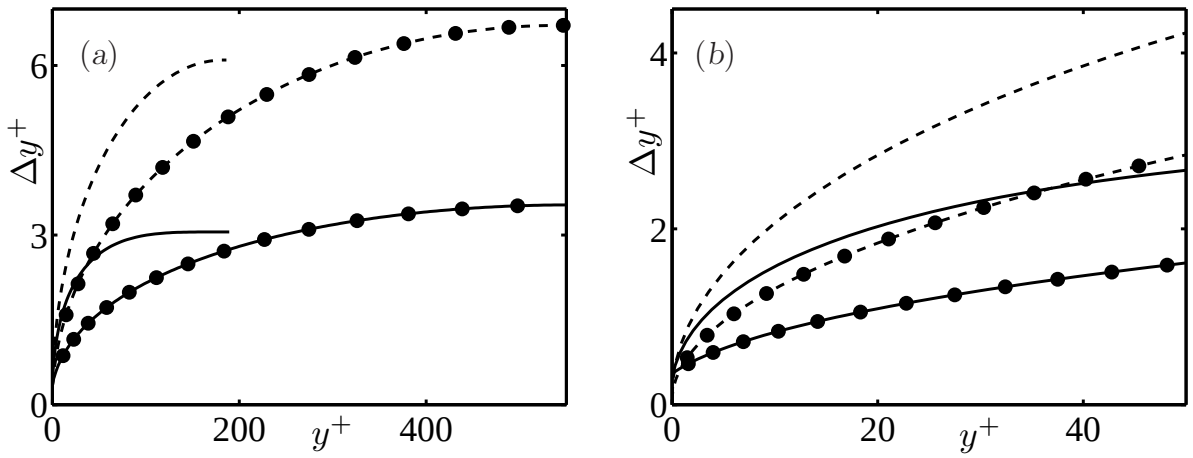

Figure 3.1: (*a*) DNS grid resolution in the wall normal direction. ——, present finite-difference grid for $\mathrm{Re}_\tau \approx 185$; – – – –, spectral grid from del Álamo & Jiménez (2003) for $\mathrm{Re}_\tau \approx 185$; —●—, present finite-difference grid for $\mathrm{Re}_\tau \approx 550$; – –●– –, spectral grid from del Álamo & Jiménez (2003) for $\mathrm{Re}_\tau \approx 550$. (*b*) Detail of the grid resolution in the near-wall region.

points per riblet depends on the particular geometry and, so long as the wall resolution remains higher than that required by turbulence, it can remain constant when varying s^+. For each geometry considered, the total number of nodes in the wall blocks is then proportional to the number of riblets in the simulation box.

The additional Fourier modes of the wall blocks require boundary conditions at the interface with the central block, where they disappear. We impose at those points that the three velocities and $\partial p/\partial y$ vanish, and require that the wall blocks extend far enough into the channel for those four quantities to have decayed to negligible levels at the interface. This condition is checked *a posteriori* and found to be satisfied beyond one or two riblet heights above the plane of the riblet tips, comparable to the y limit of our two-dimensional simulations, where the flow was required to be uniform above the riblet unit.

Incompressibility is enforced weakly (Nördstrom *et al.*, 2007). If we denote the velocity divergence by $D = \nabla \cdot \boldsymbol{u}$, the equations of motion are,

$$\frac{\partial \boldsymbol{u}}{\partial t} + \boldsymbol{u} \cdot \nabla \boldsymbol{u} = -\nabla p + \frac{1}{\mathrm{Re}} \nabla^2 \boldsymbol{u}, \tag{3.21}$$

$$\frac{\partial D}{\partial t} = -\lambda_D D + \frac{1}{\mathrm{Re}_D} \nabla^2 D, \tag{3.22}$$

where λ_D and Re_D are positive coefficients, so that D is driven continuously and exponentially towards zero, instead of being required to vanish strictly. This weak form of the incompressibility condition allows us to use a collocated grid, while eliminating the usual

'checkerboard' problem (Ferziger & Perić, 1996).

The temporal integrator is a fractional-step, pressure-correction, three-substep Runge–Kutta, which only corrects the pressure in the final step (Le & Moin, 1991),

$$\left[1-\Delta t\frac{\beta_k}{\mathrm{Re}}\mathrm{L}\right]\boldsymbol{u}_k^n = \boldsymbol{u}_{k-1}^n+\Delta t\left[\frac{\alpha_k}{\mathrm{Re}}\mathrm{L}\left(\boldsymbol{u}_{k-1}^n\right)-\gamma_k\mathrm{N}\left(\boldsymbol{u}_{k-1}^n\right)\right.$$
$$\left.-\zeta_k\mathrm{N}\left(\boldsymbol{u}_{k-2}^n\right)-(\alpha_k+\beta_k)\,\mathrm{G}\left(p^n\right)\right], \qquad k=1,2,3 \tag{3.23}$$

$$D^{n+1} = D^n+\Delta t\,\mathrm{F}\left(D^n+\frac{\Delta t}{2}\mathrm{F}\left(D^n\right)\right), \tag{3.24}$$

$$\mathrm{L}\left(\phi^{n+1}\right) = -\frac{1}{\Delta t}\left(D^{n+1}-\mathrm{D}\left(\boldsymbol{u}_3^n\right)\right), \tag{3.25}$$

$$p^{n+1} = p^n+\phi^{n+1}, \tag{3.26}$$

$$\boldsymbol{u}^{n+1} = \boldsymbol{u}_3^n-\Delta t\mathrm{G}\phi^{n+1}, \tag{3.27}$$

where k is the Runge–Kutta substep, $\boldsymbol{u}_0^n=\boldsymbol{u}^n$, N is the dealiased convective term operator, D, G, and L are the discretized divergence, gradient and Laplacian operators, and $\mathrm{F}(D)=-\lambda_D D+\mathrm{L}(D)/\mathrm{Re}_D$. Because of the weak treatment of incompressibility, $\mathrm{L}=\mathrm{DG}$ is not required to hold strictly, so the three operators can use second-order finite-differences in y even with a collocated grid. The coefficients α_k, β_k, γ_k and ζ_k are again those in Le & Moin (1991). If strict incompressibility is enforced, the above method is second order in time for the velocity, with the second-order errors mostly associated with the viscous terms, and the convective terms producing higher-order errors, as in most incompressible fractional-step Runge–Kutta schemes (Simens *et al.*, 2009). The advancing scheme for the divergence (3.24) was chosen to preserve that second order accuracy.

The variable time step is adjusted to maintain fixed $\mathrm{CFL}_C=0.5$ and $\mathrm{CFL}_V=2.5$, so that

$$\Delta t=\min\left\{\mathrm{CFL}_C\left[\frac{\Delta x}{\pi|u|},\frac{\Delta z}{\pi|w|},\frac{\Delta y}{|v|}\right],\mathrm{Re}\,\mathrm{CFL}_V\left[\frac{\Delta x^2}{\pi^2},\frac{\Delta z_c^2}{\pi^2},\frac{\Delta z_r^2}{\pi^2},\frac{\Delta y_{\min}^2}{4}\right]\right\}, \tag{3.28}$$

where the subscripts 'c' and 'r' refer to the central and riblets blocks.

The parameters λ_D and Re_D are chosen at each time step so that (3.24) is stable for the Δt given by (3.28). From the numerical analysis of (3.24), it follows that the condition for stability is $|\Delta t\,\mathrm{F}|\leq 2$, or

$$\lambda_D \leq \frac{2}{\Delta t}, \tag{3.29}$$

$$\mathrm{Re}_D \geq \frac{\Delta t}{2-\Delta t\lambda_D}\max\left[\frac{\pi^2}{\Delta x^2},\frac{\pi^2}{\Delta z_c^2},\frac{\pi^2}{\Delta z_r^2},\frac{4}{\Delta y_{\min}^2}\right]. \tag{3.30}$$

For our simulations, we have chosen

$$\lambda_D = \frac{q_D}{\Delta t}, \tag{3.31}$$

$$\mathrm{Re}_D = \frac{4\Delta t}{3-2q_D}\left[\frac{\pi^2}{\Delta x^2}+\frac{\pi^2}{\Delta z_r^2}+\frac{4}{\Delta y_{\min}^2}\right], \tag{3.32}$$

with $q_D = 0.8$. The resulting divergence in the flow is never higher than $D^+ \approx 2\cdot 10^{-4}$, which should be compared with the magnitude of other velocity gradients, for example the magnitude of the vorticity, $|\omega^+| \approx 0.05 - 0.2$.

The channel half-height is $\delta = 1$ in all cases, including in the smooth reference one, and is defined as the distance from the center of the channel to the riblet tips, while the domain half-height is slightly larger, extending to the groove floors. The time-dependent mean streamwise pressure gradient P_x is adjusted to ensure a constant flow rate Q in $y \in (0, 2\delta)$. Thus, the periodic channel resembles a segment of an infinitely long one in which, because of continuity, the flow rate is forced to be constant, while the pressure gradient, which is constant in the infinite channel, fluctuates for the segment around its mean value. This technique yields the same results as keeping a constant pressure gradient and letting the flow rate fluctuate (Orlandi, 2000). The constant Q is achieved at each substep by a correction ΔU_k^n to the instantaneous plane-averaged streamwise velocity profile U_k^n,

$$\left[1-\Delta t\frac{\beta_k}{Re}\frac{\partial^2}{\partial y^2}\right]\hat{U}_k^n = -\Delta t\left(\alpha_k+\beta_k\right), \tag{3.33}$$

$$\Delta P_x = \frac{Q-Q_k^n}{\hat{Q}_k^n}, \tag{3.34}$$

$$\Delta U_k^n = \Delta P_x \hat{U}_k^n, \tag{3.35}$$

where $\hat{Q}_k^n$ is the flow rate associated with the auxiliary $\hat{U}_k^n$, and Q_k^n is the flow rate of the uncorrected U_k^n. For simplicity, $\hat{U}_k^n$ is only defined for $y \in (0, 2\delta)$, and its boundary conditions are $\hat{U}_k^n = 0$ at the riblet tip planes, so there is no correction within the grooves owing to the constant Q constrain. This entails a very small error, because the corrections on P_x and U_k^n are several orders of magnitude smaller than their uncorrected values. Except for that small error, the procedure is equivalent to imposing on the discretized Navier–Stokes problem (3.23)–(3.27) the time-dependent pressure gradient required to obtain a constant flow rate, which is the procedure used in most channel DNSs, both smooth (Moser *et al.*, 1999; del Álamo & Jiménez, 2003; Hoyas & Jiménez, 2006) and rough (Choi *et al.*, 1993; Chu & Karniadakis, 1993; Orlandi *et al.*, 2006; El-Samni *et al.*, 2007). The procedure is explicitly formulated in Chu & Karniadakis (1993).

Case	$1/\nu$	N_R	L_x	L_z	N_x	N_{z_c}	N_{z_r}	N_y	$T\,u_\tau/\delta$
20CH	3200	8	1.05π	0.30π	72	72	576	153	335
0S	3250	0	2π	0.67π	192	192	192	153	175
5S	3250	48	2π	0.67π	192	192	1152	153	171
7S	3250	32	2π	0.67π	192	192	768	153	170
10S	3250	24	2π	0.67π	192	192	576	153	169
13S	3250	18	2π	0.67π	192	192	432	153	169
15S	3250	16	2π	0.67π	192	192	384	153	170
17S	3250	15	2π	0.73π	192	192	360	153	173
20S	3250	12	2π	0.67π	192	192	288	153	177
10FX	3250	24	2π	0.67π	384	192	576	153	11
10FZ	3250	24	2π	0.67π	192	192	1152	153	11
10DX	3250	24	4π	0.67π	384	192	576	153	17
10DZ	3250	48	2π	1.33π	192	384	1152	153	26
17FX	3250	15	2π	0.73π	384	192	360	153	11
17FZ	3250	15	2π	0.73π	192	192	720	153	11
17DX	3250	15	4π	0.73π	384	192	360	153	15
17DZ	3250	30	2π	1.46π	192	384	720	153	53
0L	11180	0	3π	1.50π	576	576	576	453	90
07L	11180	216	3π	1.48π	576	576	5184	453	15
13L	11180	128	3π	1.52π	576	576	3072	453	15
20L	11180	72	3π	1.34π	576	576	1728	453	15

Table 3.1: Parameters of the DNSs conducted. ν is the kinematic viscosity, N_R is the number of riblets in the simulation box, L_x and L_z are the channel length and width, N_x is the number of collocation points in the streamwise direction, N_{z_c} and N_{z_r} are those in the spanwise direction for the central and wall blocks respectively, and N_y those in the wall normal direction for $-\delta \leq y \leq \delta$. T is the approximate total time of the simulation, given in terms of the eddy-turnover time, δ/u_τ.

The parameters of our simulations are given in table 3.1. Simulation 20CH reproduces one of the cases studied in Choi *et al.* (1993), and served as a validation test for the code. The box includes riblets at the lower wall only, and thus has a single fine-resolution block, with the upper wall included in the coarser block. Results are presented in §3.4.4.

Simulations 0S to 20S were conducted with $\mathrm{Re}_\tau \approx 185$ for a rectangular-blade geometry with riblet height $h = 0.5s$ and tip width $t_r = 0.25s$, with the number of riblets in the box

systematically varied to span the full drag-reducing range. Case 0S is actually a smooth channel, and was also used for the validation of the code. To our knowledge, this is the first time that such a systematic parameter sweep has been undertaken for numerical riblets, except perhaps that by El-Samni *et al.* (2007), who included five different riblet sizes. Notice that L_z is increased slightly in case 17S, to obtain the desired ℓ_g^+ while keeping the fixed geometric resolution of the riblets, 24 collocation points per riblet in z. For this set of simulations, the number of x modes was set so that $\Delta x^+ \approx 6$, in terms of collocation points, in the three blocks, and the spanwise resolution in the central block was set to $\Delta z^+ \approx 2$. The spanwise grid is thus between 1.5 and 6 times finer in the wall blocks than in the central one, depending on the case. In the wall-normal direction, $\Delta y^+_{\text{min}} \approx 0.3$ at the riblet peaks, and $\Delta y^+_{\text{max}} \approx 3$ at the center of the channel. The simulations in this set were run for more than 150 eddy turn-over times, δ/u_τ, of which the first few were discarded to avoid the effects of the initial transients on the statistics. They had to be run for such long times to reduce the effect of the wall-friction oscillations, which, for the relatively small simulation boxes, are of the order of 10%. This set of simulations will be throughly analyzed in chapter 5.

In addition, cases 10S and 17S were repeated while independently doubling N_x, N_{z_r}, and the length and width of the channel, to check whether the simulations could be considered converged with respect to the grid and box sizes. These simulations, 10DX to 17FZ, were not required to run for such long times, in part because of their increased computational cost, but mainly because the precision in the friction statistics mentioned above was here unnecessary. The results are presented in §3.4.5.

To analyze the effect of the Reynolds number, a final set of simulations was conducted with $\text{Re}_\tau \approx 550$. The computational cost of these simulations is several orders of magnitude higher than the previous ones, so we reduced the number of cases from eight to four: a smooth reference case, 0L; one in the viscous regime, 7L, one near the optimum performance, 13L, and one well past the viscous breakdown, 20L. Though still in the DNS range, the resolution of these simulation is somewhat higher, $\Delta x^+ \approx 9$, $\Delta y^+_{\text{min}} \approx 0.3$ and $\Delta y^+_{\text{max}} \approx 3$, and $\Delta z^+ \approx 4$ in the central block. Also, the convective CFL number was raised to $\text{CFL}_C = 0.7$. The boxes are, in wall units, much larger than those with $\text{Re}_\tau \approx 185$, so the friction fluctuations were much smaller, and the number of eddy turnovers required to achieve the desired convergence of the drag-reduction results was greatly reduced. The simulation time for case 0L was much longer because the initial field was taken from case 0S, and the large scales of the flow required very long times to reach equilibrium with the new conditions. The results of these simulations can be found

in chapter 6.

3.3 Implementation of immersed boundaries

To model the no-slip condition at the riblet walls, we use the direct-forcing immersed-boundary technique of Mohd-Yusof (1997). With that method, the discrete equation satisfied by the points where the boundary condition is enforced would be

$$\frac{\boldsymbol{u}^{n+1}-\boldsymbol{u}^{n}}{\Delta t}=\frac{\boldsymbol{V}-\boldsymbol{u}^{n}}{\Delta t}, \tag{3.36}$$

where $\boldsymbol{V}$ is the desired velocity at the forcing points. Numerically, the above immersed-boundary condition is approximated by

$$\left[1-\Delta t\frac{\beta_k}{\mathrm{Re}}\mathrm{L}\right]\boldsymbol{u}_k^n=\left(\boldsymbol{V}_{k-1}^n-\boldsymbol{u}_{k-1}^n\right)+\left[1-\Delta t\frac{\beta_k}{\mathrm{Re}}\mathrm{L}\right]\boldsymbol{u}_{k-1}^n, \tag{3.37}$$

which, in practice, is a modification at the forcing points of (3.23) or (3.5), or of (3.14) and (3.20) if the β_k/Re factors are dropped.

If the forcing point is not exactly at the virtual, immersed boundary, the term $\boldsymbol{V}_{k-1}^n$ can be explicitly calculated from the velocity $\boldsymbol{u}_{k-1}^n$ at the neighboring grid points, using either linear interpolation (Fadlun *et al.*, 2000) or extrapolation (Iaccarino & Verzicco, 2003). We have favored an extrapolation scheme whenever possible, because it does not apply momentum forcing within the flow field. However, in the cases in which the boundary is very close to one of the fluid nodes used to calculate $\boldsymbol{V}_{k-1}^n$, extrapolation may cause numerical instability, because it leads to large negative weighting coefficients (Tseng & Ferziger, 2003). In those cases, we have substituted the extrapolation by an interpolation involving nearby nodes. For example, in figure 3.2(a), triangle (I) substitutes an equal triangle right below it, which would have lead to a large weighting coefficient. As a criterion to discard nodes we set a threshold for the weighting coefficients, typically -4 for the two-dimensional simulations and -0.4 for the DNSs. However, for the DNSs this interpolation/extrapolation process was only necessary for the triangular riblets of case 20CH, since the surface of our rectangular riblets is formed by grid points, so $\boldsymbol{V}$ is always zero. Equation (3.37) was additionally used in our DNSs to force the velocities to vanish at all the points within the solid part of the riblets, and there is a notional flat boundary at the level of the groove floors, where the velocities and $\partial p/\partial y$ are also required to vanish.

Immersed boundaries are an approximate technique, and as such the surface velocity is never exactly zero. The errors come from the implicit treatment of the viscous term

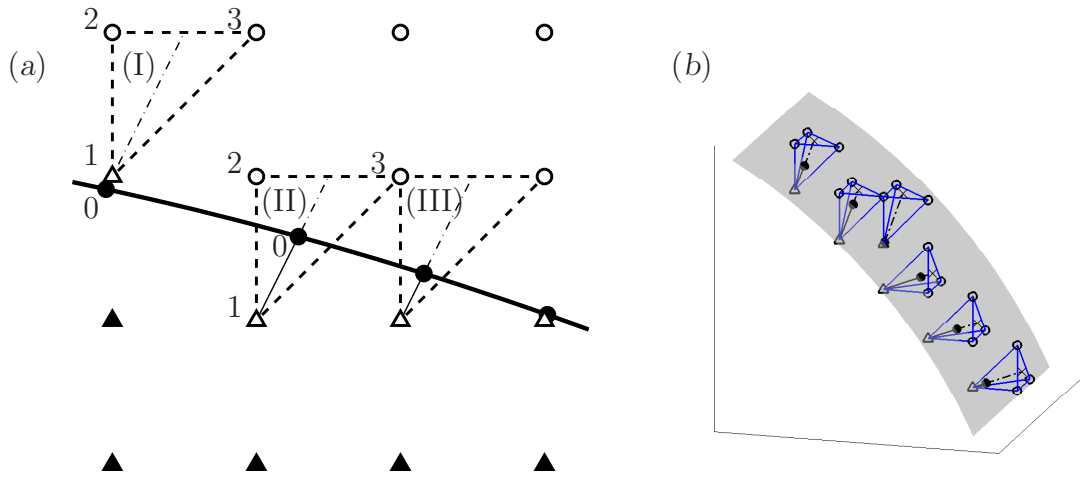

Figure 3.2: (*a*) Two-dimensional immersed-boundary implementation. ○, fluid internal nodes, where Navier–Stokes equations are satisfied, ▲, nodes inside the solid body; ●, points at the boundary, in which the velocity is known (point 0); △, nodes where the boundary conditions are imposed (point 1). In triangle (I), an interpolation scheme is used, so that the velocity to be imposed at node 1 is interpolated from the velocities at nodes 2 and 3 and the velocity at point 0. In triangles (II) and (III), an analogous scheme is used, but in those cases the velocity at 1 is calculated from those at 2, 3 and 0 by extrapolation. Note that points of class 0 do not belong to the grid. (*b*) Sketch of a three-dimensional immersed-boundary implementation.

and from the pressure-correction step (see Fadlun *et al.* (2000), for more details). The transpiration is not related to the Reynolds number of the flow directly, but to the viscous CFL of the time integrator. In our case, the resulting velocities at the riblet surface are at worst of order $0.1u_\tau$ for u, and $0.01u_\tau$ for v and w, which is in both cases roughly one order of magnitude smaller than the corresponding values in the first grid point away from the surface. Figure 3.3 shows typical values of the velocities near the wall. The small penetration of flow is mostly in the blade corners, and is equivalent to a small rounding of the riblet peaks. That only affects the viscous slope of the drag curve (m_ℓ), and has a negligible impact on the dynamics of the breakdown, as will be discussed in §4.1.2. In chapters 5 and 6, the impact on m_ℓ will be taken into consideration by obtaining the protrusion heights from Stokes simulations with equivalent resolution.

Note that the interpolation/extrapolation triangle scheme portrayed in figure 3.2(*a*) is intrinsically two-dimensional and, for flows over three-dimensional surfaces, a scheme based on tetrahedra, such as the one sketched in figure 3.2(*b*), would be more suitable. However, the two-dimensional character of the riblet surface makes such scheme unnecessary, and even undesirable. In our DNSs, we apply equation (3.37) not in the fully-physical

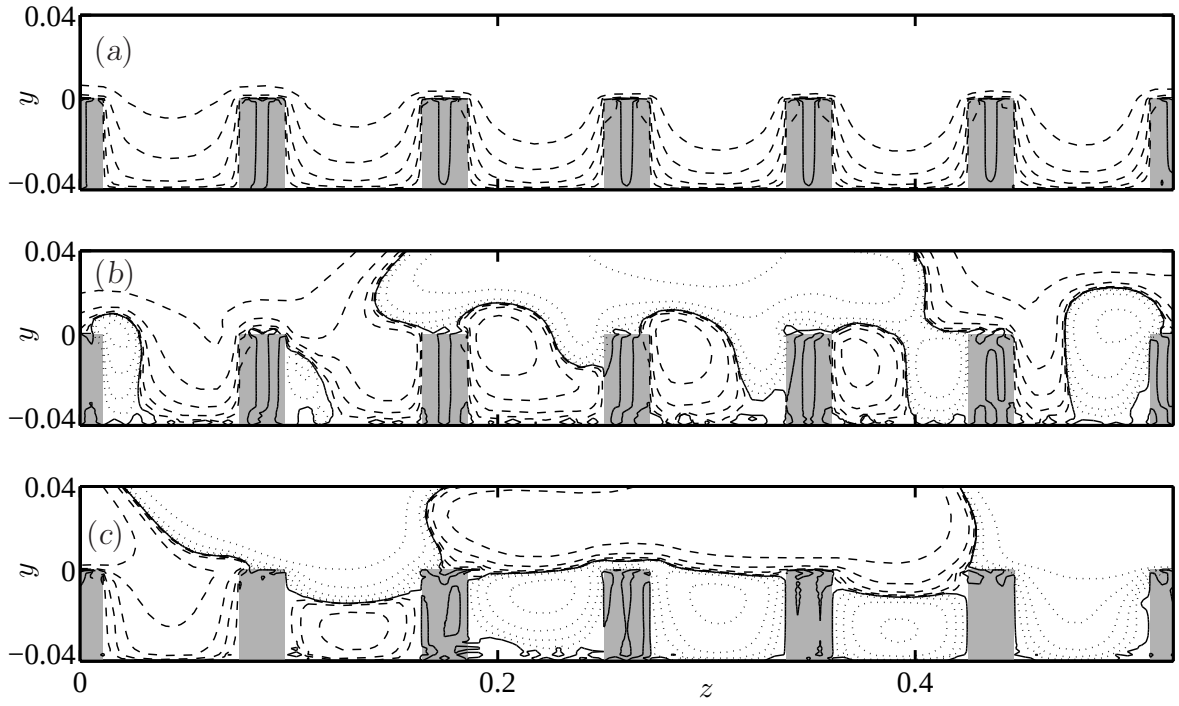

Figure 3.3: Permeability error for (*a*) u, (*b*) v and (*c*) w at the immersed boundaries, for a random instantaneous cross-section of simulation 10S. The dotted contours are negative, and the dashed ones positive, with zero solid. The absolute values of the non-zero contours are $[0.01(\times\sqrt{10})1]$ for u, and $[0.001(\times\sqrt{10})0.1]$ for v and w, in wall units.

space, but separately for each streamwise Fourier mode. Because of the linearity of the interpolation/extrapolation triangular scheme, and of the streamwise Fourier transform, this mode-by-mode implementation has spectral resolution in x, higher than any three-dimensional scheme, and is equivalent to a plane-by-plane triangular implementation.

For the Stokes case in §3.1.1, we have also applied an accelerated forcing version of (3.37),

$$[1 - \Delta t \mathrm{L}]\, \boldsymbol{u}^{n+1} = K\,(\boldsymbol{V}^n - \boldsymbol{u}^n) + [1 - \Delta t \mathrm{L}]\, \boldsymbol{u}^n, \tag{3.38}$$

where K is a coefficient that is set by trial and error in the range 1–100 to optimize the speed of convergence.

3.4 Code validation

3.4.1 Transition of the wake behind a cylinder

To validate the two-dimensional code described in §3.1.1, and in particular the immersed-boundary method of §3.3, we simulate the flow around a circular cylinder. The transition to an unsteady wake behind a cylinder is a typical –and very stringent– test often used for the validation of immersed-boundary methods, because the instability is very sensitive to the geometry of the obstacle (Linnick & Fasel, 2005). In our tests, the flow transitioned at Re ≈ 41, defined with the cylinder diameter, which is in good agreement with the experimental range Re $= 40 - 49$ (Roshko, 1953; Williamson, 1989). Hitting that bracket, as we do, requires a correct representation of the cylinder surface, which is after all, the main purpose of the immersed-boundary method.

The simulations were conducted in domains of size $50R \times 50R$, with R being the cylinder radius, as those portrayed in figure 3.4, with 512×512 points. Note that the implied total number of points where immersed-boundary forces are imposed to represent the presence of the cylinder is only of order ≈ 100. Periodic boundary conditions were imposed in the transverse direction, with $u = 1$ and $v = \partial p/\partial x = 0$ at the inflow and $\partial u/\partial x = \partial v/\partial x = \partial p/\partial x = 0$ at the outflow. Several Reynolds numbers in the range 10–100 were simulated. Some illustrative results are portrayed in figure 3.4, clearly showing the transition for Re ≈ 41, and figure 3.5, that shows the adequate resolution of the virtual cylinder surface. The weak flow inside the cylinder, which is induced by the extrapolation schemes of the immersed boundaries into points inside the cylinder, as sketched in figure 3.2(a), has no physical meaning.

3.4.2 Taylor–Green Vortex

To validate the time integrator described in §3.2, and in particular the weak enforcement of continuity of (3.22), we simulate Taylor–Green vortices. This flow is widely used to validate Navier–Stokes discretizations, because of its delicate balance between convective and pressure terms on one hand, and viscous and temporal terms on the other, and also because the existence of an analytical solution allows a precise quantification of errors. The analytical solution is

$$u = U_0\, e^{-2\nu t} \sin x \cos y, \tag{3.39}$$

$$v = -U_0\, e^{-2\nu t} \cos x \sin y, \tag{3.40}$$

$$p = U_0^2\, e^{-4\nu t} \cos 2x \sin 2y. \tag{3.41}$$

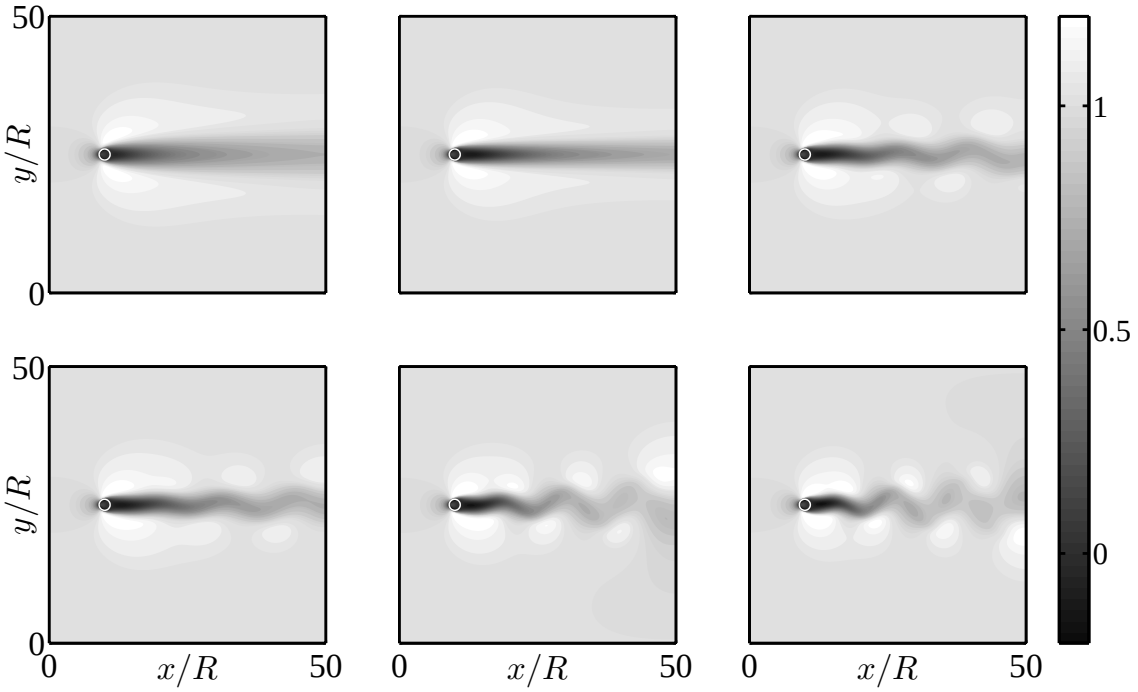

Figure 3.4: Instantaneous streamwise velocity contours of the flow around a circular cylinder at increasing Reynolds numbers, obtained with the code described in §3.1.1. From left to right and top to bottom, Re = 20, 40, 41, 42, 60, and 80.

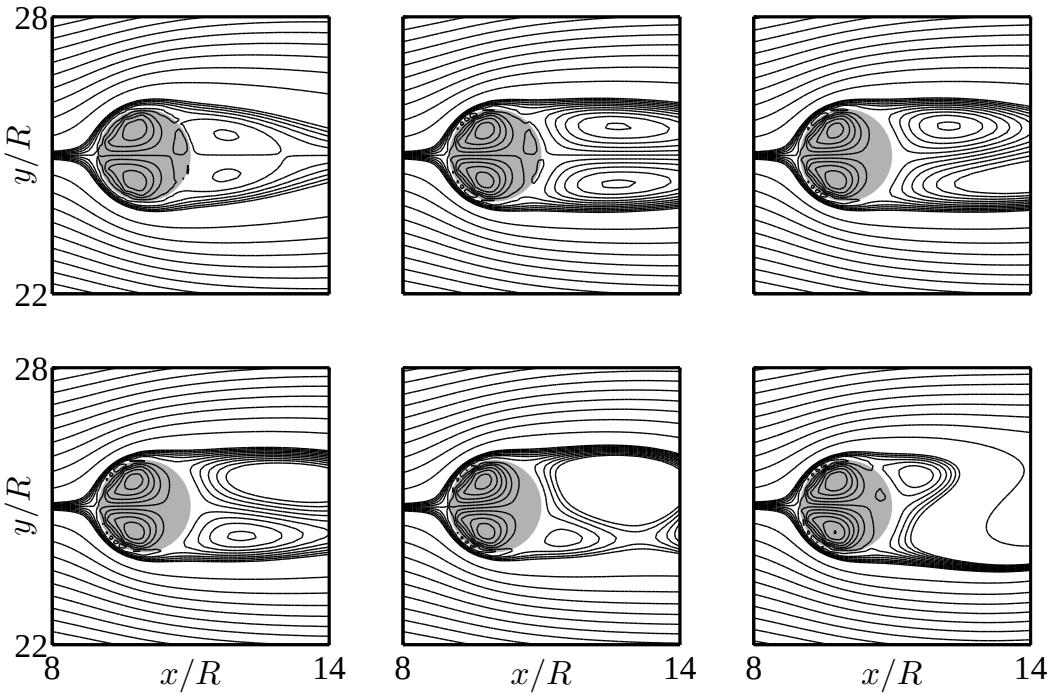

Figure 3.5: Instantaneous streamlines of the flow around a circular cylinder, in its immediate vicinity, for increasing Reynolds numbers, obtained with the code described in §3.1.1. From left to right and top to bottom, Re = 20, 40, 41, 42, 60, and 80. The streamfunction contours are in all the panels $[-0.05(0.01)0.05] \times U_\infty R$ and $[-2.5(0.25)2.5] \times U_\infty R$.

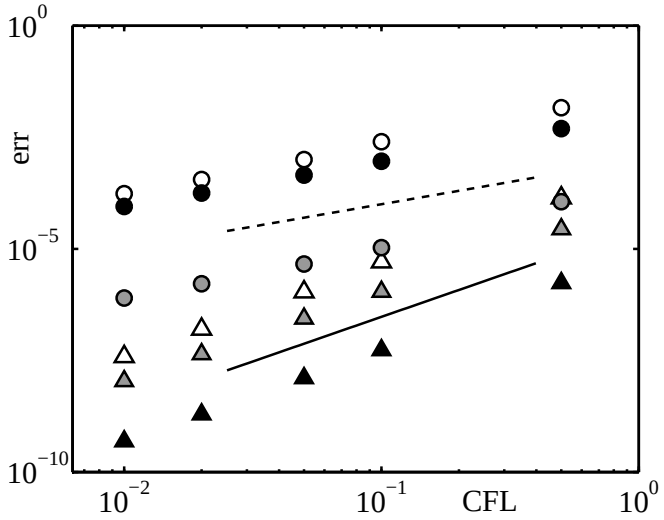

Figure 3.6: Influence of the CFL number on the global error for different Runge–Kutta algorithms. Triangles are used for the error in the velocities, and circles for the error in the pressure. Solid symbols correspond to the algorithm proposed in Simens *et al.* (2009), and open ones to the one presented in §3.2, both for $\mathrm{Re} = 10$ and with the global error measured at $t = 5\,L_x/U_0$. Grey symbols correspond to the latter algorithm, for $\mathrm{Re} = 1000$ and with the global error measured at $t = 100\,L_x/U_0$. ——, line with slope 2, indicating $\mathrm{err} \propto \Delta t^2$. - - - -, line with unity slope.

We solve the flow in a periodic domain of size $L_x \times L_y = 2\pi \times 2\pi$. The flow variables are expanded in Fourier series along both x and y, with the differential operators approximated spectrally, and the nonlinear terms dealiased using the 2/3 rule. We solve for 64 modes in each direction although, given the spectral resolution in space, a handful of modes would be enough to reproduce the solution (3.39)–(3.41). However, the resulting crystal of vortices is unstable, and the two vortex pairs in the periodic domain eventually merge into a single one, in a sudden transition. This can be circumvented by solving in a domain of half size $2\pi \times \pi$, imposing the corresponding symmetries, but since we are only interested in measuring the time resolution of different discretizations, it is sufficient to compare the errors for a given time before the transition occurs. Some of those errors are portrayed for increasing CFL number in figure 3.6, for two different Reynolds numbers, defined with the maximum initial velocity U_0 and the length $L_x/2\pi$. The figure shows that the method is indeed second-order accurate in time.

3.4.3 DNS of smooth channels

Another test for the method described in §3.2 is the comparison of the results for smooth channels with those in the literature. This serves as a test for the full method,

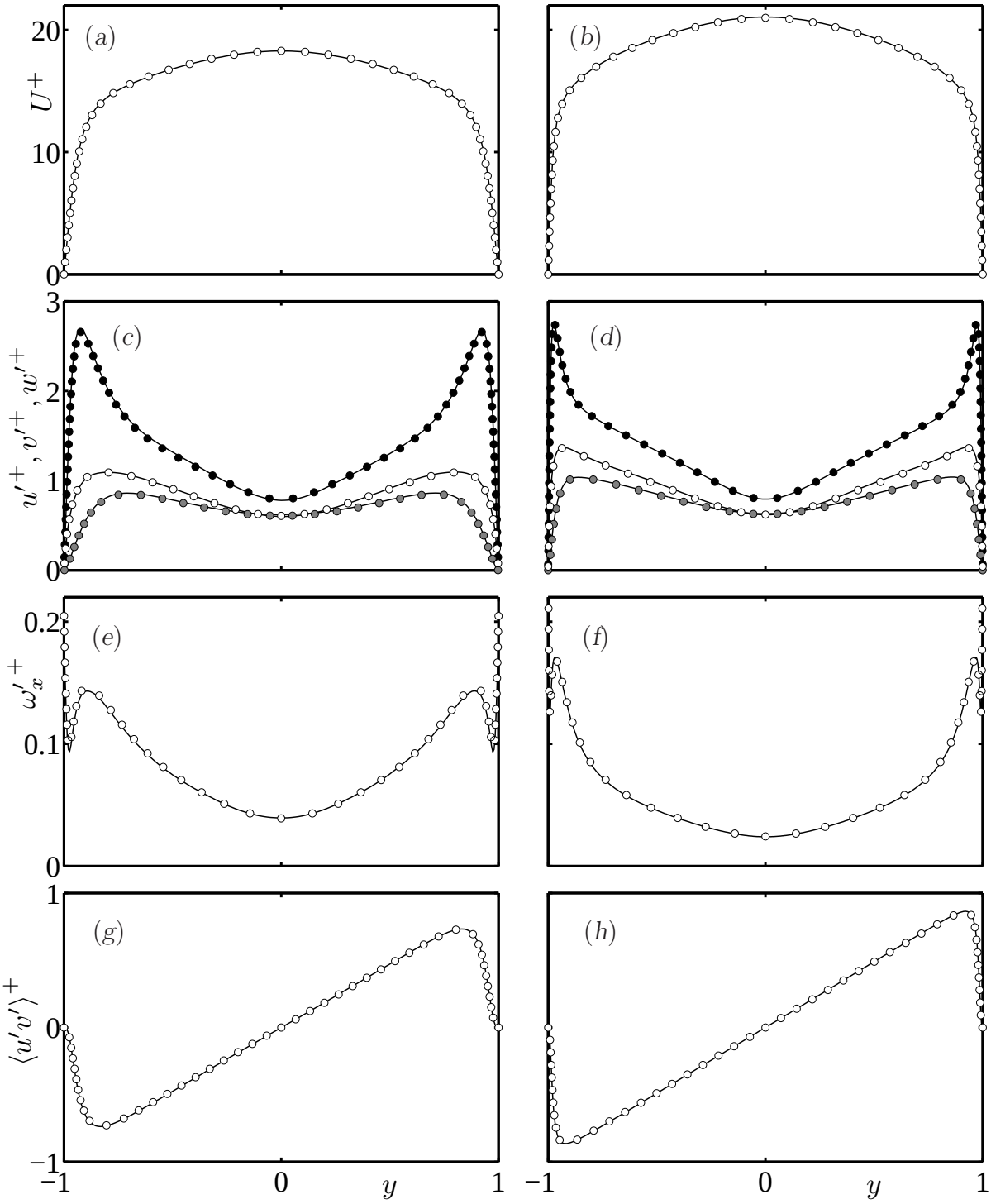

Figure 3.7: Comparison of results for smooth channels. (*a*), (*c*), (*e*) and (*g*), at $\mathrm{Re}_\tau \approx 185$, and (*b*), (*d*), (*f*) and (*h*), at $\mathrm{Re}_\tau \approx 550$. Solid lines represent results obtained with the code presented in §3.2, and symbols results from del Álamo & Jiménez (2003). (*a*) and (*b*), mean velocity profile. (*c*) and (*d*), velocity fluctuations; ●, u'^+; ●, v'^+; ○, w'^+. (*e*) and (*f*), streamwise vorticity fluctuations. (*g*) and (*h*), Reynolds stress.

including the complete, three-dimensional spatial discretization but, in the absence of an analytical exact solution, we can only compare the statistical properties of the flow.

The mean u profile, Reynolds stress, and fluctuations of the three velocities and of the streamwise vorticity are portrayed in figure 3.7. Cases 0S, $\mathrm{Re}_\tau \approx 185$, and 0L, $\mathrm{Re}_\tau \approx 550$, are compared with results from del Álamo & Jiménez (2003), showing a nearly exact agreement.

3.4.4 DNS of a channel with triangular riblets

Many of the reference riblet DNSs date back to the 1990's, and have either grids that we would now consider too coarse, simulation boxes that we would consider too small, or running times too short to consider their statistics fully converged. Of course, those were at the time pioneering simulations, and their resolution was limited by the capacity of computers at that time. It is actually surprising that present-day DNSs of riblets and other roughness are still run at $\mathrm{Re}_\tau \approx 180$ (Orlandi *et al.*, 2006; El-Samni *et al.*, 2007; Kramer *et al.*, 2010), which is turbulent only by a narrow margin. Nevertheless, the low Reynolds number has probably a small impact on the results, since the effect of riblets presumably extends only to the buffer layer.

We have validated our code by running one of the channels with triangular riblets in Choi *et al.* (1993), with 60° peak sharpness and $s^+ = 20$. This simulation had some of the caveats just described. For example, its streamwise resolution, $\Delta x^+ = 35$ in a second-order code, is between 4 and 6 times what we would dare to do. On the other hand, to achieve the same resolution as Choi *et al.*in the cross-plane near the riblet peaks, our homogeneous grid requires 72 collocation points in z per riblet, which is elsewhere much more than necessary. The simulation box was also very small, almost minimal (Jiménez & Moin, 1991), and had riblets only in the lower wall, defining the drag reduction as the relative difference between the friction at both walls. For a closer comparison, we have used the same domain and method to measure DR in this case.

The results are compared in Figure 3.8. The value $DR = 6\%$ reported by Choi *et al.*is portrayed, together with the value $DR = 4\%$ that they used as reference, which was obtained from experiments by Walsh (1982). We have obtained a mean $DR = 4.32\%$ from our simulation, extending for $t \approx 6000\,\delta/U_c$, much longer than the time span $t \approx 330\,\delta/U_c$ of Choi *et al.*. We also show DR results corresponding to partial averages over time intervals as long as that of Choi *et al.*, with the intervals overlapping and centered at the points portrayed. We conclude that, in their small box, the simulation of Choi *et al.*could have resulted in any value within the range we portray and that, as Choi himself declared

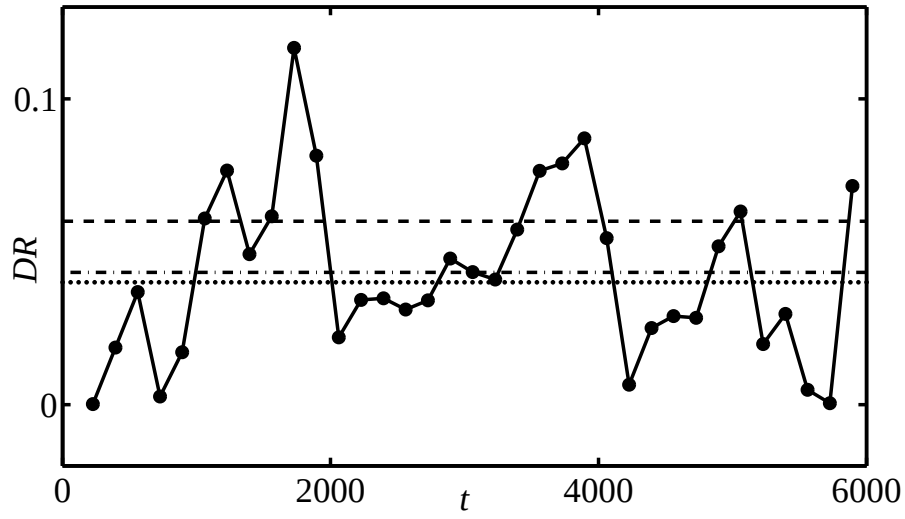

Figure 3.8: Drag reduction in a channel with triangular riblets in the lower wall, with 60° peak sharpness and $s^+ = 20$. – – – –, $DR = 6\%$ result from Choi *et al.* (1993); ·····, $DR = 4\%$ experimental result from Walsh (1982); – · – , result from the present DNS case 20CH, averaged from the full available simulation time; —●—, results from partial averages for intervals of length $t = 330\,\delta/U_c$, comparable to the full simulation time of Choi *et al.* (1993), centered at the symbols.

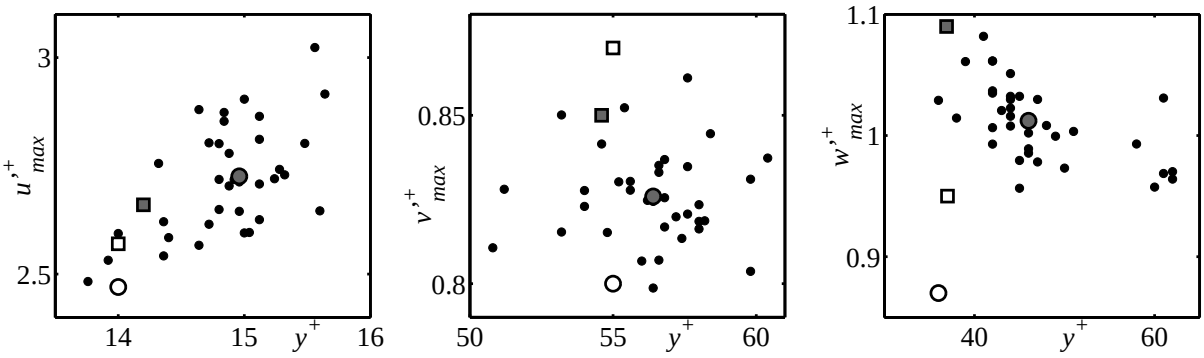

Figure 3.9: Maximum value and corresponding y coordinate of the velocity fluctuations. ●, result from the present DNS case 20CH, averaging for the full available simulation time; ○, corresponding value from Choi *et al.* (1993); ●, results from case 20CH averaged for partial intervals of length $t = 330\,\delta/U_c$, comparable to the full simulation time of Choi *et al.* (1993); ■, smooth channel from del Álamo & Jiménez (2003); □, smooth channel from Choi *et al.* (1992) with the same resolution as their riblets.

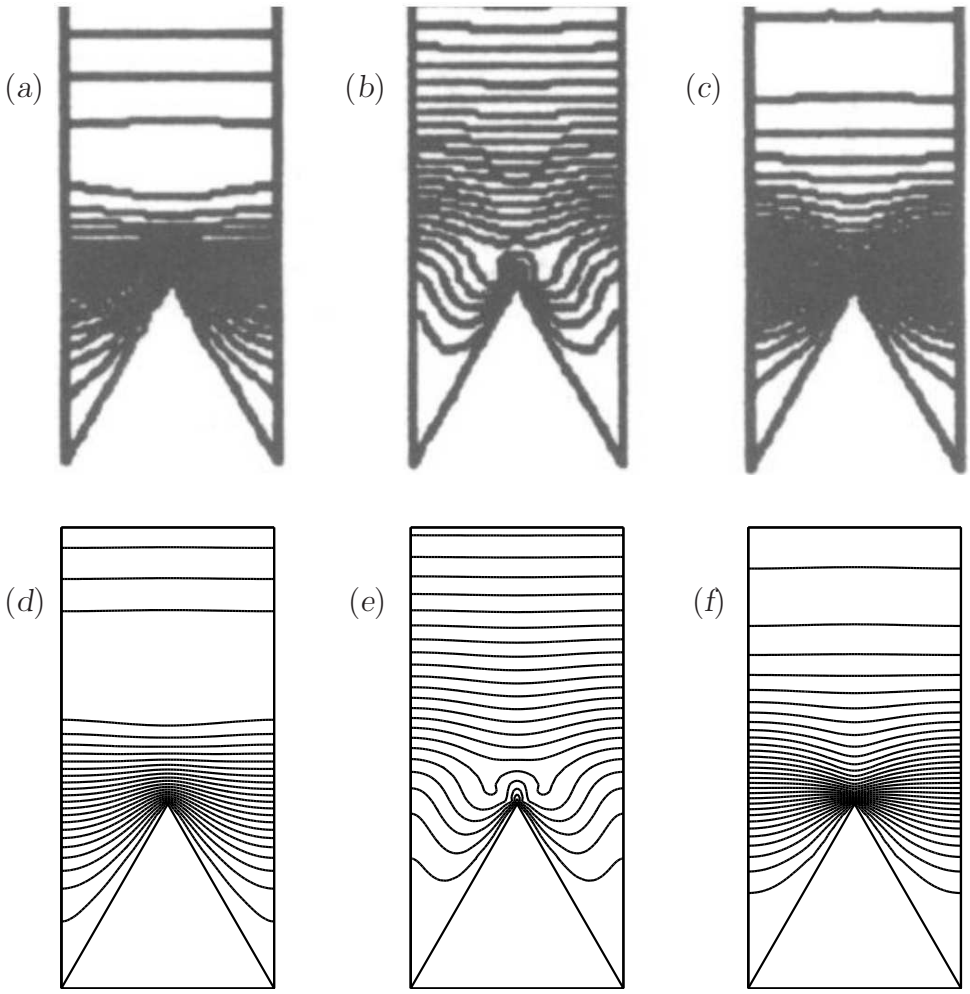

Figure 3.10: Mean fluctuation velocities conditioned to the position over the riblet. (a)-(*d*), u'; (*b*)-(*e*), v'; (*c*)-(*f*), w'. The first three panels have been scanned from figure 12 in Choi *et al.* (1993), while the other three correspond to our simulation 20CH. The contour increments are the same in both cases, $0.0064\,U_\delta$ for u', and $0.0016\,U_\delta$ for v' and w'.

in his thesis (Choi *et al.*, 1992), his simulation would have required a longer run time, and was only marginally converged.

The panels in figure 3.9 show comparisons of the maximum fluctuation velocities. Both the maximum values for u'^+, v'^+ and w'^+, and their corresponding y^+ coordinates are portrayed. In general, our values are higher than those of Choi *et al.*, but within the scatter of the short-time averages. The largest error is in w'^+_{max}, for which the values of Choi *et al.*are too low. That is also true also for their smooth case, whose results are lower than our spectral reference results, which otherwise agree well with standard simulations (Kim *et al.*, 1987; del Álamo & Jiménez, 2003). That is probably due to the

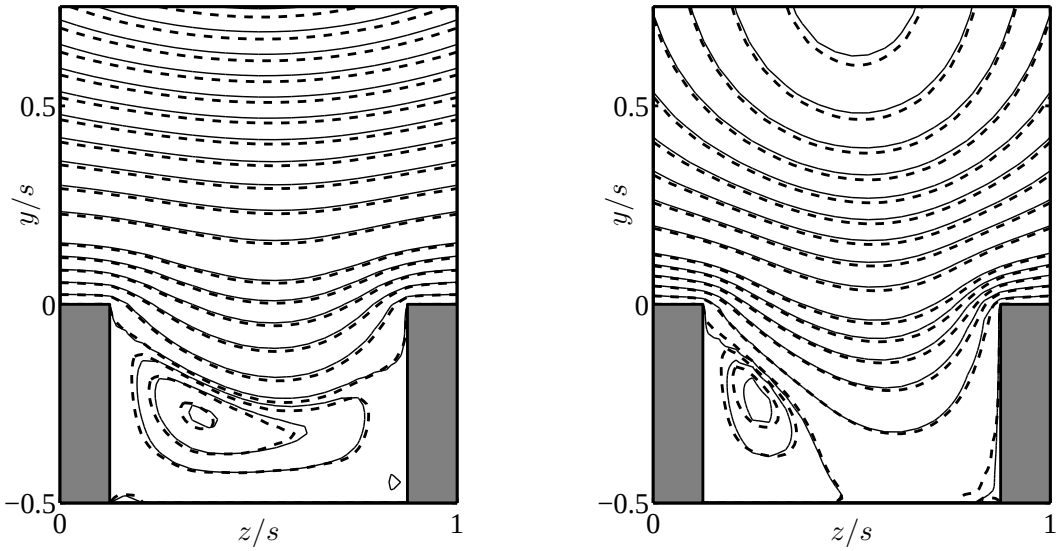

Figure 3.11: Streamfunction of the conditionally averaged cross-flow above and within the riblet grooves, conditioned to a mean rightwards flow in the plane immediately above the riblet tips. (*a*) simulations 10S and 10FZ; (*b*) 17S and 17FZ. ——, original resolution, cases 10S and 17S; - - - -, doubled spanwise resolution, 10FZ and 17FZ. The contours are the same for all cases, and are detailed in figure 5.2(*a*).

very low resolution of Choi *et al.*in the streamwise direction, which we have already mentioned (see Choi *et al.* (1992), appendix E, for details on the effect of the resolution of his simulations). The other notable feature, the scatter of the wall-normal height for w'^{+}_{max}, $y^+ = 40 - 60$, is due to the flatness of the w'^{+} curve, which is nearly constant between $y^+ = 25$ and 70.

The detail of the velocity fluctuations in the vicinity of the riblets is illustrated by figure 3.10, which compiles the statistical values of the fluctuations conditioned both to the y coordinate and the spanwise position above the riblet. The detail of the fluctuations near the riblets agree well, and the differences are due to our slightly higher values away from the wall, reported above, which change the scale of the results slightly.

3.4.5 Effect of channel dimensions and grid resolution on the DNS of channels with blade riblets

As a final test, we have replicated cases 10S and 17S while independently doubling N_x, N_{z_r}, and the length and width of the channel, in the simulations 10FX to 17DZ, summarized in table 3.1. This simulations were conducted to check that our base set was

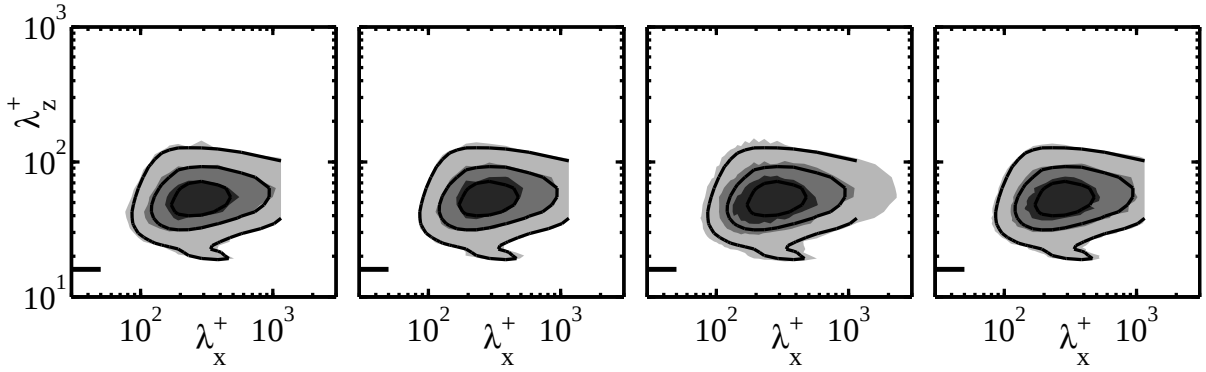

Figure 3.12: Spectral energy density of the wall-normal velocity, $k_x k_z E_{vv}$, at $y^+ \approx 5$. From left to right, simulations 10FX, 10FZ, 10DX, and 10DZ. The contour increments are $0.0015\,u_\tau^2$. Solid lines correspond to the original simulation 10S.

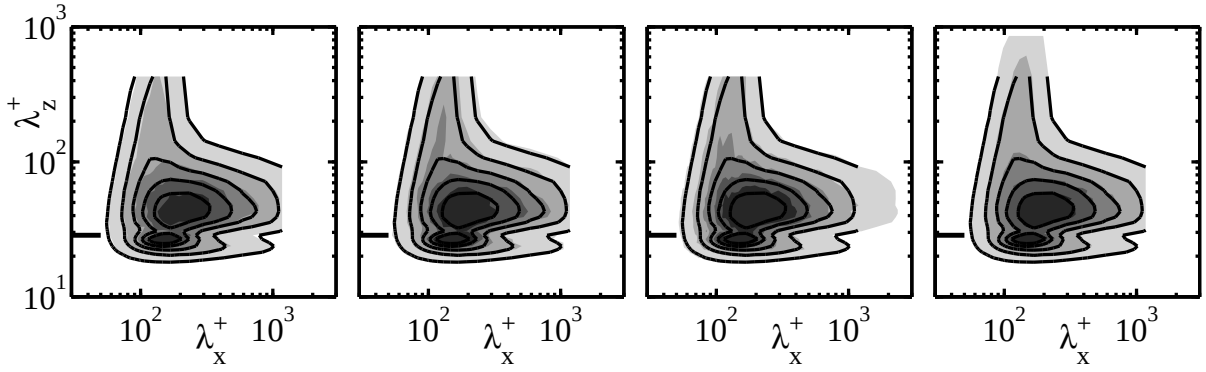

Figure 3.13: Spectral energy density of the wall-normal velocity, $k_x k_z E_{vv}$, at $y^+ \approx 5$. From left to right, simulations 17FX, 17FZ, 17DX, and 17DZ. The contour increments are $0.003\,u_\tau^2$. Solid lines correspond to the original simulation 17S.

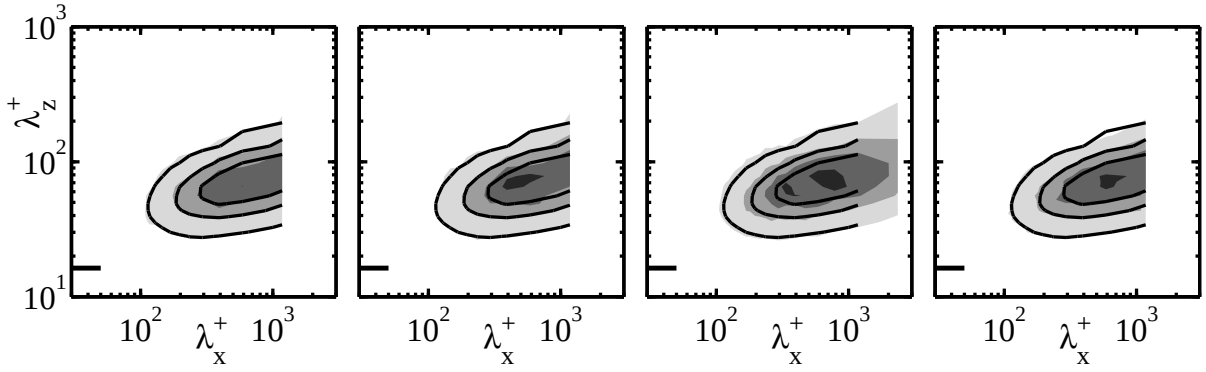

Figure 3.14: Spectral density of the Reynolds stress, $-k_x k_z E_{uv}$, at $y^+ \approx 5$. From left to right, simulations 10FX, 10FZ, 10DX, and 10DZ. The contour increments are $0.008\,u_\tau^2$, starting at $0.004\,u_\tau^2$. Solid lines correspond to the original simulation 10S.

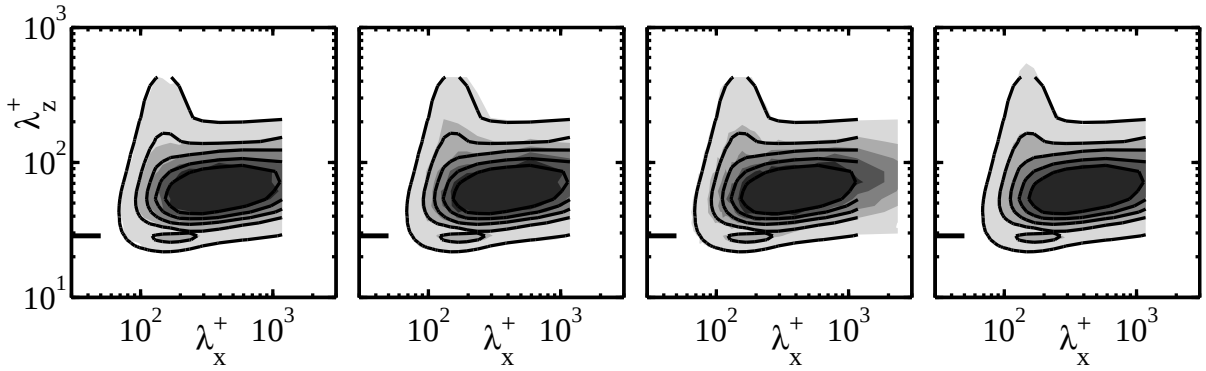

Figure 3.15: Spectral density of the Reynolds stress, $-k_x k_z E_{uv}$, at $y^+ \approx 5$. From left to right, simulations 17FX, 17FZ, 17DX, and 17DZ. The contour increments are $0.008\,u_\tau^2$, starting at $0.004\,u_\tau^2$. Solid lines correspond to the original simulation 17S.

converged with respect to the grid and box size.

The increase of the resolution in the spanwise direction in the riblet blocks has been used to test in particular whether the flow around the riblets was correctly represented. Given the uniformity of the riblets in the streamwise direction, we can expect that the wall roughness only requires a high resolution in the cross plane, although that would not hold for a more general, three-dimensional roughness. The conditional cross-flow in and immediately above the riblet grooves, obtained as discussed in §5.1, is portrayed in figure 3.11 for cases 10FZ and 17FZ, compared with the original cases 10S and 17S. There is a good agreement between the standard and finer resolutions, so we can conclude that 24 collocation points per riblet are sufficient to represent the flow around our $t_r/h = 0.25$ blades.

In figures 3.12 and 3.13, we portray the spectral distribution of the energy carried by the wall normal velocity for cases 0S and 17S, compared with the distributions for the corresponding cases with increased resolution and box size. The same is done for the Reynolds stress in figures 3.14 and 3.15. We will see in §5.2 that those distributions are greatly affected by the presence of riblets and their size, and are therefore an illustrative representation of the flow. Beyond a greater noise in most of the validation cases, which is due to the smaller simulation time, we observe good agreement, that confirms that the dimensions of our original set of simulations is adequate and their results can be considered converged.

Chapter 4

Results from two-dimensional models

In this chapter we present results from two-dimensional models for the flow over riblets. These results are mainly from Stokes regime simulations for the determination of protrusion heights, which fully account for the performance of riblets in the viscous regime, as discussed in §2.1. For a few representative riblets, we analyze the effect of some key geometric parameters, like groove depth and tip rounding, and flow conditions, like yaw. Additionally, we investigate the validity of the extension of the original model of the protrusion-height of Bechert & Bartenwerfer (1989) and Luchini *et al.* (1991) into the nonlinear regime, also commenting on the impact of the different geometric parameters under non-viscous conditions.

Sketches of two of the configurations that we study can be seen in figure 4.1. The first one is typical of the conventional 'grooved' riblets that have been extensively studied experimentally (Bechert *et al.*, 1997*b*), while the second is a novel one based on fibers laid anisotropically above a smooth surface.

4.1 Results of simulations in the viscous regime

We first undertake the simulation of the flow over riblets in the Stokes regime. Due to the relatively small computational cost of these simulations, it is possible to conduct extensive parametric studies for several configurations, studies that would be prohibitive if the actual turbulent flow were to be simulated. We are thus able to analyze the effect of different geometric parameters on the viscous performance. We give our results in terms of the 'protrusion height' Δh defined in §1.1, and discuss the extrapolation of these results to $DR_{\max}$ using the scaling with ℓ_g^+ proposed in §2.2.

Figure 4.2 shows two examples of the steady flow fields to which our simulations

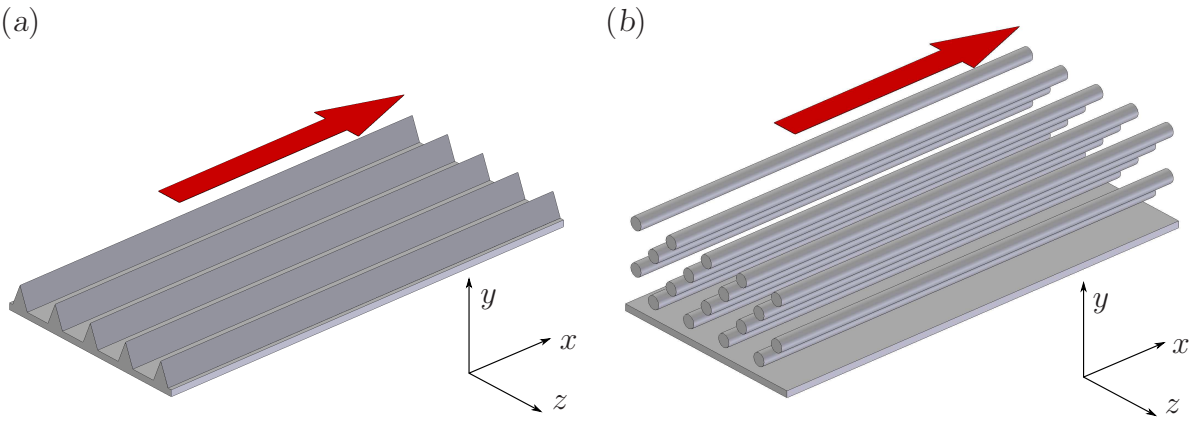

Figure 4.1: Different riblet geometries. (*a*) Conventional trapezoidal grooves. (*b*) Fiber riblets. The red arrows represent the direction of the mean flow driven by the shear S_x.

converge. For each geometry, comparing the figures for the streamwise and transverse flows we can qualitatively appreciate how the former penetrates more deeply into the grooves than the latter, resulting in positive protrusion heights. The offset between the two shears can be more clearly distinguished in figure 4.3, where the profiles for u and w are plotted for both configurations above the riblet peaks and valleys. As the height y above the riblets increases, the profiles of u above the peaks and above the valleys merge into a single, linear curve, and the same is true for the cross-flow w. The separation between the curves of u and w, once they become linear, is actually Δh.

4.1.1 The effect of groove depth

The effect of groove depth on turbulent drag reduction was studied extensively in Bechert *et al.* (1997*b*) for blade riblets. They observed that, in spite of the protrusion height increasing monotonically with groove depth, the maximum drag reduction was achieved for $h/s = 0.5$. To analyze the effect of groove depth in the viscous limit, we have simulated the Stokes flow over riblets with trapezoidal grooves of different h/s, with peak angles of 45° and 60°. These trapezoidal riblets were proposed by Bechert *et al.* (1997*b*) as a compromise between good performance and industrial realizability, since they are easier to manufacture and sturdier than blades, but still outperform triangles.

The simulations were run in two-dimensional domains containing a single riblet with peak angle α and height h. The domains were of size $s = 1$ in z and $y_{\max} = 2s$ in y, except for those cases with $h/s \leq 0.2$, for which $y_{\max} = s$. Each $s \times s$ square in the domain contained 256×256 grid points.

Results for the conventional protrusion height, $\Delta h/s$, are portrayed in figure 4.4(*a*).

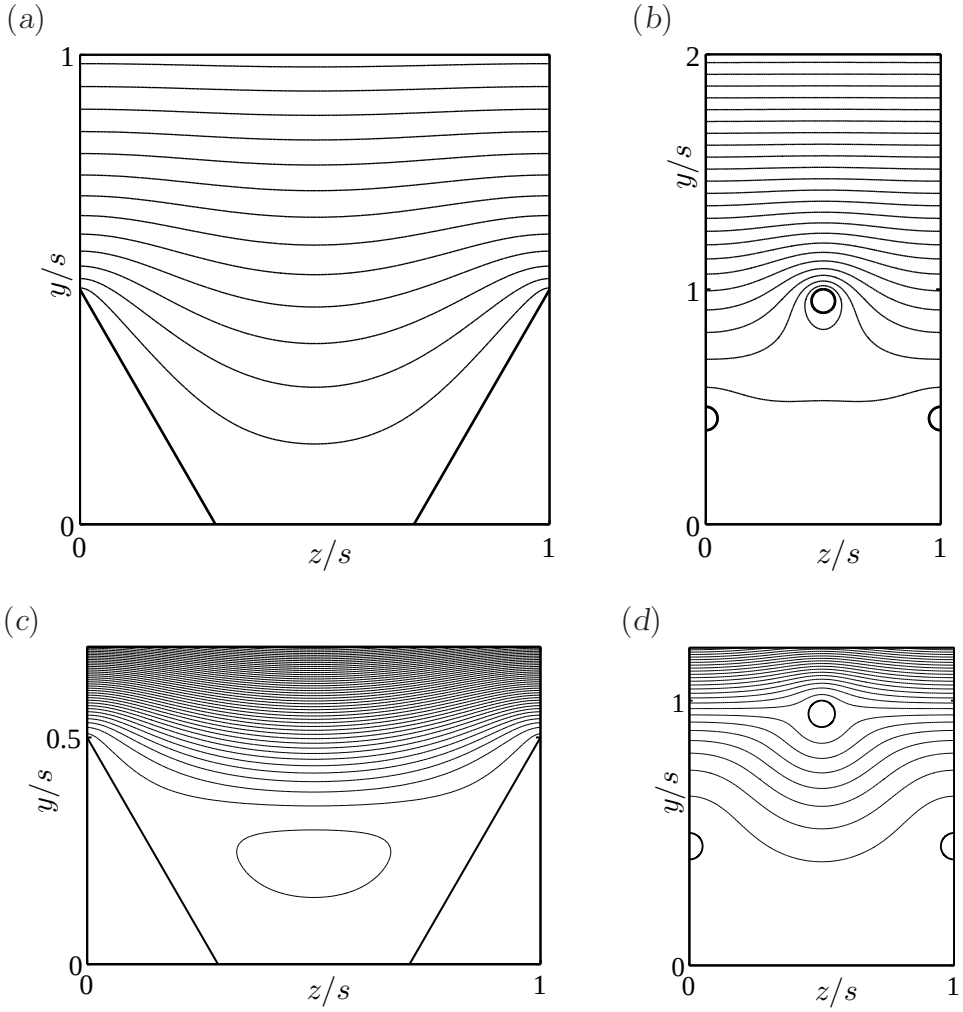

Figure 4.2: Typical velocity fields for (a,c) trapezoidal and (b,d) fiber riblets in the viscous regime. (a) and (b) are evenly spaced streamwise velocity isocontours, (c) and (d) crossflow streamfunction contours.

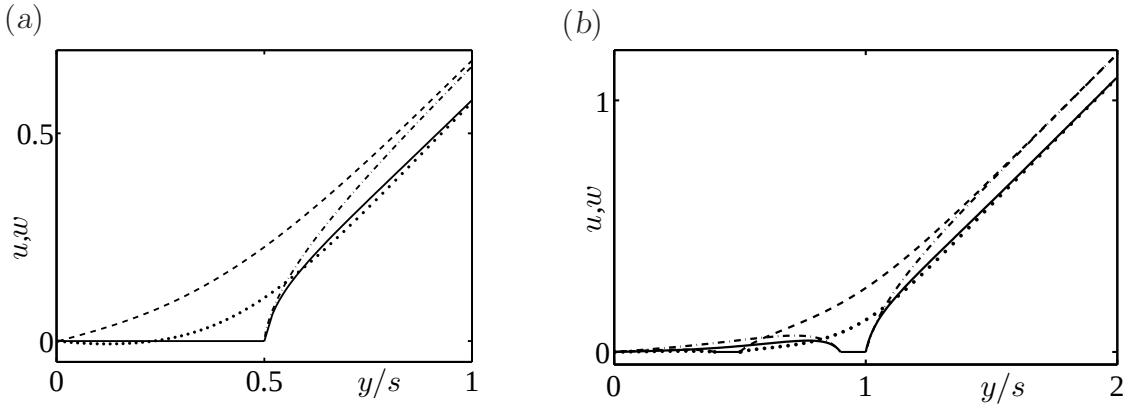

Figure 4.3: Velocity profiles for the cases of Figure 4.2. (a) corresponds to the conventional case, and (b) to the fiber one. - - - -, u above a riblet valley; – · – , u above a riblet peak; ·····, w above a riblet valley ; ——, w above a riblet peak.

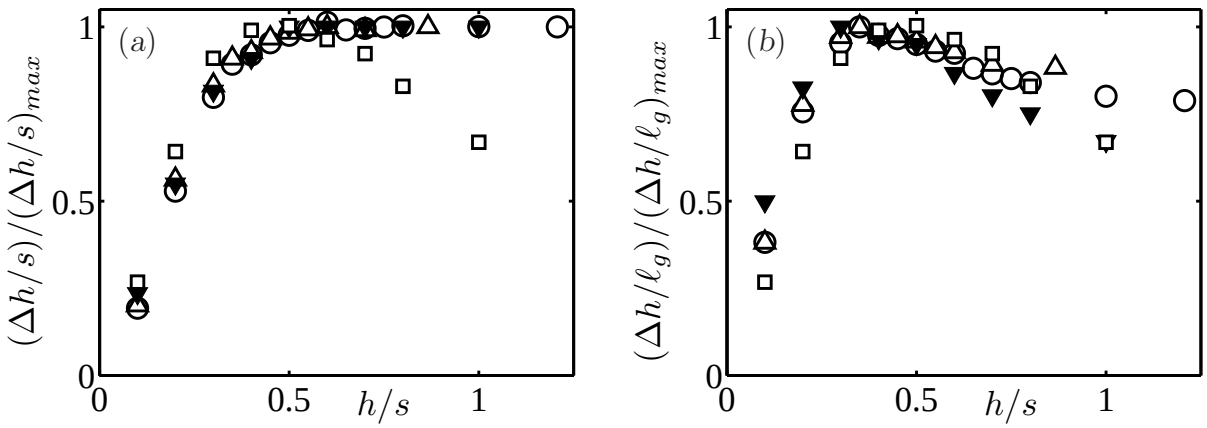

Figure 4.4: Influence of the groove depth on the viscous performance of riblets. Protrusion heights are scaled (*a*) with the riblet spacing, $\Delta h/s$; (*b*) as proposed in §2.2, $\Delta h/\ell_g$. ○, trapezes with peak angle $\alpha = 45°$ △, trapezes with $\alpha = 60°$ ▼, protrusion heights of blade riblets, estimated from experimental viscous slopes, from Bechert *et al.* (1997*b*); □, experimental $DR_{\max}$ for the same blade riblets. To enhance comparison, each set of results has been scaled so its maximum is unity.

They show that the groove depth has a negligible effect for $h/s \geq 0.5$, but the protrusion height decreases rapidly for smaller h/s. The figure includes results from the experimental viscous slopes of blade riblets from Bechert *et al.* (1997*b*). They agree incredibly well with our simulations, even if the two geometries, blades and trapezes, are not the same, implying that the effect of groove depth on the viscous performance is similar for the different geometries.

To illustrate that viscous and optimum performance are not strictly correlated, experimental results for $DR_{\max}$ from Bechert *et al.* (1997*b*), are also included. The comparison shows that the high values of $\Delta h/s$ for the deeper grooves do not translate in practice into good optimum performance. This is due to the early breakdown of the viscous regime for deep grooves. If the protrusion heights are scaled with ℓ_g instead, as proposed in §2.2, the asymptotic behavior for $h/s \geq 0.5$ is lost, but the rescaled protrusion heights $\Delta h/\ell_g$ correlate much better with $DR_{\max}$, as shown in figure 4.4(*b*).

4.1.2 The impact of tip rounding

Riblet erosion is a major concern for the industrial applications. Walsh (1990*a*) measured drag reductions for triangular riblets with rounded peaks, finding a performance loss of up to 40% for a tip radius $R \approx 0.08s$. He also found no significant performance

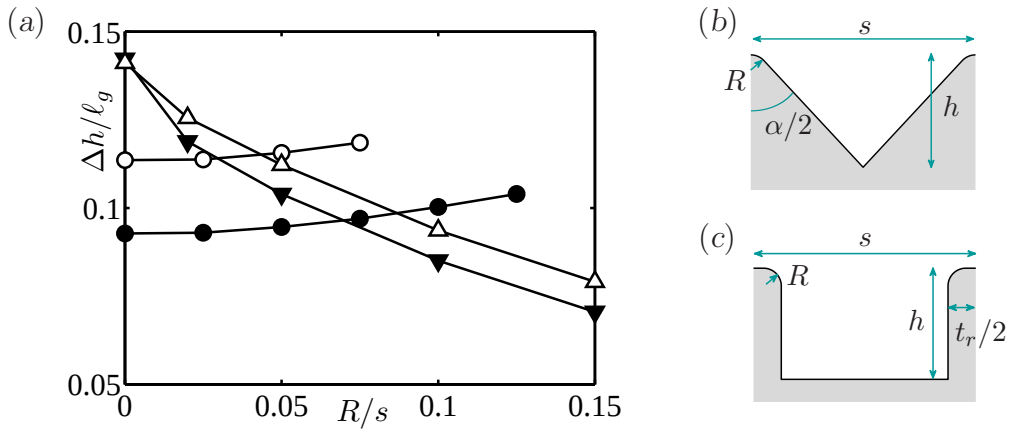

Figure 4.5: (*a*) Protrusion height of rounded peak riblets, scaled with the characteristic length scale $\ell_g = \sqrt{A_g}$, as a function of the peak radius of curvature. ▼, Triangular riblet with tip angle $\alpha = 60°$; △, triangular riblet, $\alpha = 45°$; ○, blade riblet, $h/s = 0.5$, and thickness $t_r/s = 0.15$; ●, blade riblet, $h/s = 0.5$ and $t_r/s = 0.25$. (*b*) Geometry of rounded-peak triangular riblets. (*c*) Geometry of rounded-peak blade riblets.

degradation from the rounding of the groove bottoms.

We can infer from the discussion in §2.2 that the details of the tip geometry should not affect significantly the viscous breakdown, because they barely modify the groove cross-section. That is supported by the experiments of Bechert *et al.* (1997*b*), who tested blade and scalloped geometries in which only the tip thickness changed (see for instance the experiments portrayed in figure 1.2(*a*)). The maximum drag reductions changed with the tip thickness, but not the optimum s^+, suggesting that the differences in performance were due to the changes in the slope of the drag-reduction curve in the viscous regime. If that is the case, the influence of the tip details should be restricted to a decrease in the protrusion height.

Viscous results for different geometries with tip rounding are presented in figure 4.5. Again, these simulations were run in two-dimensional domains containing a single riblet with peak angle α and nominal height h, although the actual height of the triangular riblets is in fact lower, since the straight sides of the riblet are connected at the peak by a circular segment of radius R tangent to both, instead of meeting at $y = h$. The domains were of size $s = 1$ in z, and $y_{\max} = 2\,s$ in y. Each $s \times s$ square in the domain contained 128×128 grid points, except in the cases with the two smallest radii, $R/s \leq 0.05$, for which the spatial resolution was doubled in each direction to resolve the circular corners.

In agreement with Walsh (1990*a*), the triangular riblets show a dramatic performance decrease but, surprisingly, the protrusion heights for the flat-top blades tested –which perform worse with no rounding than the sharp triangles– change little with tip rounding,

and even increase slightly as the rounding increases. It is well established that sharper riblets have higher protrusion heights (Luchini *et al.*, 1991; Bechert *et al.*, 1997*b*). Tip rounding reduces the sharpness of initially sharp configurations, and degrades their performance. The new result in figure 4.5 is that the rounding of the tips of initially blunt blades improves their performance. Although unexpected, this result is not completely contradictory with the previous knowledge, since the rounding of the corners of rectangular blades does indeed sharpen their otherwise flat tops. For practical applications in which erosion is an issue, it is probably preferable to use riblets which do not depend initially too much on the sharpness of their tips.

4.1.3 The effect of yaw

The linearity of the viscous regime allows us to compute the effect of riblet yaw. Assume that the riblets are aligned at an angle θ with respect to the free stream. We would like to determine the offset between the virtual origins defined in (1.2) and (1.3) for the streamwise and spanwise velocities. Because of the linearity of the problem, we can project those velocities to a frame of reference aligned with the riblets, with the longitudinal and transverse velocities being

$$u_L = \quad u\cos\theta + w\sin\theta \quad = (S_x\cos\theta + S_z\sin\theta)\,(y - \Delta_L), \tag{4.1}$$

$$u_T = \quad -u\sin\theta + w\cos\theta \quad = (-S_x\sin\theta + S_z\cos\theta)\,(y - \Delta_T), \tag{4.2}$$

where Δ_L and Δ_T are the virtual origins for perfectly aligned riblets. The corresponding offset would be $\Delta h_0 = \Delta_T - \Delta_L$. After some algebra we obtain

$$\Delta h(\theta) = \Delta_w - \Delta_u = \left(\cos(2\theta) + \frac{S_z^2 - S_x^2}{2S_xS_z}\sin(2\theta)\right)\Delta h_0. \tag{4.3}$$

The correction factor depends on the ratio of the spanwise to streamwise shear, which could be estimated from the experimental values of the streamwise vorticity fluctuations at the wall. However, once (4.3) is averaged over time, the shear-dependent factor drops out, because of antisymmetry. The final result is

$$\langle\Delta h\rangle(\theta) = \cos(2\theta)\Delta h_0. \tag{4.4}$$

This agrees with the observation in Walsh (1990*b*) that the performance of riblets degrades little up to yaw angles of 15°. Equation (4.4) predicts that the degradation at that angle should be about 13%. At $\theta = 45°$, riblets would lose all their efficiency. At 90°, they would increase drag as a regular rough wall.

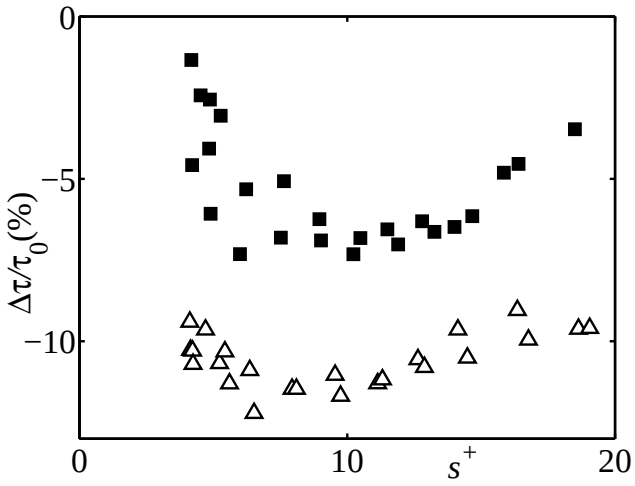

Figure 4.6: Drag reduction of the seal fur surface from Itoh *et al.* (2006). △, seal fur; ■, trapezoidal, flat-peak riblets, also from Itoh *et al.* (2006).

On the other hand, that simple dependence does not extend away from the viscous regime. Hage *et al.* (2000) reported on the effect of yaw on riblets near the optimum spacing, and found a typically larger geometry-dependent degradation than in the viscous case, increasing strongly as s^+ exceeds the optimum value. Since the viscous breakdown is an indication of the effect of nonlinearity on the riblets, it is not surprising that the linear predictions do not apply in that limit.

4.1.4 Fiber riblets

Based on the ideas of Kramer (1937), Bruse *et al.* (1993) proposed a riblet-like surface formed by a layer of fibers over a smooth wall, lined up in the direction of the flow. Similarly to the fences in blade riblets, the fibers would keep the turbulence away from the smooth surface, preventing its exposure to high momentum flow and reducing the friction. Bruse *et al.* (1993) conducted some experiments to study the influence of the fiber radius and distance to the wall, but the results were discouraging, as the drag reductions obtained were nearly negligible. Goldstein *et al.* (1995) conducted simulations on similar setups, obtaining also modest results.

More recently, Itoh *et al.* (2006) have tested the drag reduction properties of seal fur, also obtaining a riblet-like behavior. The drag reduction of these experiments is depicted in figure 4.6, where s^+ has been obtained from the wavelength identified by Itoh *et al.*, by analogy, as the 'riblet pitch'. This fibrous surface appears to achieve roughly a 12% maximum drag reduction, and also to have a wider range of s^+ with nearly optimum

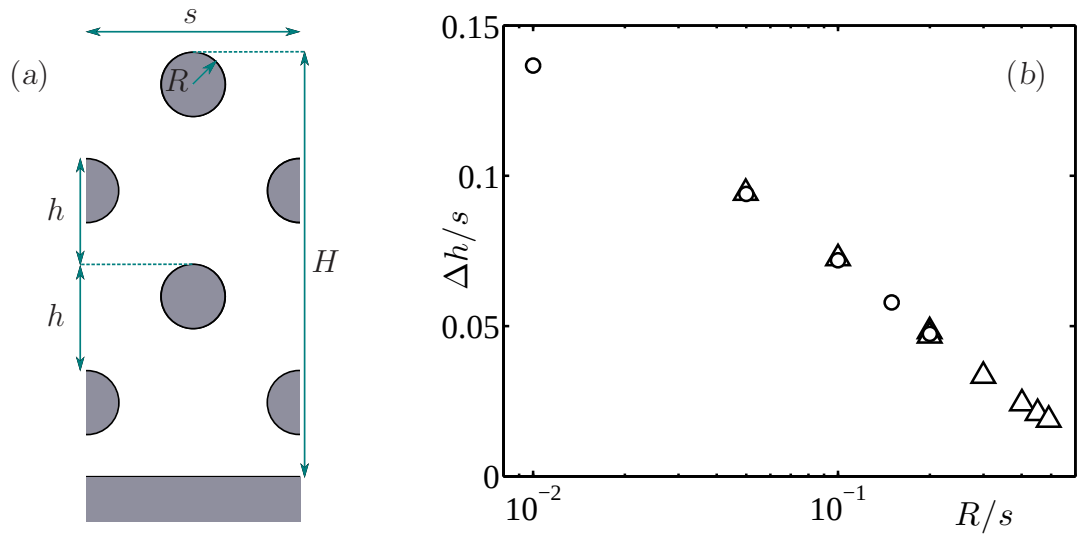

Figure 4.7: (*a*) Sketch of the fiber riblets simulated. (*b*) Protrusion height of fiber riblets as a function of the fiber radius. ○, results obtained with the numerical method outlined in §3.1.1. △, finite-elements results for the Laplacian and biharmonic equations, for u and the streamfunction of the crossflow respectively (L. González, private communication).

performance than conventional riblets. Itoh *et al.* attributed this wider range to the existence of a continuous distribution of spanwise 'riblet' wavelengths, rather than a single discrete one. However, more experiments on such surfaces would be required to confirm that the drag reductions achieved are only due to the surface geometry, and not to other phenomena such as hydrophobicity.

Based on these ideas, we have proposed a novel, unconventional riblet, consisting of fibers aligned in the streamwise direction, creating a layer of anisotropically porous material (García-Mayoral & Jiménez, 2007). The fibers, of radius R, are arranged in several staggered rows, as sketched in figure 4.7(*a*). Because of its anisotropy, the fibrous layer hinders the cross-flow more than the streamwise flow, creating a positive protrusion height much like conventional riblets. The topmost row of fibers forms then the 'riblet peaks', and the next one the 'valleys', resulting for our arrangement in a 'height' $h = 0.5s$. This value is just a tentative choice, loosely based on the optimum for blade and trapezoidal riblets found by Bechert *et al.* (1997*b*). As we mentioned in §2.2, unconventional riblets do not appear to show the same scaling for their optimum as conventional ones, so the optimum fiber arrangement could be entirely different. For the same reason, the scaling with ℓ_g^+ would not offer any particular advantage, so we have maintained the classical one with s. In any case, the effect should be roughly similar to that of the seal fur studied by Itoh *et al.* (2006), or to the fibrous surfaces proposed by Bechert's group (Bruse *et al.*,

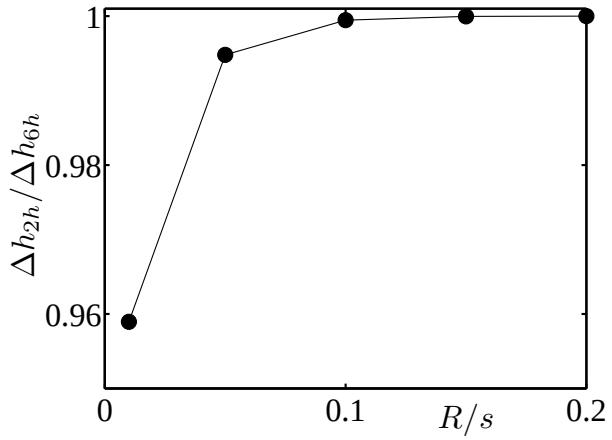

Figure 4.8: Ratio between the protrusion heights of shallow and deep fiber linings, $H = 2h$ and $H = 6h$ respectively, as a function of fiber radius.

1993; Bechert *et al.*, 1997*a*), although probably with more open space than the former, and somewhat less than the latter. In our simulations, the domain is bounded at the bottom by a no-slip surface at a distance H from the top of the uppermost fiber.

To study the influence of the fiber thickness on the protrusion height, we conducted simulations with fiber radii ranging from $R/s = 0.01$ to $R/s = 0.20$. The domains, periodic with spanwise wavelength $z = s$, reach to a maximum height $y_{\max} = s$ measured from the top of the fibers. Each $s \times s$ square contains 128×128 grid points, although the resolution was increased to 512×512 for the case $R/s = 0.01$ to capture the detail of the finer fibers. In most simulations, the depth of the lining was chosen $H = 6h$, so that it contained six layers of fibers. It will however be seen below that, except perhaps for the case $R/s = 0.01$, there is very little difference between these deep linings and very shallow ones with just two layers, $H = 2h$.

The results are given in figure 4.7(b), and show that thinner fibers produce larger protrusion heights. The logarithmic behavior of the protrusion height with R/s is not completely unexpected, because the drag of cylinders, both parallel and perpendicular to the flow, depends logarithmically on R (Batchelor, 1994). Nevertheless, the analytic theory for the present case is incomplete, and the evidence for a logarithmic limit for vanishing R is at present numerical.

To determine the influence of the number of rows of fibers in the staggered arrangement, we compare the protrusion heights obtained with two and with six fiber layers, $H = 2h$ and $H = 6h$ respectively. As we have mentioned, the shallow arrangements of Bruse *et al.* (1993) produced poor results, so we should expect to require more than one row of fibers if we are to obtain a better performance. Figure 4.8 represents, for several

values of the fiber radius, the ratio between the protrusion heights for the two values of H considered. In general, deeper linings perform better, but the effect is small. The largest relative decrease is 4% for the shallower lining of fibers with $R/s = 0.01$. For $R/s = 0.05$ it is less than 1%, and for $R/s \geq 0.10$ it is negligible.

According to our results, the fiber linings yield protrusion heights similar to those of conventional riblets, but they seem to be more geometrically permissive. It follows from figure 4.7(b) that fibers of diameter $2R = 0.02s$ achieve $\Delta h/s = 0.137$, a higher viscous performance than optimum blade riblets ($h/s = 0.5$) with blade thickness $t_r/s = 0.02$, which yield $\Delta h/s = 0.113$. They even perform better than infinitely thin, infinitely deep, blade riblets, which yield $\Delta h/s = 0.132$ (Bechert *et al.*, 1997*b*). To get the same performance as a more technologically relevant 60° triangular riblet would require a diameter $2R \approx 0.1s$. As shown in figure 4.5, a triangular riblet with a tip rounding of the same radius would have its performance degraded by 25% with respect to an ideal triangle.

However, to determine $DR_{\max}$, which is after all the quantity of practical interest, it would be necessary to determine how early do the fibers experience the viscous breakdown. In the worst case, fibers could behave like infinitely deep blades. As we have just mentioned, infinite blades have an optimum protrusion height, but are also known to have an extremely early viscous breakdown (Bechert *et al.*, 1997*b*), so they yield a low DR_{max}.

4.2 Effect of convection on the two-dimensional flow

In this section, we investigate the effect of nonlinearity on the protrusion height as a possible cause for the breakdown of the viscous regime, as discussed in §1.2. We conduct simulations preserving the two-dimensional character of the flow, but otherwise including nonlinear effects. The strength of the nonlinearity is determined by the riblet spacing $s_z^+ = \sqrt{Re_z} = \sqrt{S_z/S_x}s^+$, which was shown in §3.1.1 to be of the order of $s_z^+ \approx s^+/2$. Since experimentally the linear behavior breaks down for $s^+ \approx 10 - 20$, the test of the present model would be whether the same is true here for $s_z^+ \approx 5 - 10$.

Figures 4.9 and 4.10 are the nonlinear analogues of Figures 4.2 and 4.3. In figure 4.9, we can appreciate how the nonlinearity breaks the symmetry of the flow that existed in the viscous case. On the other hand, the penetration depths of the streamwise and of the transverse flows inside the grooves do not change noticeably, at least for the range of s_z^+ in which we are interested. Figure 4.10 shows the velocity profiles at different locations across the riblet, as in figure 4.3.

Figure 4.11 represents the typical behavior of Δh under varying s_z^+ for a triangular

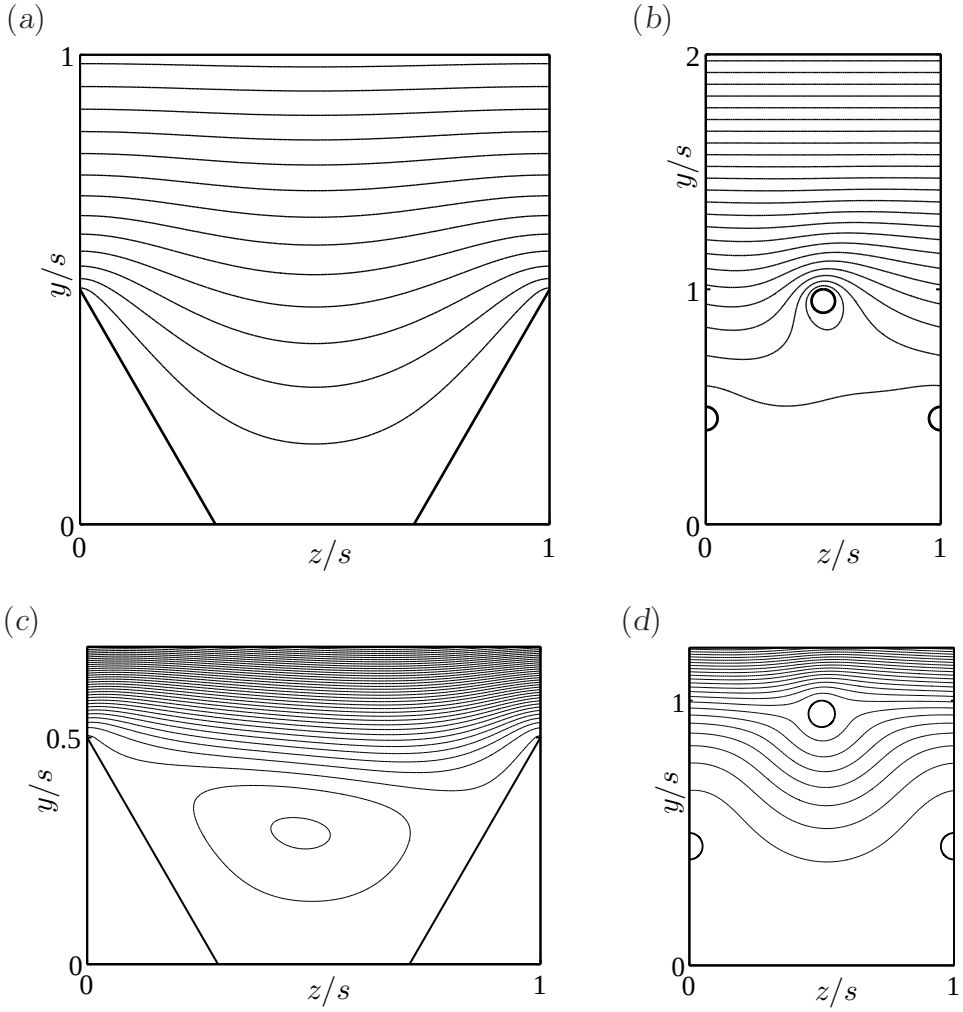

Figure 4.9: Typical velocity fields for (a,c) conventional and (b,d) fiber riblets in the nonlinear regime. Contours and conditions are as in figure 4.2, except that $s_z^+ \approx 8.2$ for the trapezoidal riblet and 6.5 for the fibers.

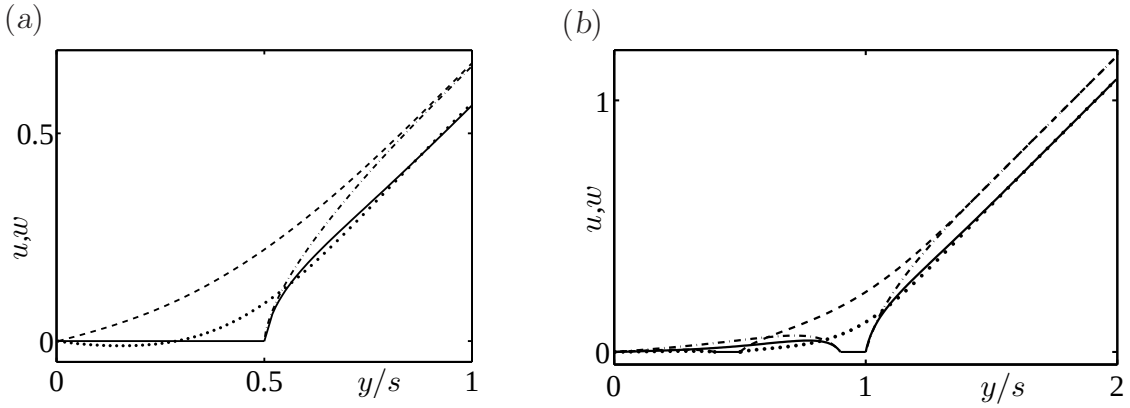

Figure 4.10: Velocity profiles for the cases of figure 4.9. (a), conventional trapezoidal riblet; (b) fiber riblet. - - - -, u above a riblet valley; – · – , u above a riblet peak; ·····, w above a riblet valley ; ——, w above a riblet peak.

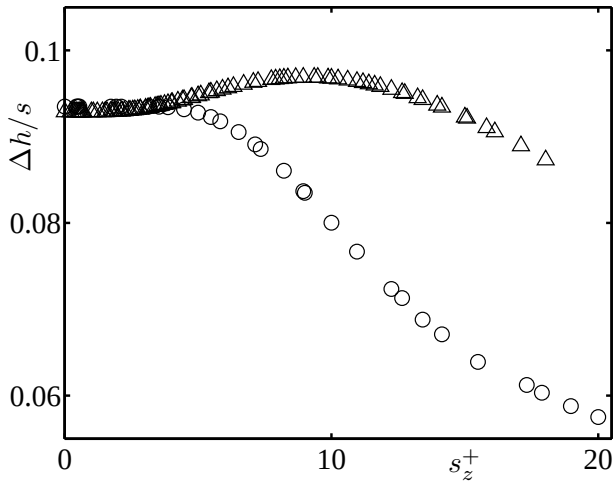

Figure 4.11: Protrusion heights of a triangular and a fiber riblet, as a function of $s_z^+ \approx s^+/2$. $\triangle$, 60° triangular riblet; $\circ$, $R/s = 0.05$ fibers.

and for a fiber riblet of similar Stokes protrusion heights. The influence of the nonlinear effects is smaller on the triangular riblet, and is slightly beneficial up to $s_z^+ \approx 15$, reaching its maximum for $s_z^+ \approx 10$. Fiber riblets are more sensitive to nonlinear effects, and the effect is always deleterious. In both cases the effect is nevertheless small, and changes of the order required to explain the experiments are not reached until $s_z^+ \approx 10 - 20$, which is too large. We will see in the next two subsections that similar results are obtained for all the other configurations tested. It would appear from these results that the experimental observations are more likely to be explained by processes acting at lower Reynolds numbers than the present one.

In fact, of all the assumptions made when defining the protrusion height, the one that looks riskier for non-zero Reynolds numbers is the homogeneity of the spanwise shear. The buffer layer extends from $y^+ \approx 10$ to $y^+ \approx 60$, and its lower region is dominated by streaks whose lengths and widths are of the order of 1000×100 wall units, and by quasi-streamwise vortices centered at $y^+ \approx 20$ with diameters $2R^+ \approx 30$. The vortices are responsible for the spanwise shear and, while it might be reasonable to assume that they are locally seen as a uniform shear by riblets whose size is $s^+ = O(1)$, the same assumption is less justified when $s^+ \approx 10$, roughly of the order of the vortex radii. The same can be said about the stationarity of the problem. When the s_z^+ is larger than unity, the characteristic evolution time for the flow around riblets is by definition s_z^+. The typical length of the vortices in the buffer layer is $100 - 200$ wall units, and their advection velocity is $C_u^+ \approx 10$. That gives a persistence above any given point of the

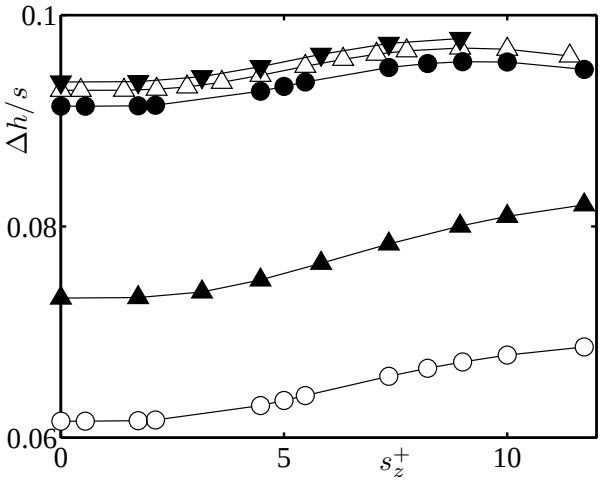

Figure 4.12: Protrusion heights of 60° trapezoidal groove riblets, as a function of $s_z^+ \approx s^+/2$. ▲, $h/s = 0.3$; ●, $h/s = 0.5$; ▼, $h/s = 0.7$; △, $h/s = \sqrt{3}/2$; ○, 90° triangular riblet ($h/s = 0.5$)

order of $T^+ \approx 10 - 20$, which begins to be of the same order as the riblet time as soon as $s^+ \gtrsim 10$. This is consistent with the results portrayed in figure 4.11, which show some nonlinear effects, but only small ones and, specially, of different signs for different riblets. It appears most probable that the main reason for the nonlinear degradation of riblet performance with s^+ is their interaction with the nonuniform flow above.

Nevertheless, an interesting conclusion from the present study is that, away from the Stokes regime, the ability of fibers to impede the flow in the cross-plane degrades more rapidly than for conventional riblets.

4.2.1 Conventional riblets

In order to elucidate whether convective effects have a similar influence on different trapezoidal and triangular riblets, we have conducted a series of simulations for different groove parameters and shapes. Due to limitations of computation time, we have used coarser grids than in §4.1.1. In these convective simulations, each $s \times s$ square in the domain contains 128×128 grid points. The resulting errors are still small, and do not modify the trend with the Reynolds number, which is what we are interested in.

The results of our simulations can be seen in Figure 4.12. Trapezoidal 60° riblets with $h/s = 0.5$ and $h/s = 0.7$ show nearly the same behavior as the corresponding equilateral triangular riblet ($h/s = \sqrt{3}/2$). The trends of the trapeze with $h/s = 0.3$ and the 90° triangular riblet seem to be analogous, but evolve at a slower rate with s_z^+ than in the

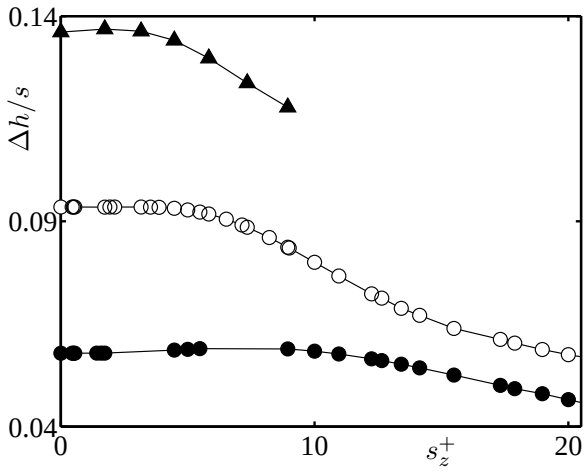

Figure 4.13: Protrusion height of different fiber riblets, as a function of $s_z^+ \approx s^+/2$. ●, $R/s = 0.15$; ○, $R/s = 0.05$; ▲, $R/s = 0.01$.

previous cases. We have not extended our simulations enough to confirm whether those two curves also reach a maximum at $s_z^+ \approx 15$ since, as discussed above, the information for $s_z^+ > 10$ would not be meaningful.

4.2.2 Fiber riblets

As with conventional riblets, we have conducted a series of simulations for fiber riblets with different geometries, to establish if convective effects have a similar influence for different configurations. We have tested fiber riblets with different sizes R/s and for different lining depths.

Figure 4.13 portrays results for three riblets with different fiber radii. The grid resolutions and domain sizes for these simulations were the same as those used for the corresponding cases in §4.1.4. As in the case of triangular riblets, the behavior of Δh with s_z^+ is similar for the three different radii, but evolves at a slower rate for the thicker fibers. For the thinner fibers, which yielded the best viscous performance, the degradation is more severe. This suggests that the sensitivity to convective effects increases with fiber thinning.

The influence of the lining depth is portrayed in figure 4.14. For fibers with $R/s = 0.01$ and $R/s = 0.05$, the figure depicts evolution with increasing s_z^+ of the ratio between the protrusion heights of $H = 2h$ and $H = 6h$ linings. For $R/s = 0.01$, the difference between the two depths is somewhat reduced as the flow becomes more nonlinear. In

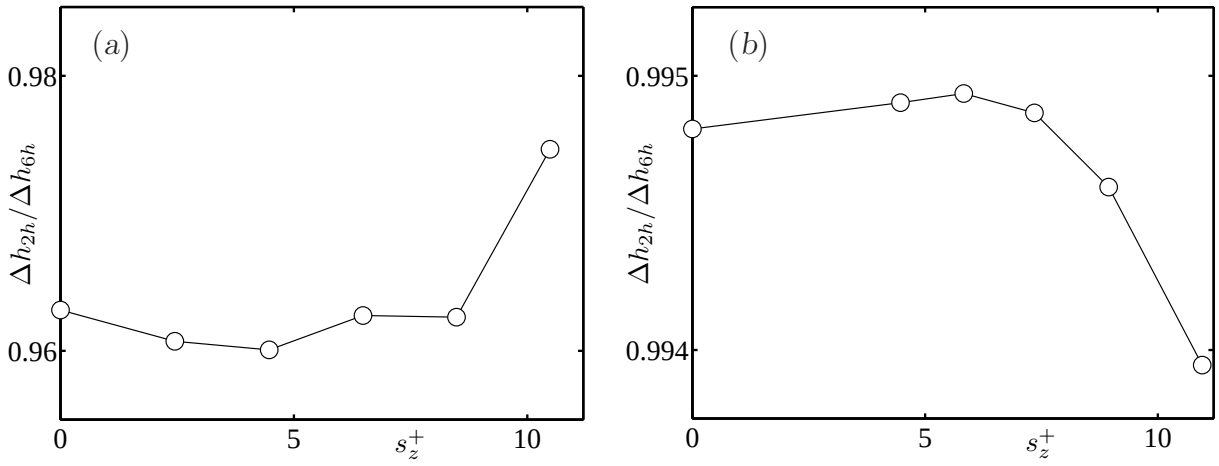

Figure 4.14: Ratio between the protrusion heights for linings with two and six rows of fibers, $H = 2h$ and $H = 6h$, as a function of s_z^+. (*a*) $R/s = 0.01$. (*b*) $R/s = 0.05$. Notice the very narrow vertical scale.

the case $R/s = 0.05$, the difference seems to grow with s_z^+, but the increment is in any case negligible. We can infer from these results that the effect of lining depth is also insignificant for the nonlinear flows, at least in the range $s_z^+ < 10$ of practical interest.

Chapter 5

Results from DNSs of channels with blade riblets at $\mathbf{Re}_\tau \approx 180$

In this chapter we discuss our DNS results for the rectangular riblets sketched in figure 5.1 at $\mathrm{Re}_\tau = \delta^+ \approx 180$. The wall geometry chosen for our experiments consists of rectangular riblets with depth-to-spacing ratio $h/s = 0.5$, blade thickness $t_r/s = 0.25$, and $\ell_g/s \approx 0.61$, for which Stokes calculations give a protrusion height $\Delta h/\ell_g = 0.095$, and an offset for the streamwise velocity $\Delta_u/\ell_g = -0.16$. From a drag-reduction perspective, this geometry is far from optimal, with a maximum expected reduction of about 6%, but it requires a lower numerical resolution than sharper configurations, reducing the computational cost, and improving the accuracy of the results. Previous DNSs of riblets (Choi *et al.*, 1993; Chu & Karniadakis, 1993; Stalio & Nobile, 2003; Orlandi *et al.*, 2006; El-Samni *et al.*, 2007) were usually conducted in channels with riblets in only one wall, with the opposite wall used as the reference to measure friction. However, although that arrangement may be useful in comparing channel simulations among themselves, it is inconvenient when trying to relate computations to experiments on boundary layers. If only one wall is ribbed, the flow is asymmetric, and the friction velocities are different for both walls. This leads to different friction Reynolds numbers and wall units at either side of the channel, which, if not taken into account, would lead to errors in the calculation of the riblet sizes s^+ or ℓ_g^+. It is also unclear which value should be used for the free-stream velocity in the friction coefficient, to make it comparable with boundary layers. These effects are negligible for moderate or high Reynolds numbers, but they can be substantial at the relatively low Reynolds numbers of most DNSs, especially when dealing with the relatively weak effects of most riblets. To avoid those potential errors, our simulations include riblets in both walls, and use as reference a smooth-wall channel with the same

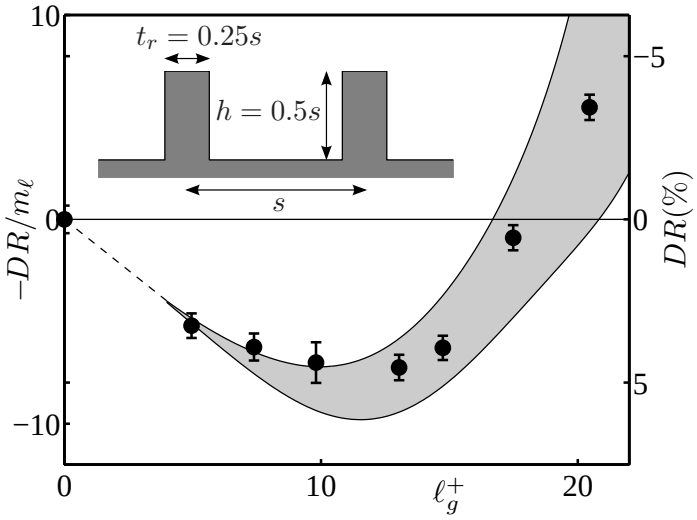

Figure 5.1: Drag-reduction results from DNSs of channels with the sketched rectangular riblets. ●, results normalized using equation (2.10), with protrusion heights obtained from a second-order finite-differences Stokes simulation with the same effective resolution as the DNSs, and the value for μ_0 from Jiménez (1994). The error bars have been estimated from the time-history of DR, following Hoyas & Jiménez (2008). The shaded area is the envelope of the experimental data in figure 2.3(d).

mass flux between the two planes defined by the riblet tips. We also take as reference velocity the one at the centerline.

This set of simulations was devised to cover the full drag reducing range, $0 \leq \ell_g^+ \lesssim 20$, and the target parameters for the eight simulations, summarized in table 5.1, were chosen accordingly. Figure 5.1 compares the drag reduction obtained for the numerical cases 0S to 20S with the experimental data discussed in §2.2, with reasonably good agreement.

The definition of the friction coefficient deserves some comment. It was noted by Luchini (1995) that the friction coefficient of internal flows is harder to define than that of external boundary layers. In the latter case, a reasonable procedure is to normalize the wall friction with the free-stream velocity, which is also the quantity of interest in vehicular applications. In internal flows, the practical quantity is the mass-flow rate, but, if it is used to normalize c_f, there is an ambiguity as to which hydraulic radius should be used to convert the flow rate into a bulk velocity. Luchini (1995) remarked that different 'reasonable' choices could result in changes of the friction coefficient comparable to those expected from the riblets themselves, with the neutral choice being measuring the hydraulic radius from the virtual origin Δ_u.

On the other hand, it follows from the discussion in §2.1 that the physically relevant

Case	ℓ_g^+	s^+	Re_τ	$c_f \times 10^3$	$DR(\%)$
0S	0	0	189.31	5.99	0
5S	4.95	8.09	185.37	5.80	3.26
7S	7.39	12.06	184.33	5.76	3.91
10S	9.80	16.01	183.47	5.73	4.39
13S	13.04	21.29	182.99	5.72	4.54
15S	14.74	24.07	183.91	5.75	3.94
17S	17.48	28.55	186.93	5.96	0.56
20S	20.46	33.41	191.42	6.20	-3.43
17DZ	17.51	28.59	187.23	5.97	0.31

Table 5.1: Parameters resulting from DNSs at $\mathrm{Re}_\tau \approx 180$. ℓ_g^+ is the square root of the groove cross-section; s^+ is the riblet spacing; Re_τ is the friction Reynolds number; c_f is the friction coefficient; and DR the drag reduction.

definition of drag change should be based on the offset ΔB of the logarithmic velocity profile, which, if we assume that surface manipulations only modify the near-wall region, is equivalent to the change in the maximum mean velocity U_δ^+. The only corrections are those associated with the denominator of (2.2), which depends weakly on the Reynolds number. That is why in this thesis we use the centerline velocity to normalize the friction coefficient, rather than the mass flux. The friction Reynolds number is kept approximately constant by the procedure of fixing the flux among the different cases, and the effect of any small change should only manifests itself in the change of c_{f0} in the denominator of (2.2), which would yield at most a 1% change in drag.

The friction itself is defined in terms of the mean pressure gradient P_x. In the case of smooth walls, the skin friction can be obtained by extrapolating to the wall the total stress, $\tau(y) = -\langle uv \rangle + \nu \partial_y \langle u \rangle$, which is linear in y with slope P_x. The brackets $\langle\rangle$ stand for averaging over wall-parallel planes and time. Equivalently, it follows from the integrated streamwise momentum equation that

$$2L_z \tau_w = -A_c P_x, \tag{5.1}$$

because the friction in both walls has to compensate the effect of P_x over the cross-sectional area $A_c = 2\delta L_z$. The result,

$$\tau_w = -\delta \, P_x, \tag{5.2}$$

can be derived either from the extrapolation of $\tau(y)$ or from (5.1).

In cases with riblets, the wall friction is not exerted at a constant y-plane to which $\tau(y)$ can be extrapolated, but we can use (5.1) as long as A_c is the real channel cross-section, including the open section of the grooves. Equivalently, since the total stress is still linear above the riblet tips, τ_w can be computed by extrapolating $\tau(y)$ to the level $y = \delta - \delta'$, where $A_c = 2\delta' L_z$, which is the y-plane at which a smooth wall would have to be located for a channel of area A_c. The resulting τ_w is the total friction exerted per unit streamwise length and channel span, and is thus the correct quantity to compare with the friction on a smooth wall when estimating drag reduction. For our test geometry, $\delta' = \delta + 3h/4$. Note that, if those corrections are not taken into account, and τ_w is estimated by extrapolating the total stress to $y = 0$, the relative error in c_f would be of order $(\delta - \delta')/\delta \sim h/\delta$. For typical values of $\Delta c_f/c_f \approx 0.1$, that error would only be negligible if $h/\delta \ll 0.1$, which is not our case.

5.1 The conditional flow

To elucidate the structure of the flow near the ribbed surface, we have compiled flow statistics conditioned on the spanwise position across the riblet. Figure 5.2(a) portrays the conditionally-averaged crossflow inside and immediately above a riblet groove, for several riblet sizes. The panel for $\ell_g^+ = 0$ is the two-dimensional Stokes crossflow used for the computation of the protrusion height. For non-zero values of ℓ_g^+, the crossflow is averaged over identical spanwise locations with respect to each riblet, as well as over time and x, but, since that procedure only recovers a weak secondary flow, the statistics are also conditioned on the mean direction of the crossflow in the plane immediately above the riblet tips. The flow over individual grooves is characterized as either 'rightwards' or 'leftwards', and the statistics for the two directions are combined by adding the specular image of the mean leftwards flow to the rightwards one. Note that this procedure generates statistics that are not periodic with the riblet spacing, because the flow over each riblet is conditioned to a particular orientation, while those over the neighboring ones are not.

Figure 5.2(a) shows that there is a weak recirculation bubble in the riblet groove, which is especially clear in the Stokes case (first panel in the figure), but which persists up to the viscous breakdown, becoming increasingly asymmetric for the larger riblets.

At the same time, other changes occur in the outer flow. The increasing curvature of the conditional streamlines suggests that a mean vortex settles above the groove, and drifts towards the wall as the riblet size increases. It turns out that the drift is mostly due to the change in the scale of the figures, which are normalized with the riblet height.

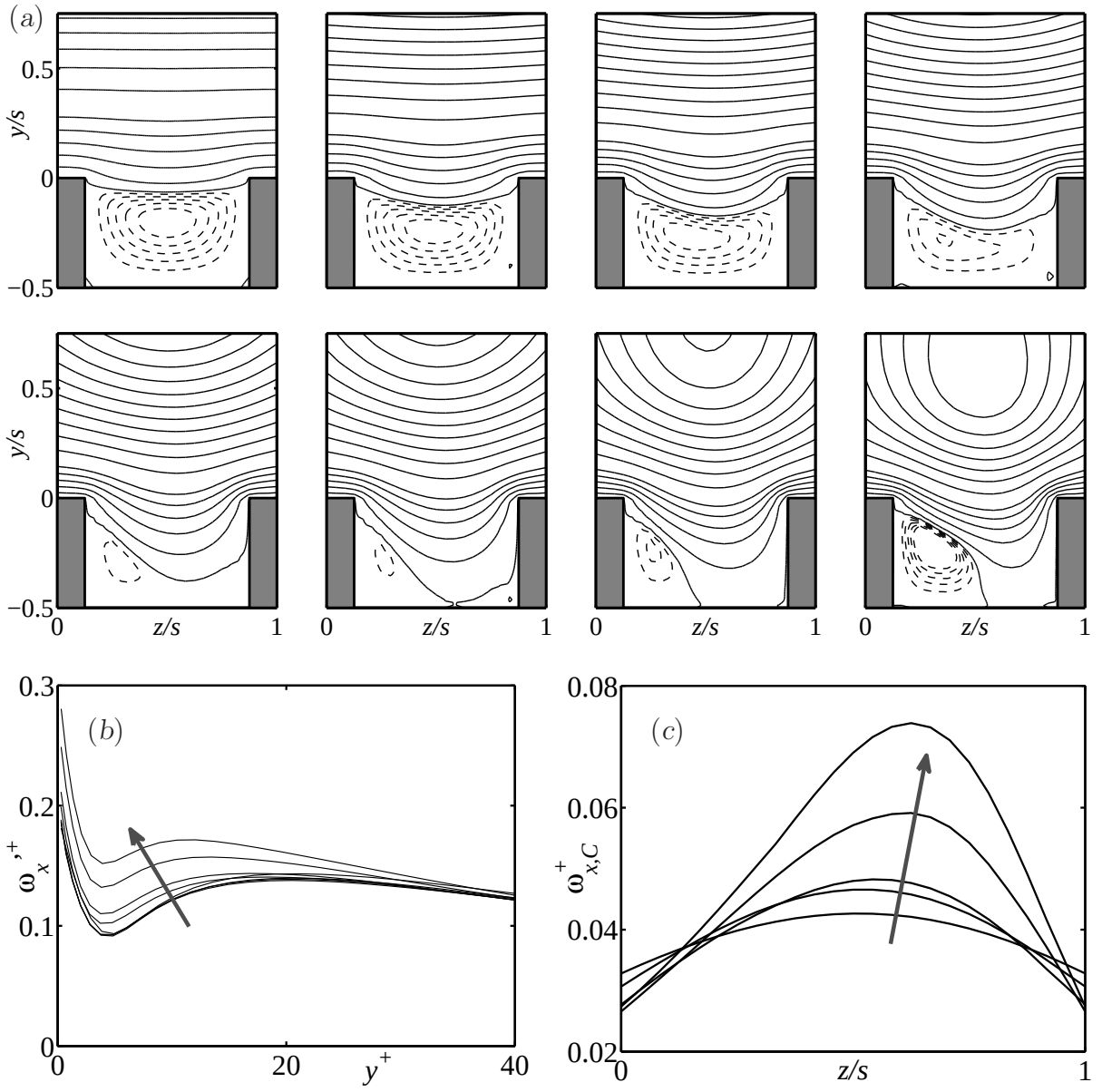

Figure 5.2: (*a*) Streamfunction of the conditionally averaged crossflow above and within the riblet grooves, conditioned to a mean rightwards flow in the plane immediately above the riblet tips. From left to right and top to bottom, $\ell_g^+ = 0$ and cases 5S to 20S. The case $\ell_g^+ = 0$ is a two-dimensional Stokes simulation. To facilitate the comparison between different cases, the streamfunction has been scaled with u_τ and with the riblet height h. ——, rightwards flow with streamfunction values $0.05 \times [0(0.2)1]^2$ and $0.10(0.05)0.60$. - - - -, clockwise recirculation flow, with streamfunction values $-2 \times [0.2(0.2)1] \times 10^{-3}$. (*b*) Fluctuation of the streamwise vorticity as a function of the distance to the riblet peak plane, for cases 0S to 20S. (*c*) Maximum conditioned streamwise vorticity, as a function of the z-position across the riblet span, for cases 10S to 20S. The arrows in (*b*) and (*c*) indicate increasing ℓ_g^+.

The vertical position of the vortices is better measured by the unconditioned root-mean-squared intensity of the streamwise vorticity ω_x, which is shown in figure 5.2(b). The quasi-streamwise vortices correspond to the maximum away from the wall, and slowly approach the wall as the riblets get larger, but they never get closer than $y^+ \approx 10 - 15$. The simplest interpretation of the velocity fields in figure 5.2(a) is that the vortices tend to linger on top of the grooves. To measure this tendency, we can obtain mean vorticity fields conditioned to the direction of the crossflow, $\langle\omega_x\rangle_c$, following the procedure described above, and determine the modulation in z of the maximum for each y, $\max_y\langle\omega_x\rangle_c$. This quantity is shown in figure 5.2(c). It is maximum above the grooves and minimum above the riblet tips, but the modulation is negligible for the smallest riblets, increasing with the riblet size. This shows that the vortices get increasingly localized above the grooves for the larger riblets.

Choi (1989), Goldstein *et al.* (1995) and Goldstein & Tuan (1998) suggested that one of the effects of the riblets was to order the turbulent flow near the wall by preventing the spanwise motion of the streamwise vortices, inhibiting the instability of the streamwise-velocity streaks, and eventually the bursting. They conjectured that this effect would be part of the drag-reduction mechanism. The vortex localization observed in figure 5.2(c) supports the flow-ordering idea, but it is interesting that the localization is weak for the riblets that actually reduce drag, and strongest for those that increase it, suggesting that other phenomena may be more important for the drag evolution.

The actual lodging of the vortices inside the grooves, which was documented by Choi *et al.* (1993) and Lee & Lee (2001) for grooves with $\ell_g^+ \gtrsim 25$, and proposed as a mechanism for the drag deterioration, is not observed in the present simulations. Figures 5.1 and 5.2(a) suggest that, if it happens at all, it probably only does for very large riblets in the drag-increasing regime, rather than for those in the neighborhood of the performance optimum. In that sense, it should probably be considered a consequence, rather than the cause, of the penetration of the outer flow into very large grooves.

On the other hand, although it could have been expected that the recirculation bubbles would isolate the valley floor from the overlying flow, keeping the high-momentum fluid away from the groove walls, it is somewhat surprising that all the changes in the crossflow have a relatively small effect on the streamwise velocity, which is the component responsible for the friction. That is seen in figure 5.3, which portrays the mean slip velocity U_0 at $y = 0$, as a function of the riblet size, and shows that the linear Stokes approximation holds for the longitudinal flow throughout the whole range of our simulations, at least in the mean. Averaging the Stokes assumption (1.2) over the streamwise direction and time

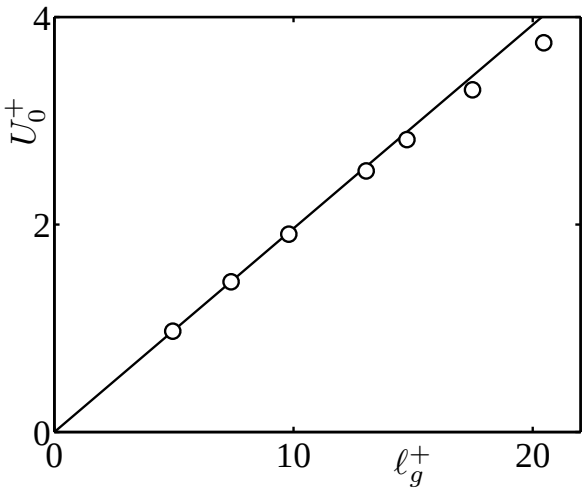

Figure 5.3: Mean slip velocity at the riblet-tip plane, compared with the Stokes result (5.3), represented by the solid line.

implies that the mean velocity of the boundary layer approaches the wall with an effective slip velocity

$$U_0^+ \equiv U^+(y=0) = -\Delta_u^+, \tag{5.3}$$

which is represented by the solid line in figure 5.3.

The reason for the small effect of the crossflow on U_0 is probably that the recirculation bubbles in figure 5.2(a) are relatively weak. The magnitude of the conditioned spanwise velocity at the horizontal mid-plane of the riblet grooves in figure 5.2(a), $y = -h/2$, never exceeds $0.04\,u_\tau$, and the mean streamwise velocity within the grooves follows the same universal curve $U(y/h)/U_0$ within a few percent for all the riblets in our simulations. Similarly, the mean velocity gradient at the bottom of the groove is always $(\partial_y U)^+ \approx 0.15$.

That low shear at the bottom of the grooves is not enough to guarantee drag reduction, as seen in the case $\ell_g^+ = 0$, where the drag reduction is zero because the low shear within the groove is compensated by the higher one at the peaks. In fact, the approximately universal scaling of the streamwise velocity inside the grooves suggests that the reason of the drag reduction is not so much that the friction decreases, but that the slip augments the velocity of the free stream, thus decreasing the friction coefficient $2\tau_w/U_\delta^2$. Of course, both interpretations are essentially the same, depending on the units used to express the result, and the question will be examined quantitatively in §5.2.

Before doing that, we can gain some insight on how the riblets affect the distribution of the friction by examining the conditional statistics of the viscous, Reynolds, and total streamwise stresses on the x–z plane just above the riblet tips. Figures 5.4(a)–5.4(c)

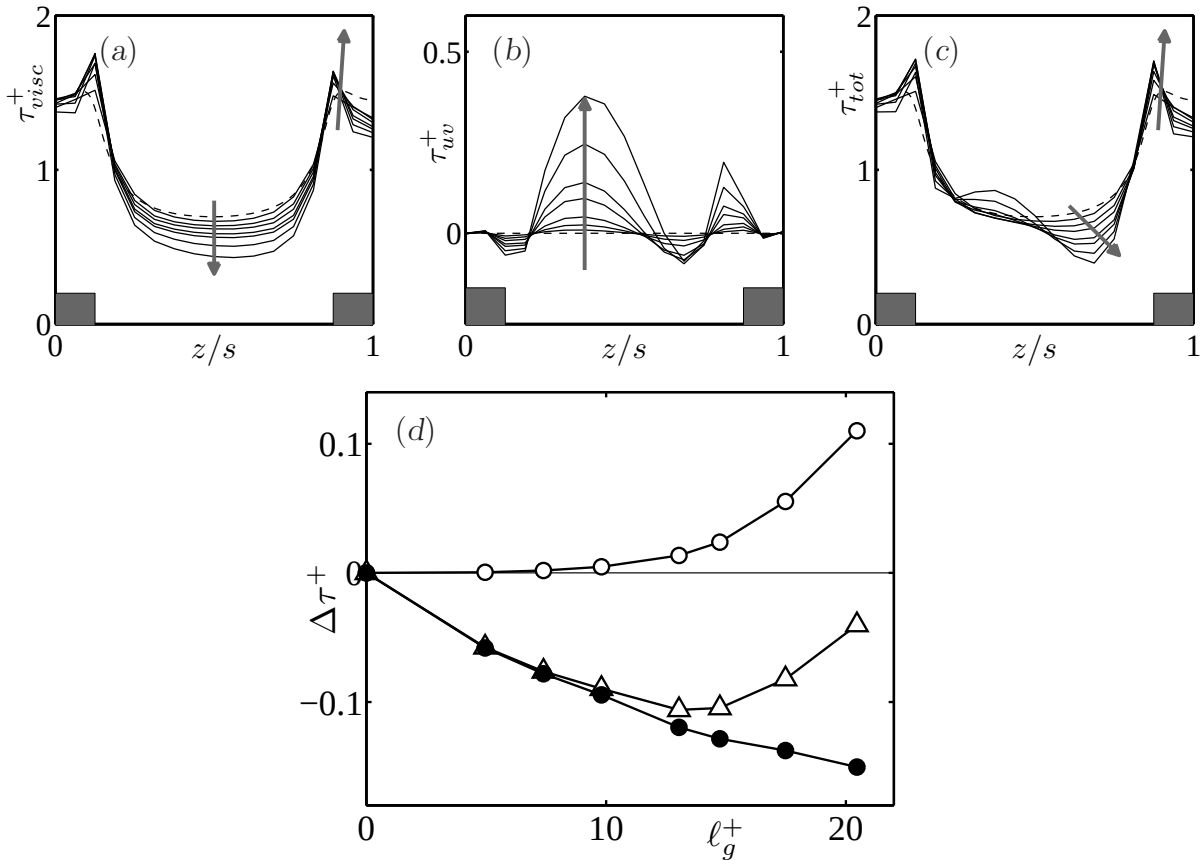

Figure 5.4: Conditionally averaged (a) viscous, (b) Reynolds and (c) total shear stresses at the $x-z$ plane just above the riblet tips, as a function of the spanwise position with respect to the riblets. The arrows indicate increasing ℓ_g^+. The dashed line corresponds to the Stokes two-dimensional simulations for $\ell_g^+ = 0$. The rectangles at the bottom of the figures mark the z-location of the riblet tips. Each flow is normalized in its own wall units. (d) Integrated average stresses at the same x–z plane, as a function of ℓ_g^+; —●—, viscous stress; -○-, Reynolds stress; -△-, total stress. The difference between the total stress portrayed here and the results in figure 5.1 is due to the pressure drop within the grooves, which is not accounted for here, and whose contribution increases with groove size.

portray the conditionally-averaged stresses normalized with the friction velocity of each ribbed surface. The figures show that the dominant stress on that plane is always the viscous one, $\tau_{visc} = \nu\partial_y\langle u\rangle_c$, which partially compensates its high value over the tips with a lower one above the grooves. We have already mentioned that the net effect vanishes in the case $\ell_g = 0$, and figures 5.4(a)–5.4(c) show that, although the viscous contribution decreases over the groove as the riblet size increases, the effect is partly compensated by the Reynolds stress, $\tau_{uv} = -\langle uv\rangle_c$, which becomes significant for the larger riblets.

The ratio between the contributions to the total skin friction of the tips and of the grooves remains relatively unchanged over the range of our simulations, in agreement with the previous observation that the streamwise flow in the groove remains dominated by viscosity. The partial transfer of viscous to Reynolds stress reflects the modification of the distribution of streamwise and wall-normal velocities near the plane of the riblet tips, but it does not reach deep into the grooves.

This does not mean that the drag remains constant, since our simulations cover the whole range from drag reduction to drag increase. The net contributions of the two stress components, now expressed in terms of the constant friction velocity of the smooth channel, can most clearly be appreciated in figure 5.4(d). The figure shows that the net viscous stress decreases almost linearly with ℓ_g^+, while the Reynolds stress increases slowly at first and faster for the larger ℓ_g^+. In the cases near the maximum drag reduction, the Reynolds stress compensates the decrease of the viscous one and the drag reduction saturates. For riblets larger than the optimum the drag reduction begins to degrade, because the mean Reynolds stress increases further. For case 20S, the contribution of the Reynolds stress is so large that the drag reduction becomes a k-roughness-like drag increase. The breakdown is therefore associated with the appearance of inertial effects, but the discussion in the previous paragraph suggests that they are concentrated near or above the plane of the tips, rather than within the grooves. They are discussed in the next section.

5.2 Spectral analysis

The main difference between flows in smooth and ribbed channels is the higher fluctuation intensities of the latter immediately above $y = 0$ (not shown, but see figures 5.5 to 5.9). In the same way, the transverse Reynolds stress $-\langle uv \rangle$ increases over riblets, especially over the larger ones (see figure 5.4(b)). Both things are to be expected from the relaxation of the wall boundary conditions above the riblet grooves, and are consistent with the discussion in the previous section. To account for these increases, Choi *et al.* (1993) introduced a virtual origin for the turbulent statistics slightly below the riblet-peak plane.

More interesting is than those higher intensities is their spectral distribution. Figures 5.5 to 5.10 contain examples of two-dimensional spectral energy densities over wall-parallel planes for cases 0S to 20S, representing how the energy of the different velocity components is distributed in the λ_x^+–λ_z^+ wavelength plane. Cases 13S to 20S, which are those with ℓ_g^+

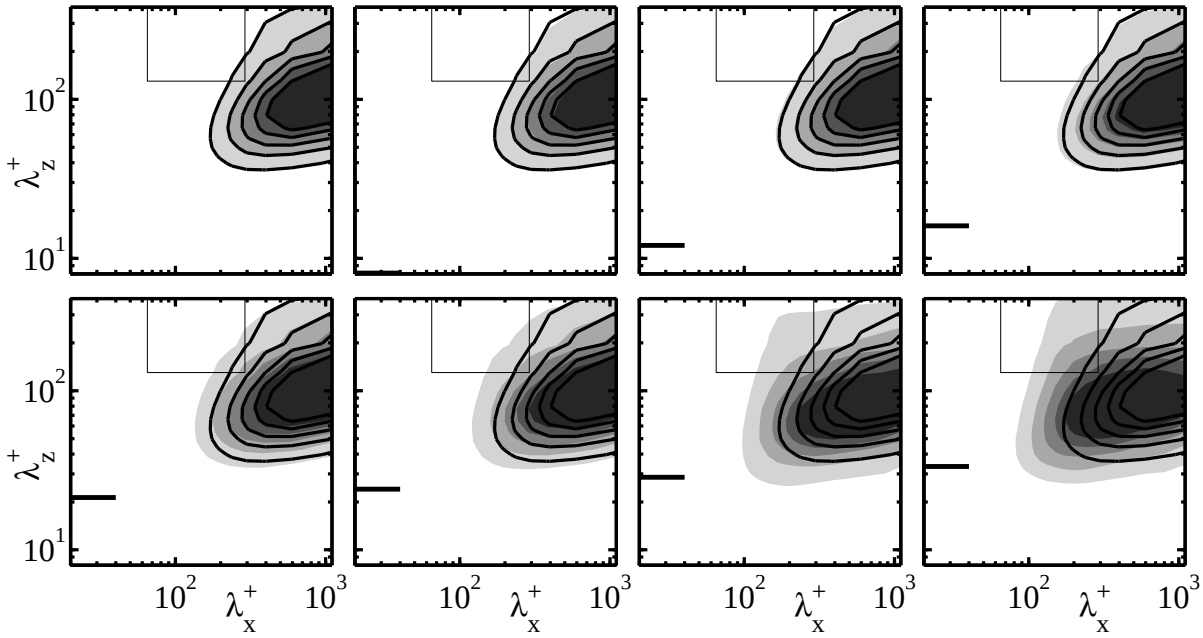

Figure 5.5: Spectral energy density of the streamwise velocity, $k_x k_z E_{uu}$, at $y^+ \approx 5$. From left to right and top to bottom, cases 0S, 5S, 7S, 10S, 13S, 15S, 17S, and 20S. The contour increments are $0.09\,u_\tau^2$. For comparison, the contours from case 0S are superimposed as solid lines in all panels. The thick horizontal line to the left of the plots marks the riblet spacing. The rectangular area indicates the region of the spectrum considered in figure 5.13.

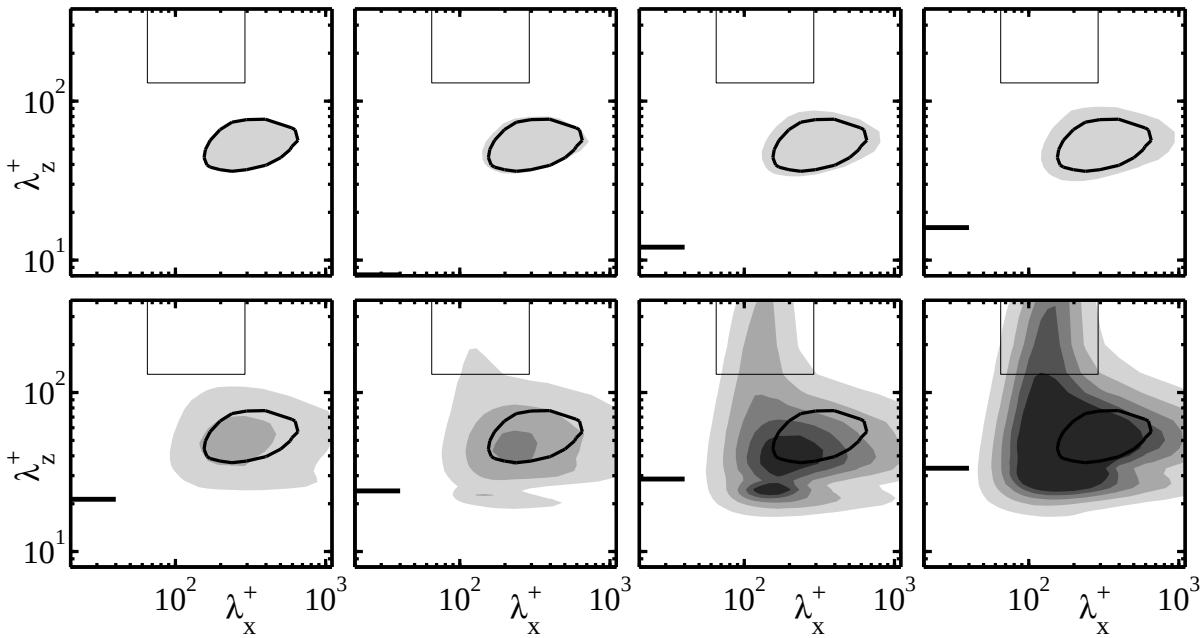

Figure 5.6: Spectral energy density of the wall-normal velocity, $k_x k_z E_{vv}$, at $y^+ \approx 5$. From left to right and top to bottom, cases 0S, 5S, 7S, 10S, 13S, 15S, 17S, and 20S. The contour increments are $0.003\,u_\tau^2$. Solid lines are as in figure 5.5.

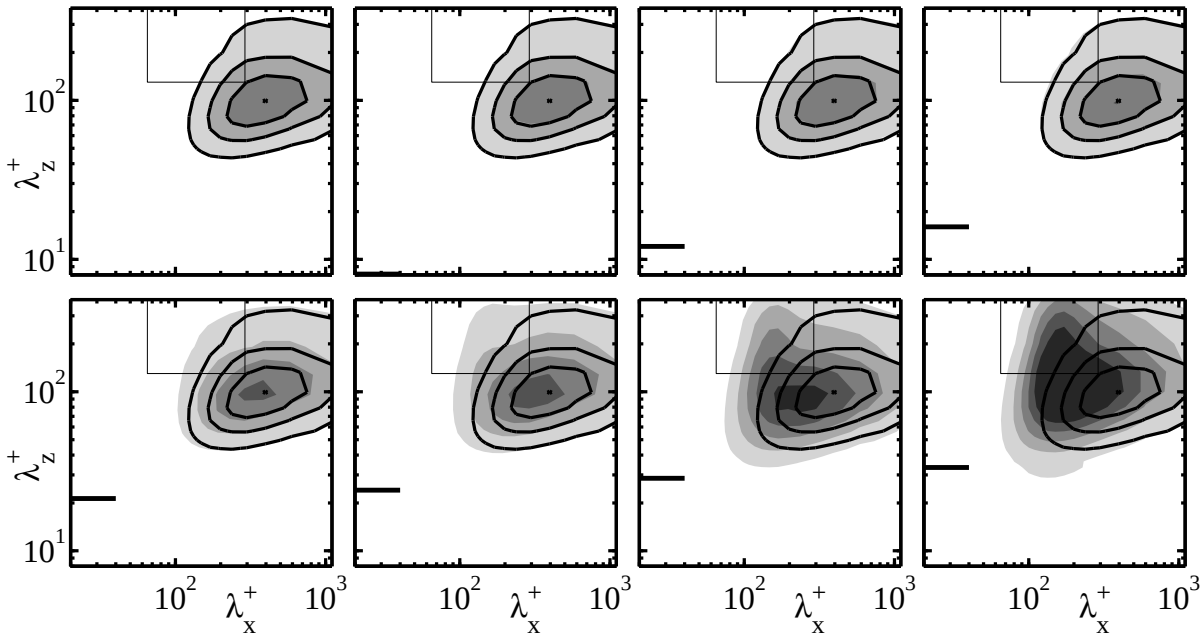

Figure 5.7: Spectral energy density of the spanwise velocity, $k_x k_z E_{ww}$, at $y^+ \approx 5$. From left to right and top to bottom, cases 0S, 5S, 7S, 10S, 13S, 15S, 17S, and 20S. The contour increments are $0.026\,u_\tau^2$. Solid lines are as in figure 5.5.

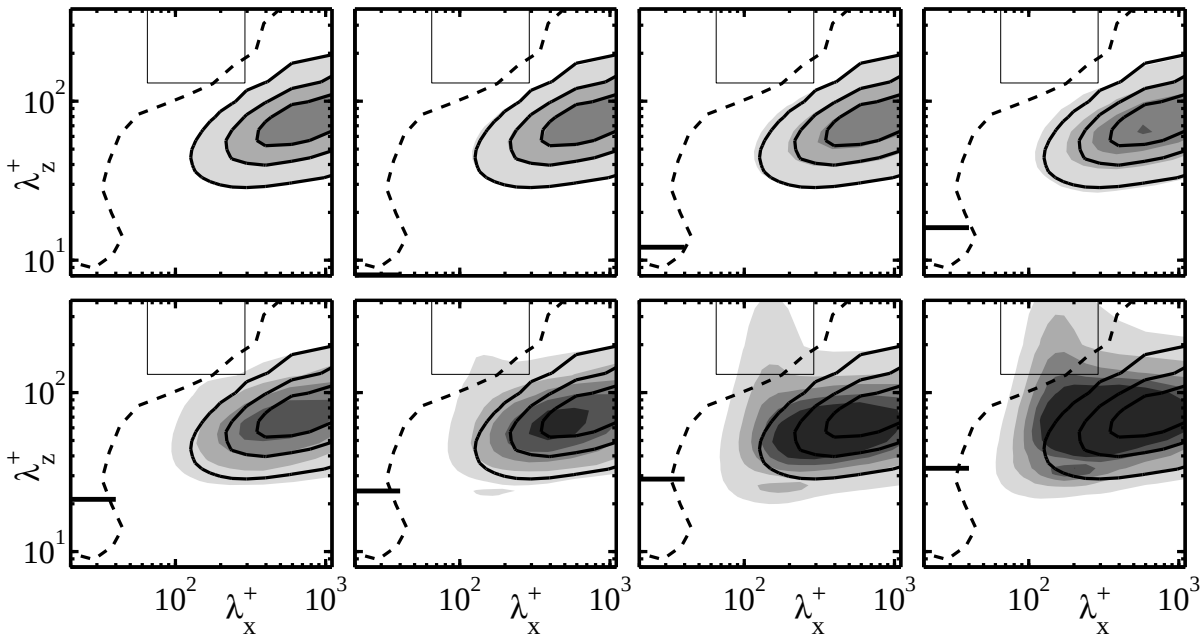

Figure 5.8: Spectral density of the Reynolds stress, $-k_x k_z E_{uv}$, at $y^+ \approx 5$. From left to right and top to bottom, cases 0S, 5S, 7S, 10S, 13S, 15S, 17S, and 20S. The contour increments are $0.008\,u_\tau^2$, starting at $0.004\,u_\tau^2$. Solid lines are as in figure 5.5, and the dashed line represents the $E_{uv} = 0$ contour for case 0S.

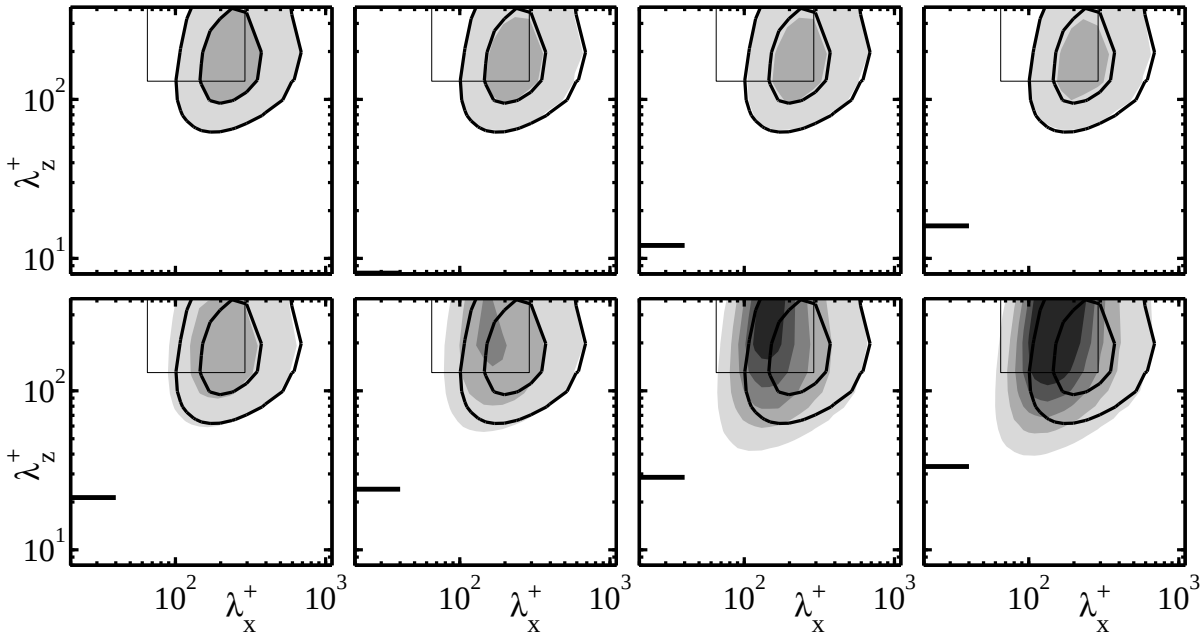

Figure 5.9: Spectral density of the pressure fluctuations, $k_x k_z E_{pp}$, at $y^+ \approx 5$. From left to right and top to bottom, cases 0S, 5S, 7S, 10S, 13S, 15S, 17S, and 20S. The contour increments are $0.2\,u_\tau^4$. Solid lines are as in figure 5.5.

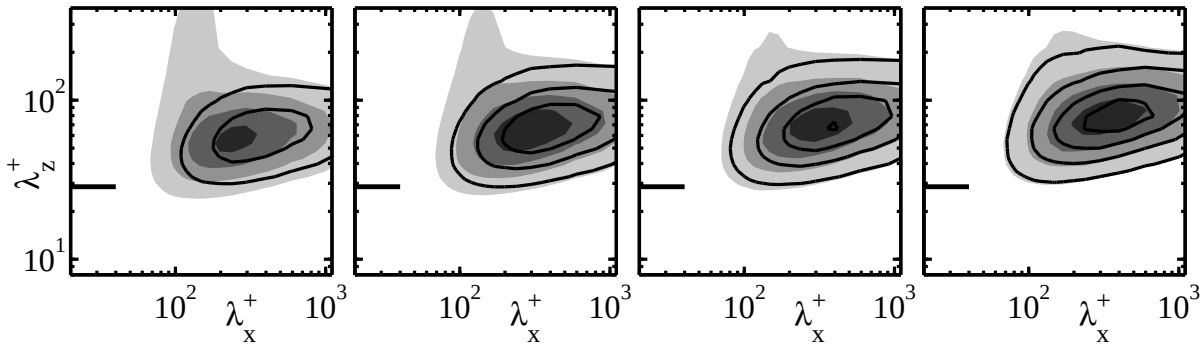

Figure 5.10: Premultiplied two-dimensional spectrum of v^2 for case 17S. From left to right, at heights $y^+ \approx 10$, 15, 19, and 25. The same spectrum is plotted for $y^+ \approx 5$ in figure 5.6. The superimposed solid contour lines correspond to the smooth-wall case. The contour increments are 0.010, 0.015, 0.020, and $0.025\,u_\tau^2$ for increasing y^+. The thick horizontal line to the left of the plots marks the riblet spacing.

beyond the viscous breakdown, are the ones whose spectra differ most from those of the smooth channel, which are superimposed for comparison as solid lines.

For instance, figure 5.6 shows the spectral density of v^2 at $y^+ \approx 5$. As the riblet size increases beyond the optimum spacing, energy accumulates in a spectral region near $\lambda_x^+ \approx 150$ that extends over all the spanwise wavelengths longer than $\lambda_z^+ \approx 50$, and which therefore represents very wide structures. The same can be seen in the spectra of the

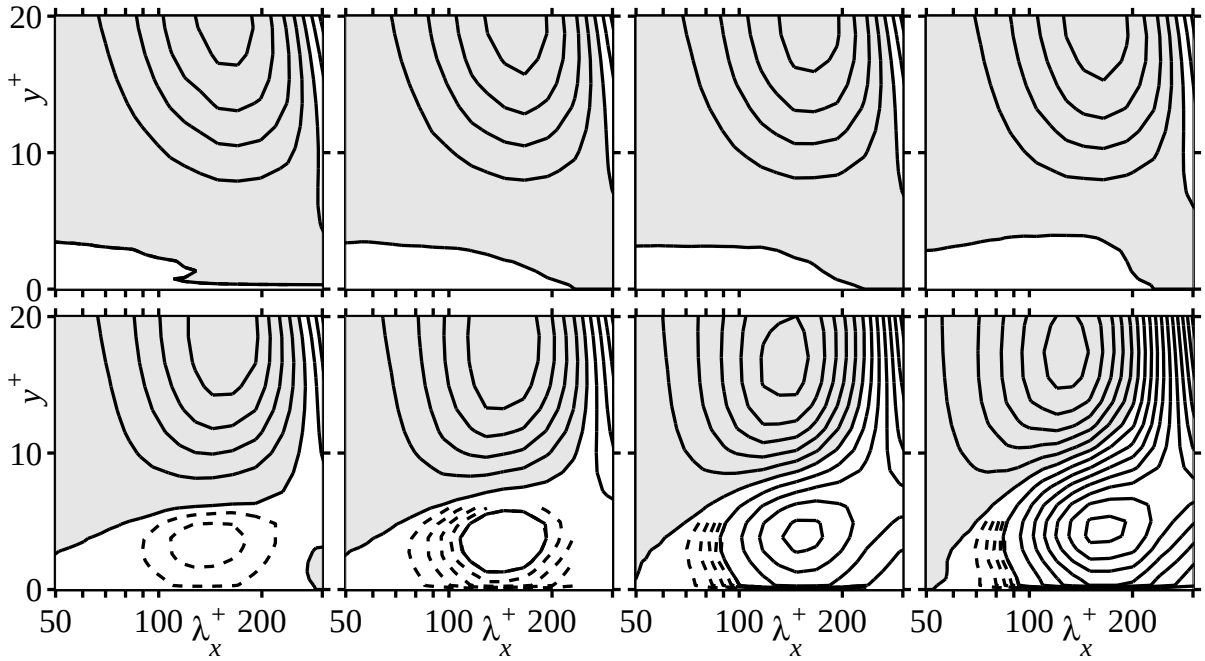

Figure 5.11: Premultiplied streamwise cospectra of the Reynolds stress, $k_x E^+_{uv}$. From left to right and top to bottom, cases 0S, 5S, 7S, 10S, 13S, 15S, 17S, and 20S. The spectra have been integrated in z only for $\lambda_z^+ \geq 130$. The solid isolines are spaced by 4×10^{-3}, with the shaded area corresponding to positive values. The dashed isolines correspond to $4 \times [0.2(0.2)0.8] \times 10^{-3}$. Notice that the stresses in the region portrayed are counter-gradient for the smooth-wall case, as can be observed in figure 5.8.

other flow variables, given in figures 5.5 to 5.9. The new spectral region exists only for heights below $y^+ \approx 15 - 20$, depending on the variable considered. The widest vertical ranges correspond to v^2, whose spectrum for case 17S is portrayed at different heights in figure 5.10, and to the pressure fluctuations (not shown, but see figure 6.7(c)).

We next focus our analysis on those new structures, which we will treat as being approximately confined to a spectral window delimited by $65 < \lambda_x^+ < 290$ and $\lambda_z^+ > 130$. That window is included in figure 5.6 for reference. Note that the relatively high lower limit for λ_z^+ implies that we will essentially be studying the effect of riblets on the spanwise-averaged flow, as opposed to the conventional approach used in §5.1, which stresses streamwise averages.

Figure 5.11 portrays the streamwise one-dimensional cospectral density of the uv stress, integrated for $\lambda_z^+ > 130$, and shows that the shear stress carried by the new structures concentrates around $\lambda_x^+ \approx 150$ and $y^+ \approx 4$, and that their contribution increases with the riblet size. The Reynolds stress of the smooth channel is weak and positive

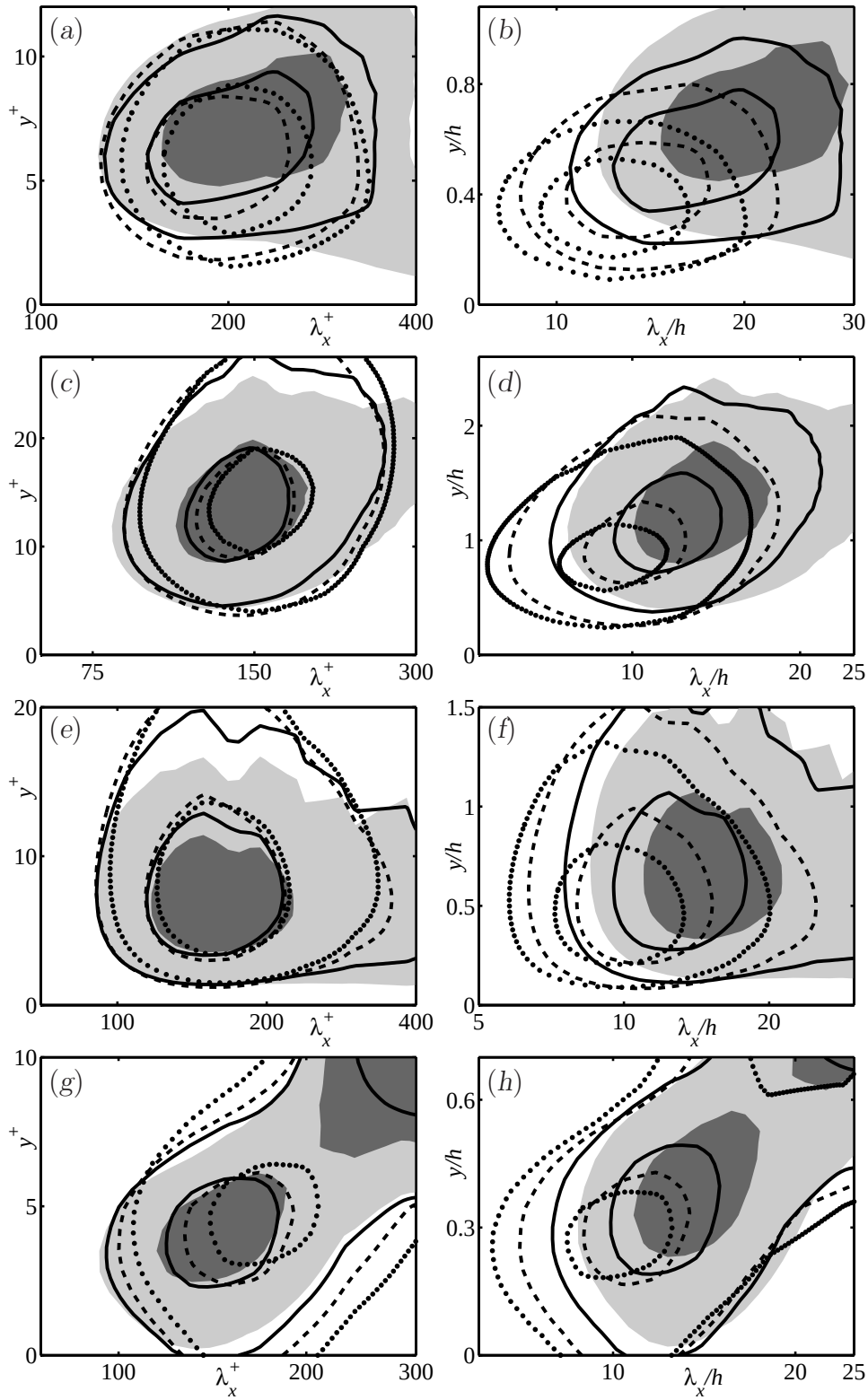

Figure 5.12: Increment in the spectra of the flow variables caused by the presence of riblets, integrated for $\lambda_z^+ > 130$. (*a*–*b*), $\Delta(k_x E_{u^2})$; (*c*–*d*), $\Delta(k_x E_{v^2})$. (*e*–*f*), $\Delta(k_x E_{w^2})$; (*g*–*h*), $\Delta(-k_x E_{uv})$. Figures are scaled in wall units in the first column, and with the riblet height h in the second. Shaded, case 13S; ——, 15S; – – – –, 17S; ·····, 20S. The isolines drawn have been chosen to enhance the comparison of the scales in the four cases considered, regardless of their magnitude.

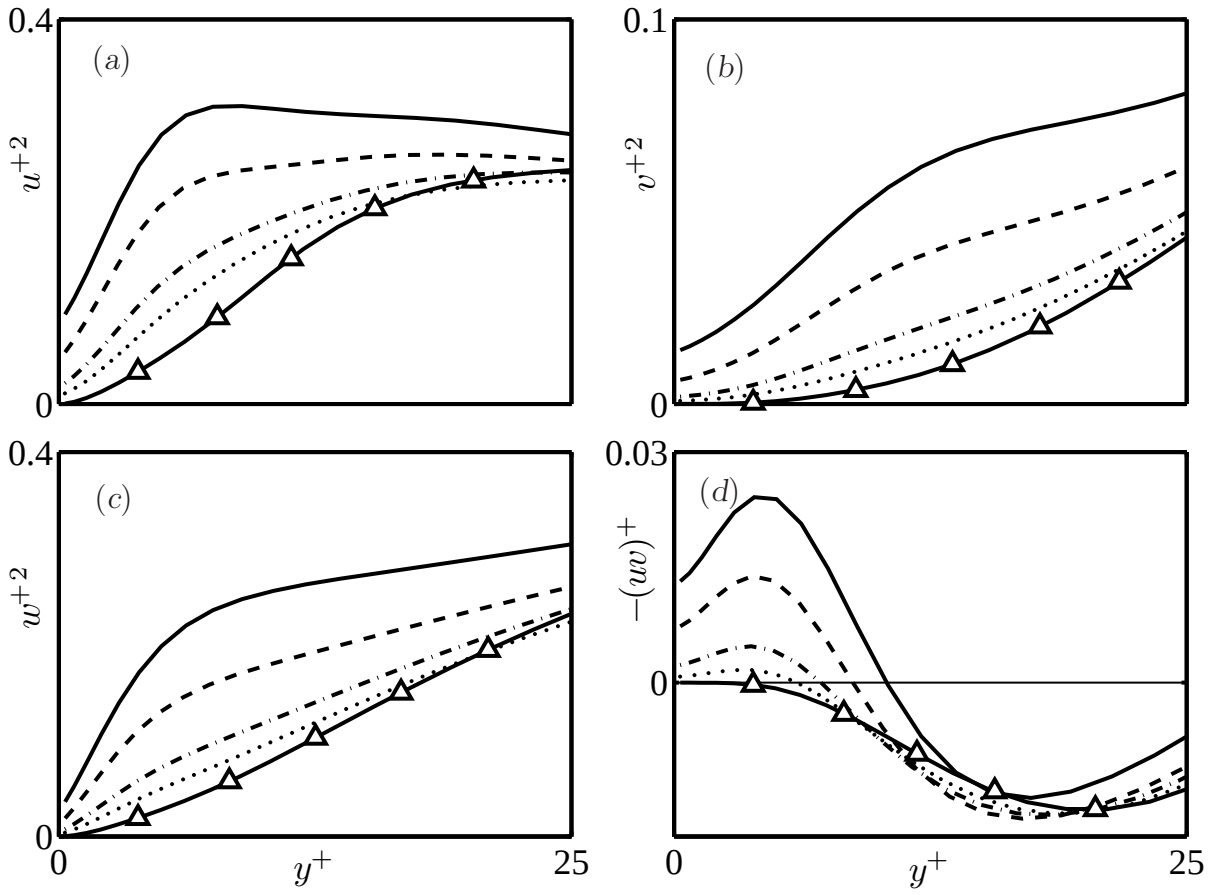

Figure 5.13: Energy contained in the long spanwise structures above riblets. The figures portray the integrals of the spectra of (*a*) u^{+2}, (*b*) v^{+2}, (*c*) w^{+2}, and (*d*) $-uv^+$, in the region $65 \leq \lambda_x^+ \leq 290$, $\lambda_z^+ \geq 130$. -△-, smooth wall; ·····, 13S; – · – , 15S; – – – –, 17S; ——, 20S.

(counter-gradient) in that spectral region, but becomes negative and stronger for riblets larger than the optimum.

The spectra of the additional energy of the three velocity components carried by the new structures also scale well in wall units, and better than when normalized with the riblet size. Figure 5.12 portrays, for the cases with ℓ_g^+ larger than the optimum, the departures from the smooth case of the spectra integrated for $\lambda_z^+ > 130$. The figure shows that the position of the structures collapses well when expressed in wall units, but not so much when λ_x and y are scaled with the riblet size. There is a slight drift of the structures towards longer λ_x^+ for increasing riblet size, which is perhaps more apparent for v^2 and uv. The spanwise structures center around $\lambda_x^+ \approx 150$ and $y^+ \approx 5$ in most cases, although for the streamwise velocity they are slightly longer, $\lambda_x^+ \approx 200$, and v^2 peaks around $y^+ \approx 10$. Since the present simulations have approximately the same Reynolds

number, it is impossible to determine from them whether the spectra collapse in wall or in outer units, although the former seems more plausible given the location of the structures very near the wall, as well as the experimental scaling of the viscous breakdown in wall units. The simulations at higher Reynolds number of chapter 6 were devised largely to shed light on this dilemma, and further support for the wall scaling is provided in chapter 7, where a simplified linearized model for the structures is proposed.

The energy integrated over the spectral window defined above is given in figure 5.13 for the three velocity components and for the shear stress. For riblets smaller than 10S, which are not shown in the figure, the results are virtually indistinguishable from the smooth case, but the fluctuations become stronger beyond the optimum riblet size, and keep increasing thereafter.

5.2.1 Breakup of the different contributions to the change in friction drag

The additional uv stresses can be directly related to the drag increase beyond the breakdown. Using the subscript 'S' to refer to the reference smooth channel, the momentum balances for the smooth and ribbed channel are, respectively,

$$\tau_{uvS} + \nu \frac{\partial U_S}{\partial y} = u_{\tau S}^2 \frac{\delta - y}{\delta}, \tag{5.4}$$

$$\tau_{uv} + \nu \frac{\partial U}{\partial y} = u_\tau^2 \frac{\delta - y}{\delta'}. \tag{5.5}$$

If we define $u_* = u_\tau(\delta/\delta')^{1/2}$ and integrate these equations over $y \in (0, \delta)$, they can be combined into

$$\int_0^\delta \tau_{uv}^* \, \mathrm{d}y + \frac{\nu}{u_*^2}(U_\delta - U_0) = \int_0^\delta \tau_{uvS}^+ \, \mathrm{d}y + \frac{\nu}{u_{\tau S}^2} U_{\delta S}, \tag{5.6}$$

where $\tau_{uv}^* = \tau_{uv}/{u_*}^2$. Further manipulation results in

$$\frac{\Delta c_f}{c_{f0}} \approx -\frac{\Delta U_\delta^{+2}}{U_\delta^{+2}} = T_1 + T_2 + T_3, \tag{5.7}$$

where

$$T_1 = \left[1 - \frac{\delta U_\delta}{\delta' U_{\delta S}}\right] \left(\frac{U_{\delta S}^+}{U_\delta^+}\right)^2, \tag{5.8}$$

$$T_2 = -\frac{U_0^+}{U_\delta^+}, \tag{5.9}$$

$$T_3 = \frac{\delta \delta^+}{\delta' U_\delta^+} \int_0^1 \left(\tau_{uv}^* - \tau_{uvS}^+\right) \, \mathrm{d}(y/\delta). \tag{5.10}$$

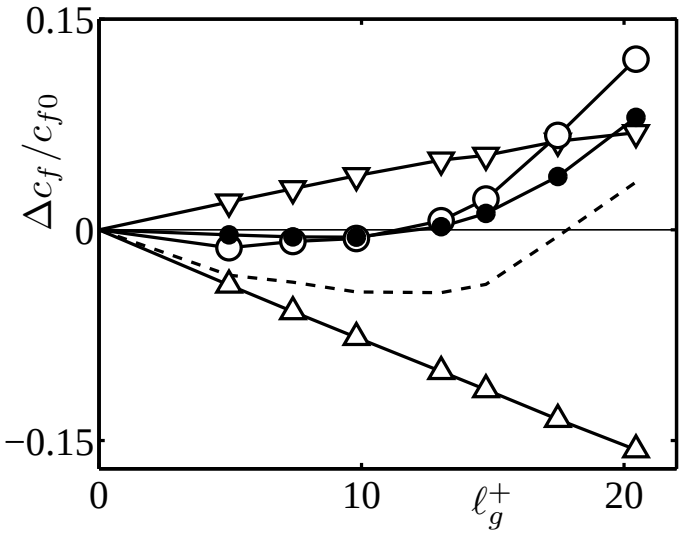

Figure 5.14: Contributions T_1, T_2 and T_3 to the drag reduction curve, as defined by equations (5.8)–(5.10). -▽-, T_1; -△-, T_2; -○-, T_3 calculated from the full uv stress; —●—, T_3 calculated considering uv only within $65 \leq \lambda_x^+ \leq 290$, $\lambda_z^+ \geq 50$, and $y^+ \lesssim 35$. ----, total drag reduction $T_1 + T_2 + T_3$.

These three terms are shown in figure 5.14. The first one is a correction factor that accounts for the differences in the definition of the two channels, both in height and in mass flux. It should remain small for the decomposition (5.7) to be useful, since otherwise the influence of the Reynolds number mentioned in §2.2 should be taken into account. Figure 5.14 shows that T_1 is always less than a few percent in our simulations.

The term T_2 represents the slip velocity at the riblet tips, which we have already discussed in §5.1. It is directly related to the drag-reduction mechanism of the protrusion height, and remains proportional to the riblet size over our simulation range. It always reduces the skin friction.

The term T_3 represents the effect of the extra Reynolds stresses in the flow above the riblet tips and, owing to the scaling with u_*, its integrand differs from zero only near the wall. Figure 5.14 confirms that T_3 is the term responsible for the drag degradation. The figure also includes the part of the extra Reynolds stress that is contained in the spectral region that we have associated with the new spanwise structures. It shows that this region contains most of the extra stress, strongly suggesting that the new structures are the root cause of the degradation of the drag.

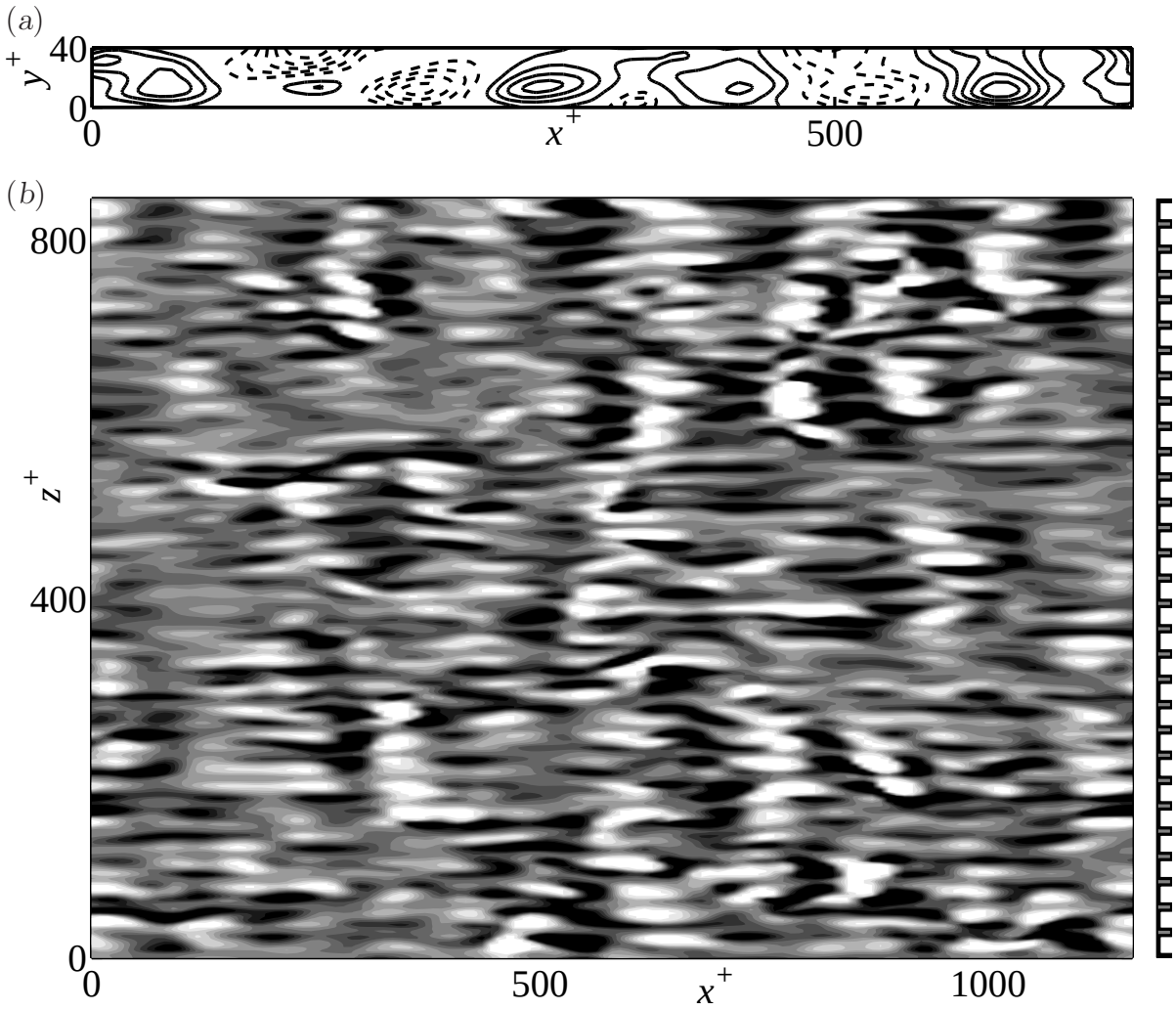

Figure 5.15: (*a*) Instantaneous streamlines of the spanwise-averaged perturbation u–v flow, for case 17D. The solid lines correspond to clockwise-rotating rollers. (*b*) For the same instant, wall normal velocity at $y^+ \approx 3$. The clear regions represent negative velocities, or flow towards the wall, and the dark regions positive ones. The position of riblet tips and grooves is sketched to the right of the figure.

5.2.2 Instantaneous realization of the spanwise structures

The spanwise length of the new structures, $\lambda_z^+ \gtrsim 50$, implies that they extend over several inter-riblet spacings. In fact, because they are much wider than their streamwise wavelengths, they can be characterized as spanwise rollers, which are shown in figure 5.15 for an instantaneous realization of case 17D. Figure 5.15(*a*) portrays streamlines of the flow averaged over the full span of the simulation box, which is in this case $L_z^+ \approx 850$. The averaged rollers are centered at $y^+ \approx 10 - 15$, and extend to the wall, even penetrating the riblet grooves. Their streamwise extent is about 50–70 wall units, and the separation

between rollers of the same sign is $\lambda_x^+ \approx 150$, consistent with the spectral analysis. That implies aspect ratios for the spanwise-averaged structures in figure 5.15(a) of the order of 10–20, and characterizes them as quasi-two-dimensional in the x–y plane. The structures themselves can be seen in the wall-parallel section in figure 5.15(b), which confirms their spanwise coherence across several riblet grooves. That coherence manifests itself in spite of the presence of the riblet blades, which disrupts the structures with riblet-spacing periodicity. It must however be stressed that figure 5.15 is merely an instantaneous realization of the flow, and is only included here to help the reader visualize the roller structures. The evidence for those rollers is not in this figure, but in the discussion on spectra of §5.2, and in the corresponding figures 5.6 to 5.13.

To our knowledge, those structures had not been reported before over riblets, but they can probably be found, in retrospect, in some of the visualizations published by previous authors. See, for example, the visualization of v at $y^+ = 8$ above the tips of triangular riblets in figure 20(b) of Goldstein *et al.* (1995), or the spanwise lines of velocity reversal within the grooves of similar riblets in figure 30 of Chu & Karniadakis (1993). Even if their conditions are very different from ours, it is interesting that the streamwise wavelengths of the observed structures are in both cases in the range $\lambda_x^+ = 100 - 200$. It should be noted, however, that we do not observe flow reversal within our grooves.

Although the formation of these structures, perpendicular rather than parallel to the riblets, may seem surprising, it is not completely unexpected. Similar spanwise rollers have been reported over vegetable canopies (Raupach *et al.*, 1996; Finnigan, 2000), and over permeable (Jiménez *et al.*, 2001) and porous walls (Breugem *et al.*, 2006). They are typically attributed to Kelvin–Helmholtz-like instabilities due to the relaxation of the impermeability condition at the wall, although quantitative analyses to support that claim are somewhat scarce in the literature (Jiménez *et al.*, 2001; Py *et al.*, 2006). Ghisalberti (2009) has proposed that these Kelvin–Helmholtz structures are a dominant feature common to "obstructed" shear flows.

5.2.3 Convection velocities

The hypothesis of an instability is reinforced by the spectral distribution of the advection velocities of the u, v and w-structures, respectively C_u, C_v and C_w. They can be computed as a function of y and of the two wall-parallel wavelengths, using the scheme in del Álamo & Jiménez (2009), which for C_u is

$$C_u\left(k_x, k_z, y\right) = \frac{\mathbb{I}\mathrm{m}\left\langle \widehat{u}^* \partial\widehat{u}/\partial t \right\rangle}{k_x \left\langle \left|\widehat{u}\right|^2 \right\rangle}. \tag{5.11}$$

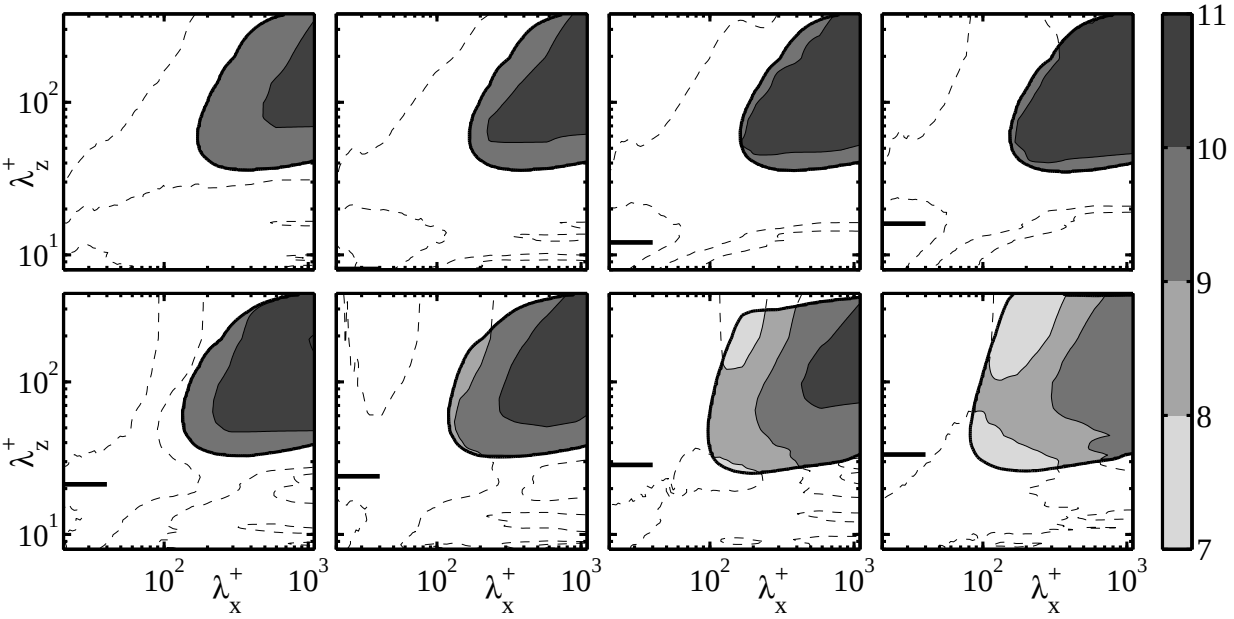

Figure 5.16: Spectral distribution of the convection velocity C_u^+ of u-structures at $y^+ \approx 5$ for cases 0S to 20S. Values are only significant within the shaded region, and are portrayed elsewhere by dashed contours. The encircling solid line represents the threshold $k_x k_z E_{uu} = 0.09\, u_\tau^2$. Outside of it the u-structures carry very little energy, but lead to large uncertainty errors in the calculation of convection velocity. The thick horizontal line to the left of the plots marks the riblet spacing.

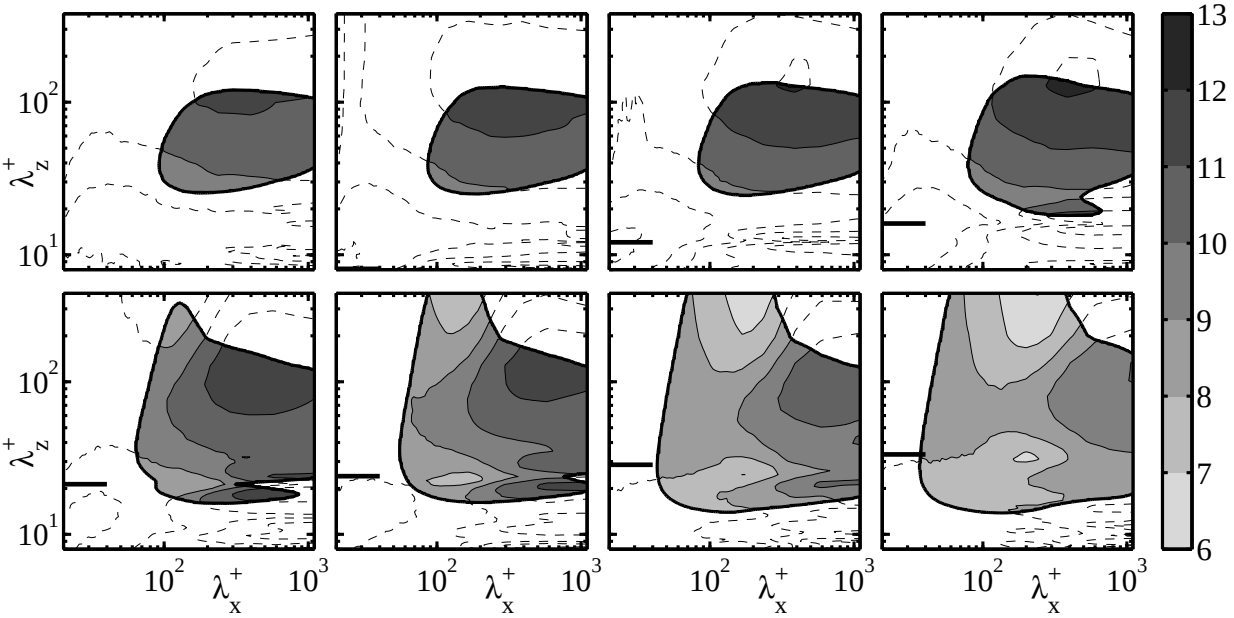

Figure 5.17: Spectral distribution of the convection velocity C_v^+ of v-structures at $y^+ \approx 5$ for cases 0S to 20S. The lines and contours are the same as in figure 5.16, with the solid line encircling the shaded region representing the threshold $k_x k_z E_{vv} = 0.0012\, u_\tau^2$.

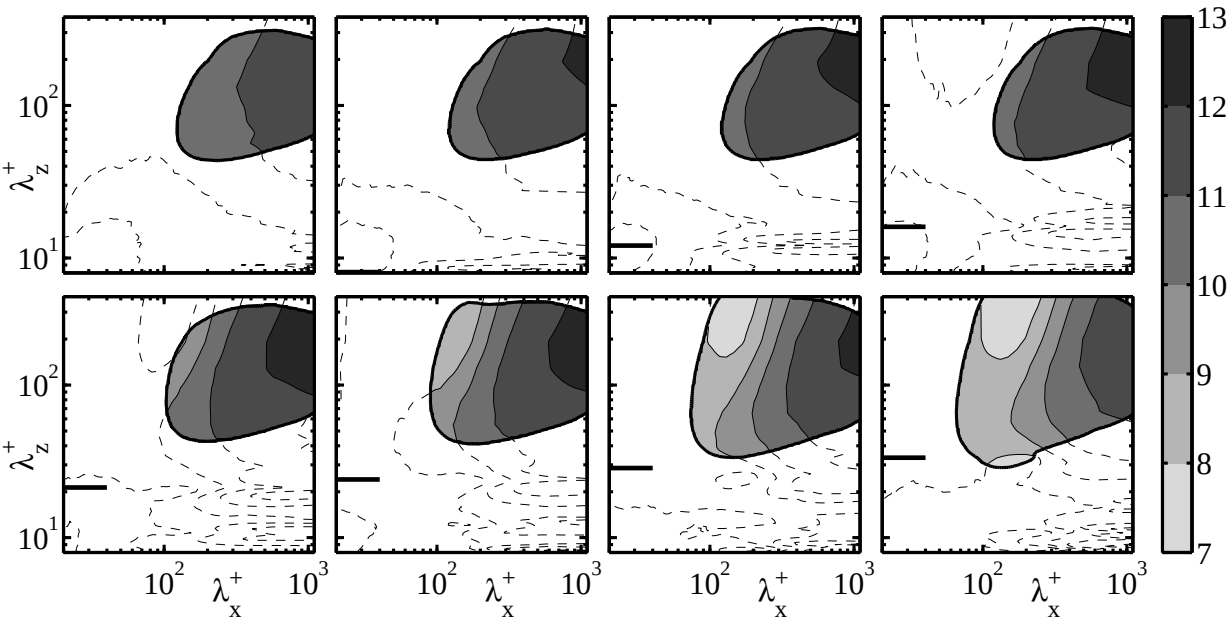

Figure 5.18: Spectral distribution of the convection velocity C_w^+ of w-structures at $y^+ \approx 5$ for cases 0S to 20S. The lines and contours are the same as in figure 5.16, with the solid line encircling the shaded region representing the threshold $k_x k_z E_{ww} = 0.026\, w_\tau^2$.

The schemes for C_v and C_w are defined analogously. The spectral distributions are portrayed for $y^+ \approx 5$ in figures 5.16, 5.17 and 5.18. For the spectral region of the new spanwise structures, the advection velocities are noticeably lower than for the spectral region of the regular ones. Near the wall, for $y^+ \lesssim 15$, the latter are of order $10\, u_\tau$, while the former are $6 - 8\, u_\tau$. The effect becomes more noticeable for the larger riblets, and suggest that the structures are not advected by the local flow, but correspond to unstable eigenstructures with a y-support extended below the riblet-tip plane. We will analyze this instability in chapter 7 with a generalized linear stability model.

Chapter 6

Results from DNSs of channels with blade riblets at $\mathrm{Re}_\tau \approx 550$

In the present chapter, results for riblet channels at $\mathrm{Re}_\tau \approx 550$ are presented. To our knowledge, no similar set of simulations has ever been reported. In fact, all previous DNSs with riblets have been conducted at $\mathrm{Re}_\tau \approx 180$ (Choi *et al.*, 1993; Chu & Karniadakis, 1993; Stalio & Nobile, 2003; Orlandi *et al.*, 2006; El-Samni *et al.*, 2007; Wassen *et al.*, 2008; Kramer *et al.*, 2010). In principle, the effect of the Reynolds number should be small, because riblets seem to interact only with the near-wall structures, so their presence should only affect the flow in the buffer layer. However, results of simulations at $\mathrm{Re}_\tau \approx 180$ should always be treated with care, since for such low Re_τ the flow is only marginally turbulent. It is our belief that some higher Reynolds number simulations were needed in the community, at least to confirm the validity of the DNSs at low Re_τ. Part of the reason for such simulations not having been conducted before is that the computational cost is prohibitive, especially because of the high spanwise resolution required near the riblet surfaces. It is worth noting that our parallelization strategy, which involves dividing the domain in constant-y planes, reaches for these simulations its limit of application. Due to memory limitations, not more than a single wall-block, fine-grid plane can be assigned to each individual computing process. In other words, if the domain is divided into its smallest elements, it barely 'fits' in the machine, and this cannot be circumvented by further division. For simulations at higher Re_τ, a finer parallelization strategy would therefore be required.

Given the high computational cost, we have only conducted simulations for a few cases, selecting them so that they were representative of the different flow conditions. We have also tuned the simulations to closely match ℓ_g^+ values from the set of simulations of

Case	ℓ_g^+	s^+	Re_τ	$c_f \times 10^3$	$DR(\%)$
0L	0	0	558.05	4.51	0
7L	7.21	11.77	546.85	4.36	3.38
13L	12.45	20.32	544.19	4.35	3.71
20L	20.52	33.51	571.76	4.77	-5.74

Table 6.1: Parameters resulting from DNSs at $\mathrm{Re}_\tau \approx 550$. ℓ_g^+ is the square root of the groove cross-section; s^+ is the riblet spacing; Re_τ is the friction Reynolds number; c_f is the friction coefficient; and DR is the drag reduction.

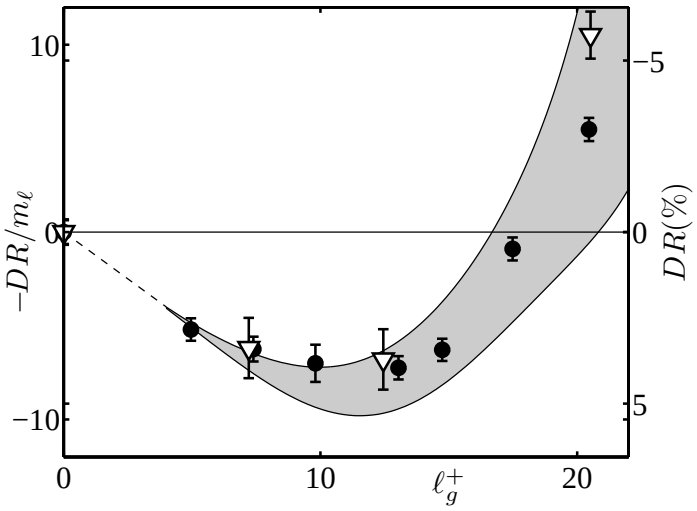

Figure 6.1: Drag-reduction results from DNSs of channels with rectangular riblets at $\mathrm{Re}_\tau \approx 550$ compared with those of chapter 5. $\triangledown$, results for cases 0L, 7L, 13L and 20L, normalized using equation (2.10), with protrusion heights obtained from a second-order finite-differences Stokes simulation with the same effective resolution as the DNSs, and the value for μ_0 from Jiménez (1994). ●, results at $\mathrm{Re}_\tau \approx 185$ from chapter 5, also normalized using equation (2.10). The error bars have been estimated from the time-history of DR, following Hoyas & Jiménez (2008). The shaded area is the envelope of the experimental data in figure 2.3(d).

the previous chapter, so that direct comparisons could be made. Thus, we have simulated a smooth reference case, 0L, one in the viscous regime, 7L, one near the optimum performance, 13L, and one well past the viscous breakdown, 20L. The parameters resulting from the simulations are summarized in table 6.1. Throughout the chapter, we will compare the present results with those of the corresponding simulations 0S, 7S, 13S and 20S at $\mathrm{Re}_\tau \approx 185$.

The drag reduction results of the present simulations are portrayed in figure 6.1, together with the results at $\mathrm{Re}_\tau \approx 185$ of figure 5.1. The new results have been scaled with

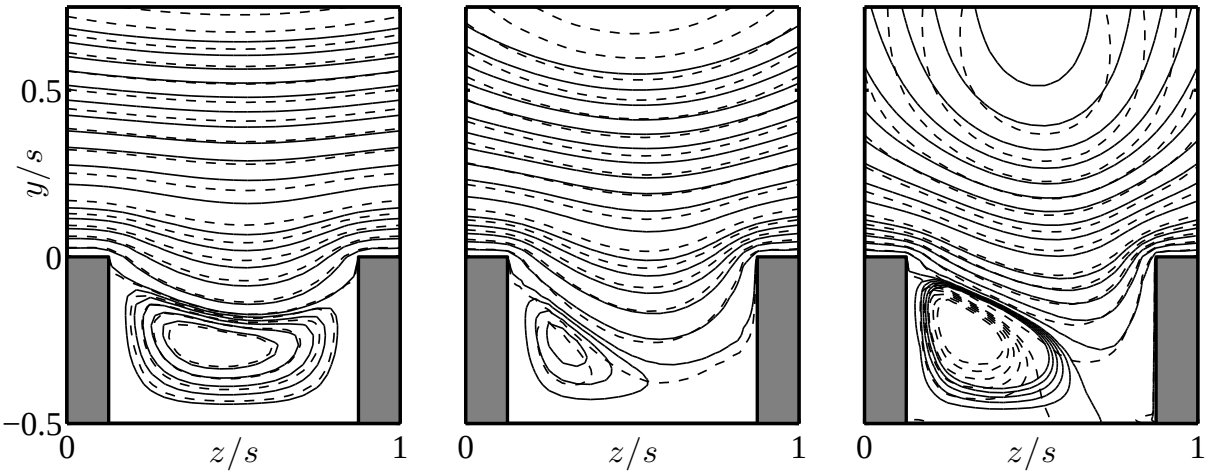

Figure 6.2: Streamfunction of the conditionally averaged crossflow above and within the riblet grooves, conditioned to a mean rightwards flow in the plane immediately above the riblet tips. From left to right, $\ell_g^+ \approx 7$, $\ell_g^+ \approx 13$ and $\ell_g^+ \approx 20$. To enhance the comparison between the different cases, the streamfunction has been scaled for each case with the corresponding u_τ and riblet height h. ——, results from the present simulations at $\mathrm{Re}_\tau \approx 550$, cases 7L, 13L and 20L. – – – –, results from the cases 7S, 13S and 20S of chapter 5, at $\mathrm{Re}_\tau \approx 185$. The contour levels are the same as in figure 5.2(a).

a viscous slope m_ℓ calculated using equation (2.10) with $c_{f0} = 4.51 \times 10^{-3}$, corresponding to the smooth wall at $\mathrm{Re}_\tau \approx 550$, like the previous set was scaled with the slope obtained for $\mathrm{Re}_\tau \approx 185$. Therefore, the scale for DR at the right-hand-side ordinate axis only applies to the results at $\mathrm{Re}_\tau \approx 550$. The comparison with the DR results of figure 5.1 indicates that the performance in terms of DR drops roughly to 0.85 times its value at $\mathrm{Re}_\tau \approx 185$, because of the change in equation (2.2) of the friction coefficient. On the other hand, the performance in terms of ΔB, or DR/m_ℓ, remains essentially unaltered, supporting the reduced scaling discussed in §2.1.

6.1 The conditional flow

Once more, we have compiled statistics of the flow near the ribbed surface conditioned both on the spanwise position across the riblet and on the mean direction of the crossflow in the plane immediately above the tips. We have followed the procedure described in §5.1. The mean conditioned crossflows within the grooves are portrayed in figure 6.2 for simulations 7L, 13L, and 20L, compared with the corresponding simulations at $\mathrm{Re}_\tau \approx 185$. The same evolution of the recirculation bubbles can be observed, with increasing asym-

metry for the larger riblets. The flows remain weak inside the grooves and very similar to those at $\mathrm{Re}_\tau \approx 185$, although there is some modulation coming from the overlying turbulence. The difference is most apparent for the case 20L for which, if the lengths are measured with the riblet dimension, as has been done in the figure, the riblets see the peak of the velocity perturbations closer than in the other cases. The higher peak values of v'^+ and w'^+ are a Reynolds number effect common to the smooth wall case (see figures 3.7(c) and (d)), and essentially independent of the presence of riblets.

6.2 Spectral analysis

To investigate the presence of spanwise rollers, we have again compiled the spectral distribution of the flow variables for simulations 7L, 13L and 20L, as in §5.2. Some results are portrayed in figures 6.3 to 6.7, which contain examples of two-dimensional spectral energy densities over wall-parallel planes at several heights y^+ over the riblet peaks. The spectral densities are compared with those of cases 7S, 13S and 20S at $\mathrm{Re}_\tau \approx 185$.

The figures show the increase in the mean intensity mentioned in the previous section. The increase is largest for the wall-normal velocity and for the pressure fluctuations (del Álamo & Jiménez, 2003), and very small for the streamwise velocity ones (see figures 3.7(c) and (d) for a comparison between the velocity fluctuations in the case of smooth channels). Besides this riblet-independent effect, the appearance of the spanwise structures at roughly the same range of streamwise wavelengths, $\lambda_x^+ \approx 100 - 200$, can be observed. The structures extend again for heights below $y^+ \approx 15 - 20$, depending on the variable considered, with the widest vertical ranges corresponding to wall-normal velocity and pressure fluctuations, portrayed in figures 6.4 and 6.7 respectively.

On the other hand, while the typical lengths remain the same, there is a slight increase in the intensity of the spanwise structures, in accordance with the mean increase of the fluctuations. That is most apparent for the spectral density of v^2 and $-uv$ of case 20L, shown in figures 6.4(c) and 6.6(c). For the intermediate case 13L, this higher intensity even leads to the structures leaving a 'footprint' in the spectral distributions of v^2 and $-uv$ for $y^+ \lesssim 5$, which was not present for $\mathrm{Re}_\tau \approx 185$, as can be seen in the first panels of figures 6.4(b) and 6.6(b).

The spectral densities of the new simulations also have an interesting by-product. Since the size in wall units of the simulation domain is now much larger, $L_x^+ \times L_z^+$ of order 5000×2500 compared to the previous 1000×400, the new spectral densities are not artificially cropped for the higher wavelengths, at least near the wall, which is the region

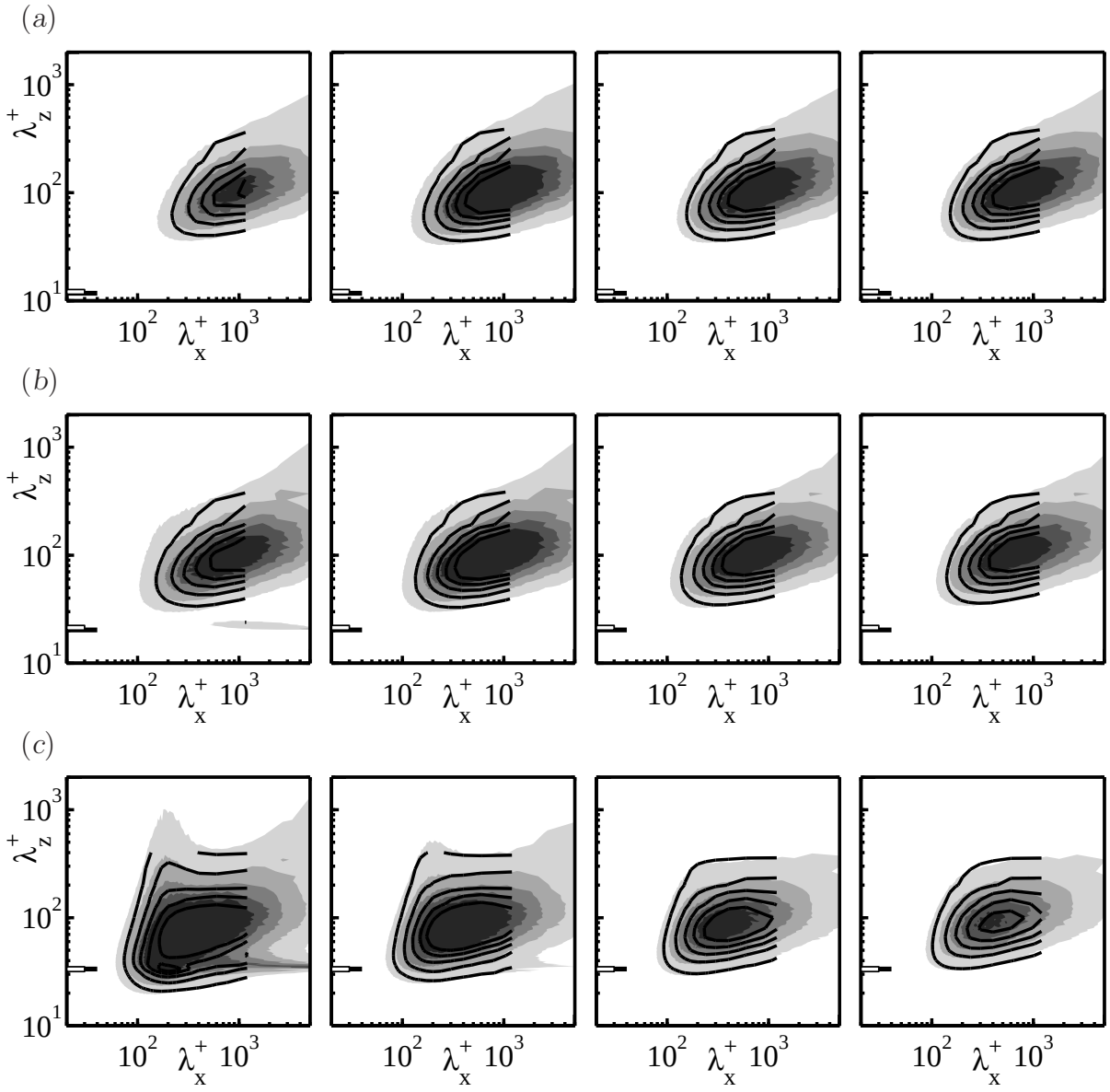

Figure 6.3: Spectral energy density of the streamwise velocity, $k_x k_z E_{uu}$, for cases (*a*) 7L, (*b*) 13L and (*c*) 20L. From left to right, at $y^+ \approx 2$, 5, 7 and 10, with the contour increments 0.04, 0.09, 0.15 and $0.20\,u_\tau^2$ respectively. For comparison, the same contours for the corresponding cases 7S, 13S and 20S at $\mathrm{Re}_\tau \approx 185$ are superimposed as solid lines. The black thick horizontal line to the left of the plots marks the riblet spacing for the cases at $\mathrm{Re}_\tau \approx 550$, and the white one for those at $\mathrm{Re}_\tau \approx 185$.

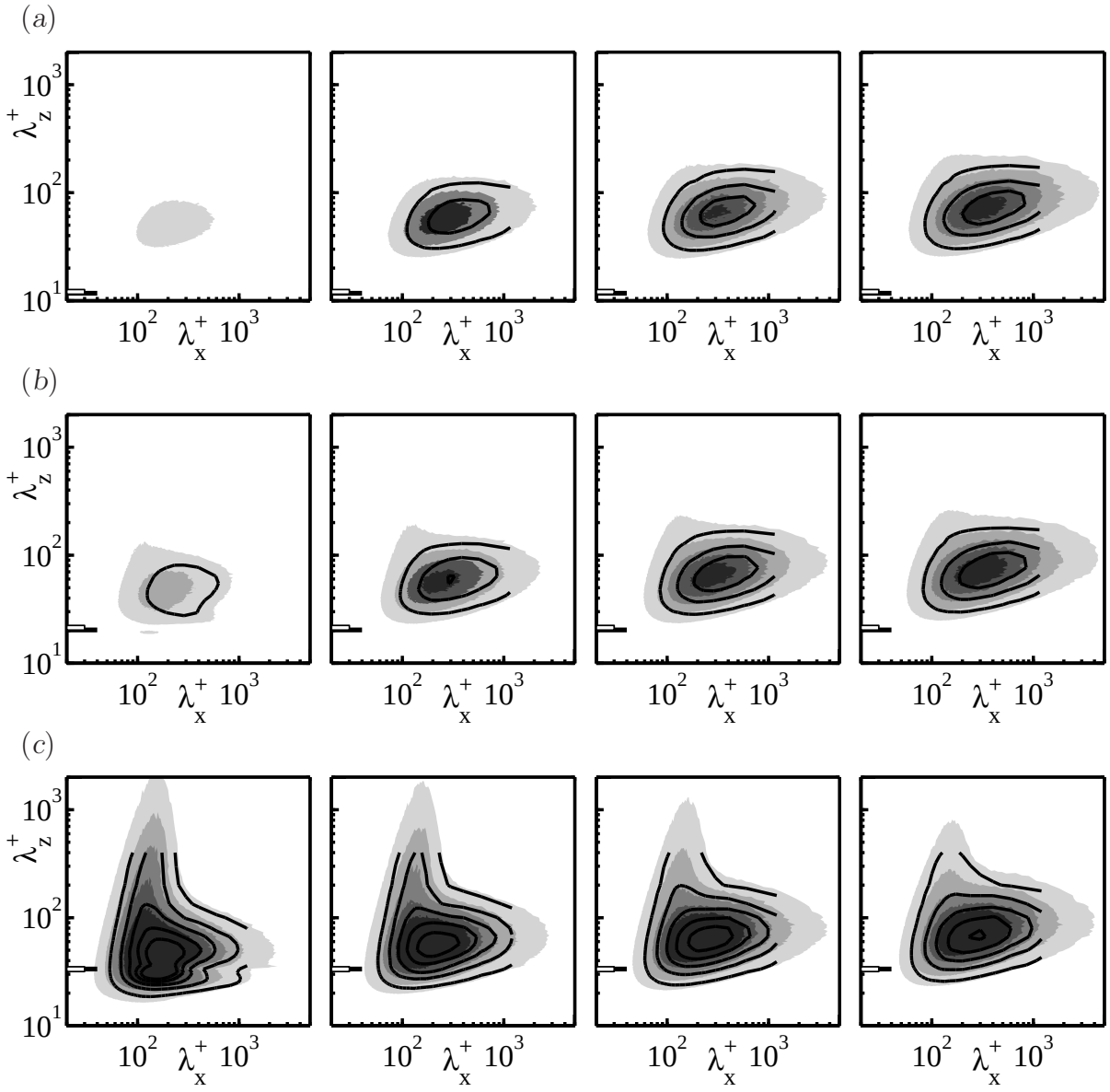

Figure 6.4: Spectral energy density of the wall-normal velocity, $k_x k_z E_{vv}$, for cases (*a*) 7L, (*b*) 13L and (*c*) 20L. From left to right, at $y^+ \approx 5$, 10, 15 and 20, with the contour increments 0.005, 0.010, 0.015 and $0.020\,u_\tau^2$ respectively. For comparison, the same contours for the corresponding cases 7S, 13S and 20S at $\mathrm{Re}_\tau \approx 185$ are superimposed as solid lines. The black thick horizontal line to the left of the plots marks the riblet spacing for the cases at $\mathrm{Re}_\tau \approx 550$, and the white one for those at $\mathrm{Re}_\tau \approx 185$.

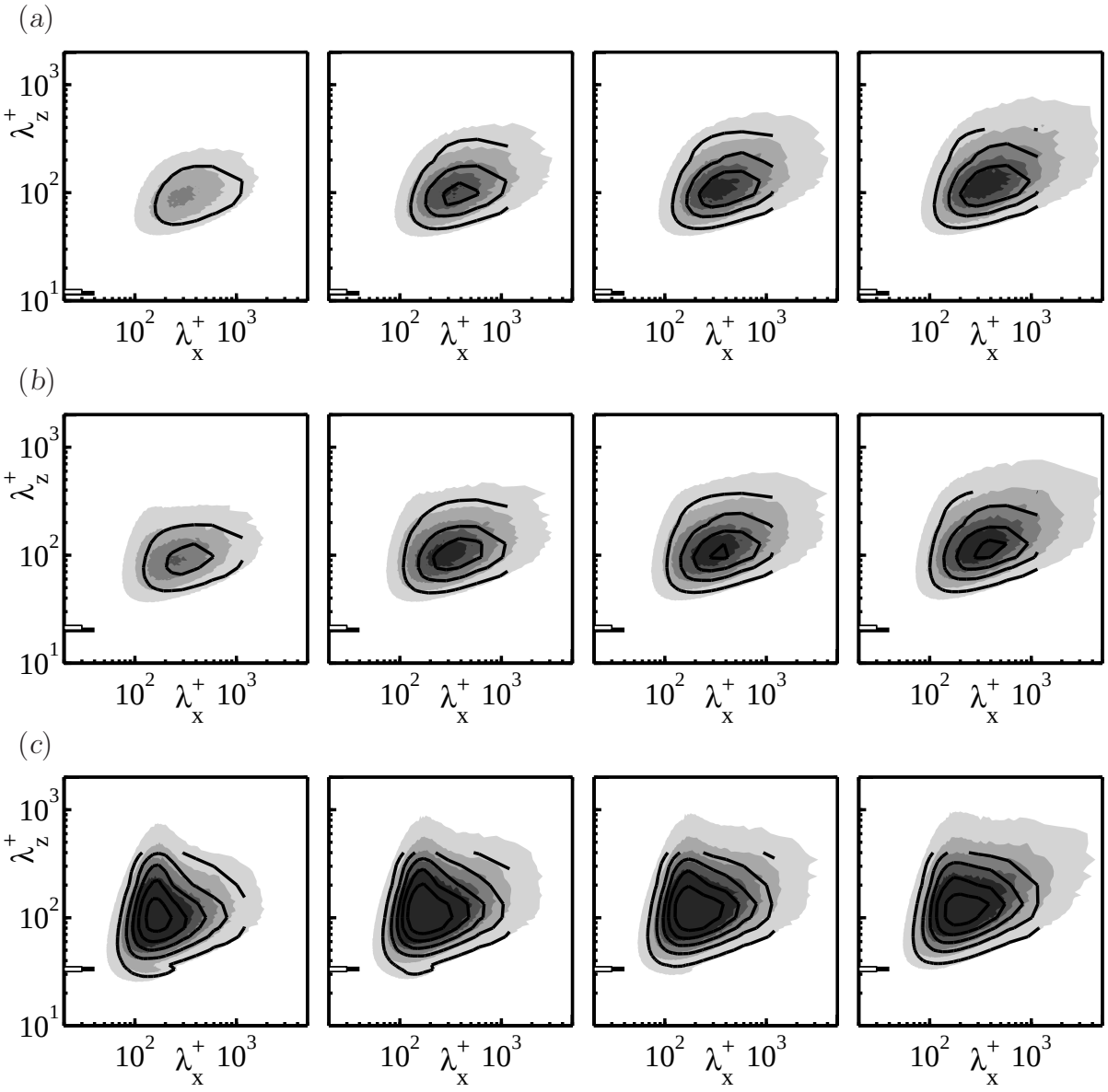

Figure 6.5: Spectral energy density of the spanwise velocity, $k_x k_z E_{ww}$, for cases (*a*) 7L, (*b*) 13L and (*c*) 20L. From left to right, at $y^+ \approx 2$, 5, 7 and 10, with the contour increments 0.020, 0.030, 0.035, and $0.040\,u_\tau^2$ respectively. For comparison, the same contours for the corresponding cases 7S, 13S and 20S at $\mathrm{Re}_\tau \approx 185$ are superimposed as solid lines. The black thick horizontal line to the left of the plots marks the riblet spacing for the cases at $\mathrm{Re}_\tau \approx 550$, and the white one for those at $\mathrm{Re}_\tau \approx 185$.

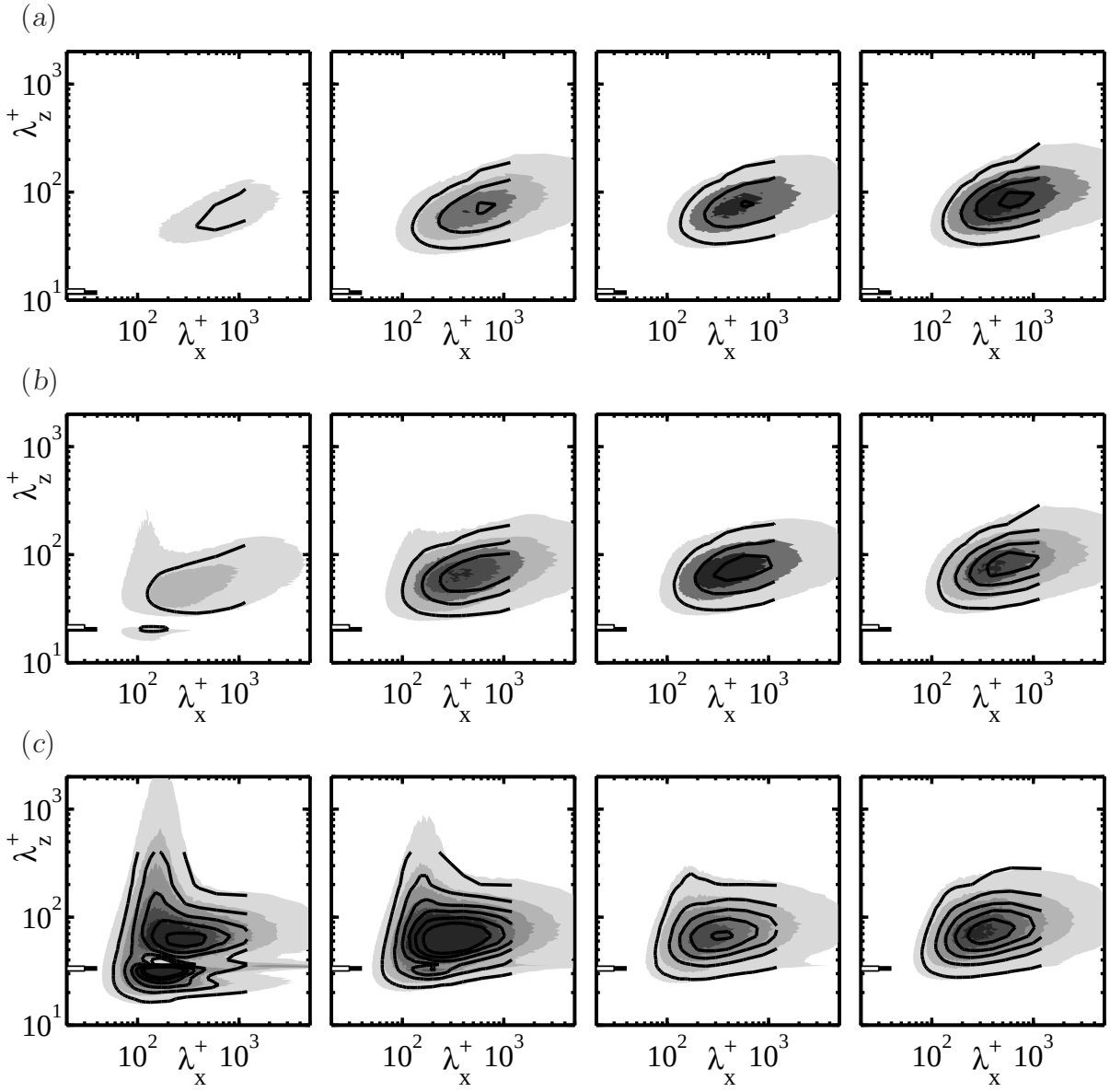

Figure 6.6: Spectral energy density of the Reynolds stress, $-k_x k_z E_{uv}$, for cases (*a*) 7L, (*b*) 13L and (*c*) 20L. From left to right, at $y^+ \approx 2$, 5, 7 and 10, with the contour increments 0.005, 0.010, 0.025, and $0.030\,u_\tau^2$ respectively, starting at half their values. For comparison, the same contours for the corresponding cases 7S, 13S and 20S at $\mathrm{Re}_\tau \approx 185$ are superimposed as solid lines. The black thick horizontal line to the left of the plots marks the riblet spacing for the cases at $\mathrm{Re}_\tau \approx 550$, and the white one for those at $\mathrm{Re}_\tau \approx 185$.

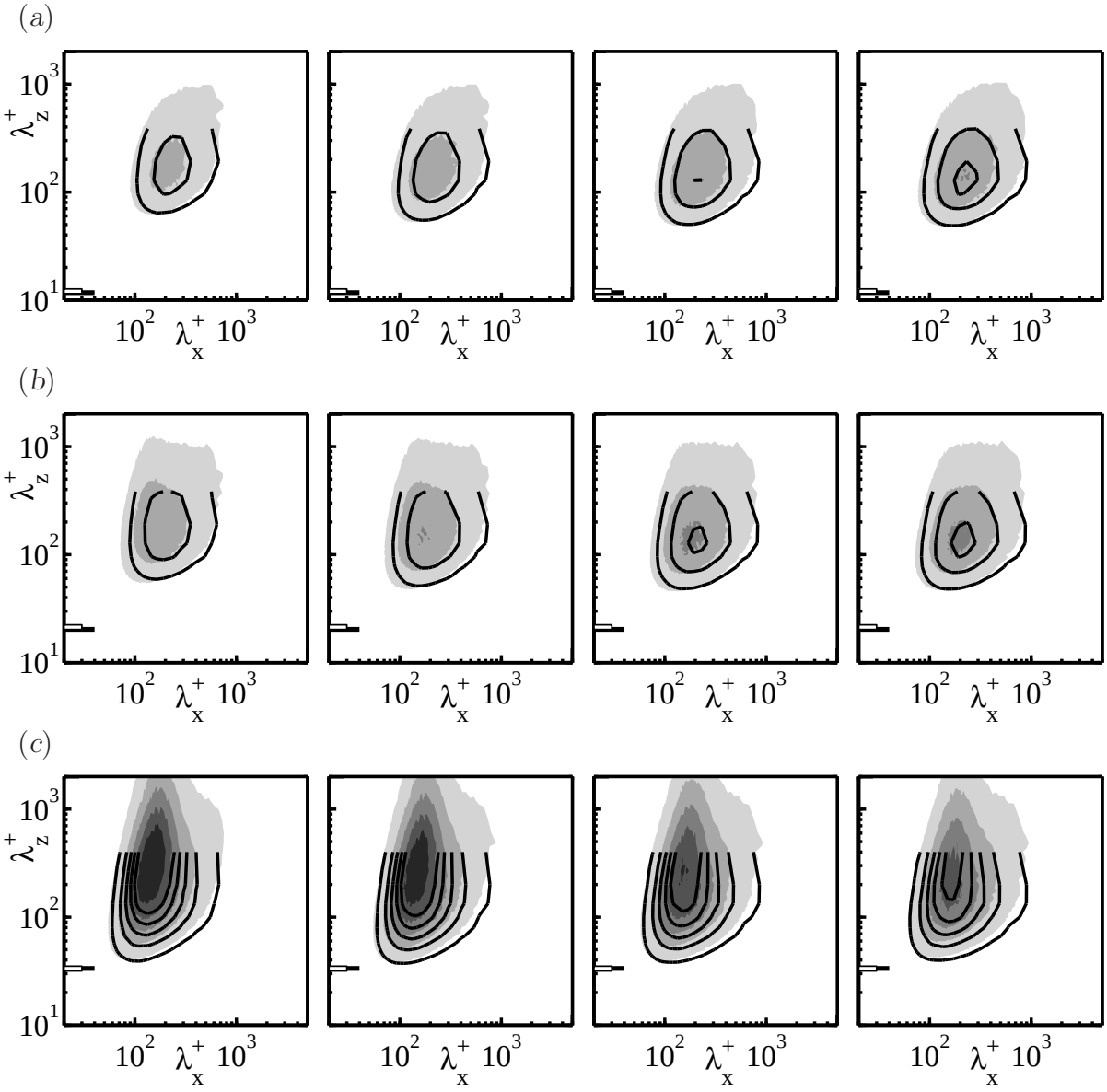

Figure 6.7: Spectral energy density of the pressure fluctuations, $k_x k_z E_{pp}$, for cases (*a*) 7L, (*b*) 13L and (*c*) 20L. From left to right, at $y^+ \approx 5$, 10, 15 and 20. For comparison, contours for the corresponding cases at $\mathrm{Re}_\tau \approx 185$, 7S, 13S and 20S, are superimposed as solid lines. The contour increments are $0.4\,u_\tau^4$ for the cases at $\mathrm{Re}_\tau \approx 550$ and $0.2\,u_\tau^4$ for the cases at $\mathrm{Re}_\tau \approx 185$. The black and the white thick horizontal lines to the left of the plots mark the respective riblet spacings.

we are interested in. Thus, we have now been able to obtain the full spectral distribution of the flow variables, and to bound the typical spanwise wavelength of the new structures. In chapter 5 we could only say that they could be as wide as the simulation domain, while now we can affirm that they are not longer than $\lambda_z \approx 1000 - 2000$. Nevertheless, since $\lambda_z \gg \lambda_x$ and $\lambda_z \gg \lambda_y$, with $\lambda_y \approx 10 - 20$ being the typical height above the riblet peaks, the hypothesis that the structures are elongated in the spanwise direction is confirmed.

Beyond the validation of results for low Reynolds number, we were also interested in clarifying the scaling of the rollers. As we discussed in §5.2, the absence of sufficient disparity in Re_τ for the simulations of chapter 5 made impossible to establish whether the size of the rollers scaled with outer or wall units. The evidence for that discussion is now available. From figures 6.3 to 6.7 it is clear that the structures scale in wall units, but the scaling can be more clearly appreciated in figure 6.8. The latter figure compares, for cases 13S and 20S at $\mathrm{Re}_\tau \approx 185$, and cases 13L and 20L at $\mathrm{Re}_\tau \approx 550$, the distribution in y and in streamwise wavelengths of the additional energy, taking as reference the corresponding smooth wall, stored in the spectral region that corresponds to the new structures. For the comparison, the spectral densities are portrayed with the length scales normalized both with the wall unit, ν/u_τ, and the channel half-width δ. The hypothesis of inner scaling of §5.2 is confirmed, since the figure shows that the spectral densities lie in the same region for the two different Reynolds numbers when using wall scaling, and that they do not when outer units are used. Furthermore, there is a ratio of roughly three in the sizes when scaling with δ, which is what should be expected from the ratio in Re_τ, $550/185 \approx 3$, for structures that scale in wall units.

The drag breakup analysis of §5.2.1 can be repeated for the present simulations to compare the different contributions to DR. According to the discussion in that section, the first contribution T_1 should be a factor that accounts for the differences in the setup of the smooth and ribbed channels, both in height and in mass flux, and its definition implies that it should vanish for $\mathrm{Re}_\tau \to \infty$. That would leave only the terms T_2, which represents the slip velocity at the riblet tips, and T_3, which accounts for the extra Reynolds stresses in the flow over the riblets. These last two terms are the only ones with physical meaning, since the first one is merely an adjustment parameter to account for a setup constrained by limited resources, *i.e.* with low Reynolds number.

The three contributions are shown in figure 6.9 for cases 0L to 20L, compared with the results for $\mathrm{Re}_\tau \approx 185$ of §5.2.1. We can appreciate that the influence of T_1 is indeed reduced. In turn, T_3 increases, making up for most of the decrease in T_1. This increase is a direct consequence of the higher intensities found in the $-uv$ cospectrum, portrayed in

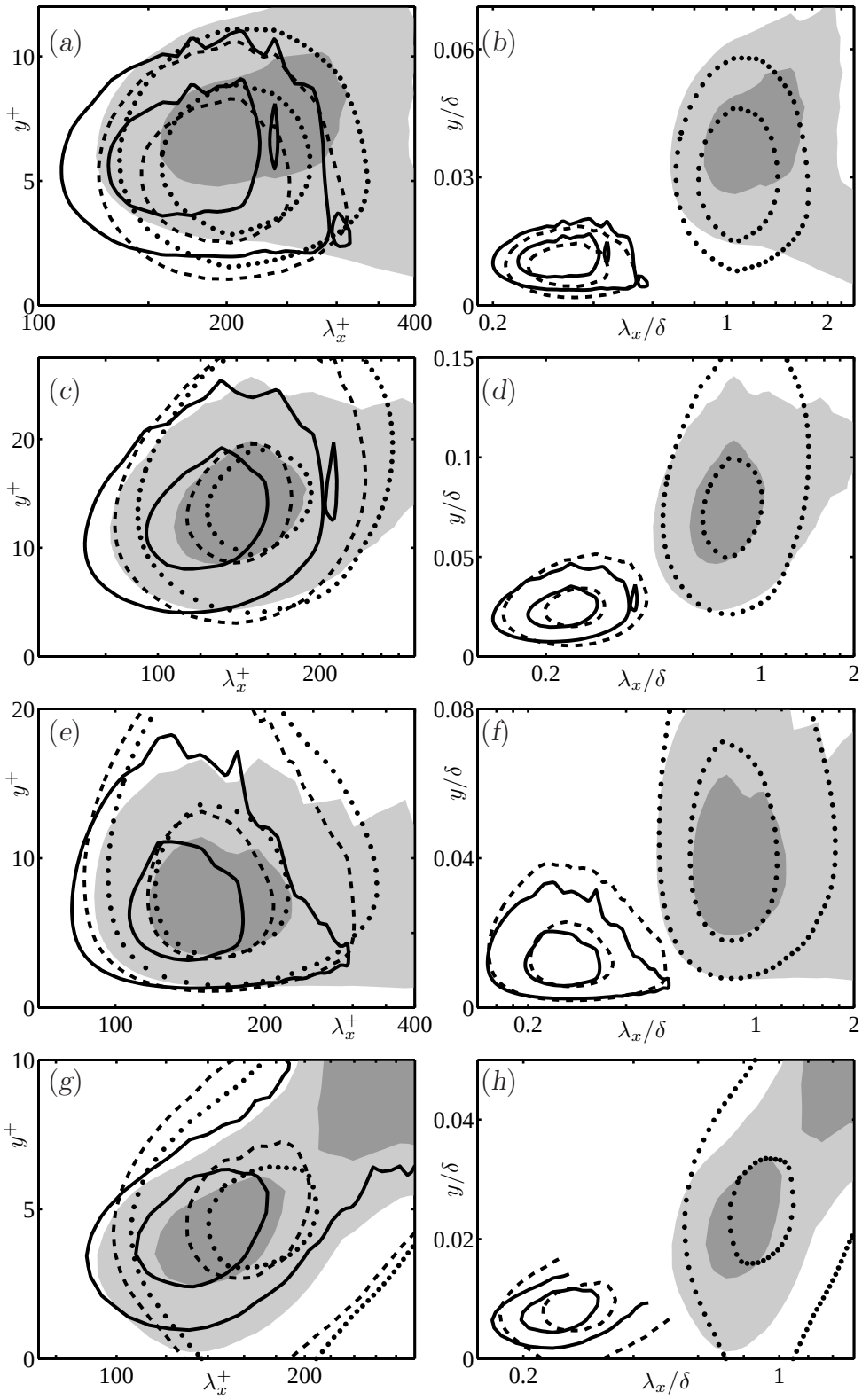

Figure 6.8: Increment in the spectra of the flow variables caused by the presence of riblets, integrated for $\lambda_z^+ > 130$. (*a–b*), $\Delta(k_x E_{u^2})$; (*c–d*), $\Delta(k_x E_{v^2})$. (*e–f*), $\Delta(k_x E_{w^2})$; (*g–h*), $\Delta(-k_x E_{uv})$. Figures are scaled in wall units in the first column, and with the channel half-height δ in the second. Shaded, case 13S; ·····, 20S; ——, 13L; – – – –, 20L. The isolines drawn have been chosen to enhance the comparison of the scales in the four cases considered, regardless of their magnitude.

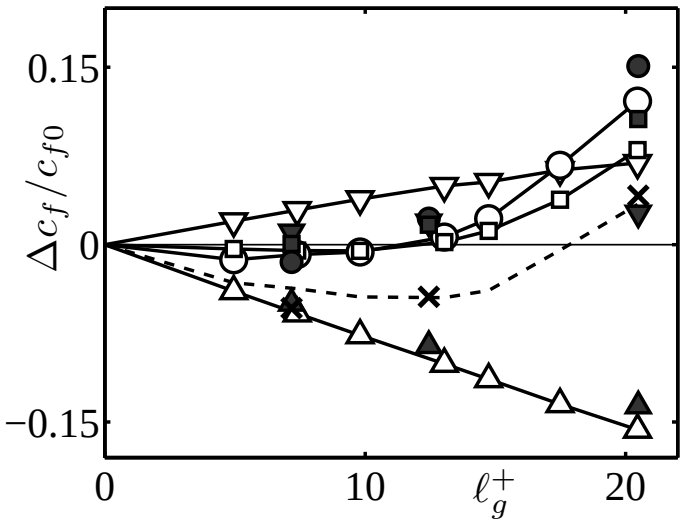

Figure 6.9: Contributions T_1, T_2 and T_3 to the drag reduction curve, as defined by equations (5.8)–(5.10). ▼, T_1 for cases 7L, 13L and 20L; -▽-, T_1 for $\mathrm{Re}_\tau \approx 185$; ▲, T_2 for cases 7L, 13L and 20L; -△-, T_2 for $\mathrm{Re}_\tau \approx 185$; ●, total T_3 for cases 7L, 13L and 20L; -○-, total T_3 for $\mathrm{Re}_\tau \approx 185$; ■, T_3 for cases 7L, 13L and 20L, calculated considering only uv within $65 \leq \lambda_x^+ \leq 290$, $\lambda_z^+ \geq 50$, and $y^+ \lesssim 35$; -□-, the same contributions for $\mathrm{Re}_\tau \approx 185$; ×, total drag reduction, $T_1 + T_2 + T_3$, for cases 7L, 13L and 20L; ----, total drag reduction for $\mathrm{Re}_\tau \approx 185$.

figure 6.6. Again, most of T_3 is produced in the spectral region of the new structures.

The structures appear in the time-evolving flow as rollers, very similar to those observed for low Re_τ. To illustrate this, two instantaneous realizations, obtained from simulations 13L and 20L, of the wall-normal velocity at a y-plane near the riblet peaks, are portrayed in figure 6.10. In the first one, for ℓ_g^+ slightly larger than the optimum, the spanwise coherence of the flow seems weak, and the realization resembles greatly one of a smooth channel, save for the proximity of the riblet peaks, that induces streamwise strips of very low v, separated from each other by the riblet spacing. In the second realization, for large ℓ_g^+, the rollers are fully developed, and their spanwise coherence across several riblet grooves can be more easily appreciated, overlapped with the background modulation by the larger, outer structures. Again, the presence of the riblet peaks disrupts the flow with riblet-spacing periodicity, although it does not impede the manifestation of the spanwise coherence. For comparison with the rollers at $\mathrm{Re}_\tau \approx 185$, we have superimposed figure 5.15(b), scaled so the wall units for both visualizations coincide. The latter image was obtained for case 17S, but in spite of the slightly smaller riblet spacing, and its smaller associated spanwise-periodic disruption, the rollers have roughly the same appearance and characteristic streamwise wavelength, $\lambda_x^+ \approx 150$.

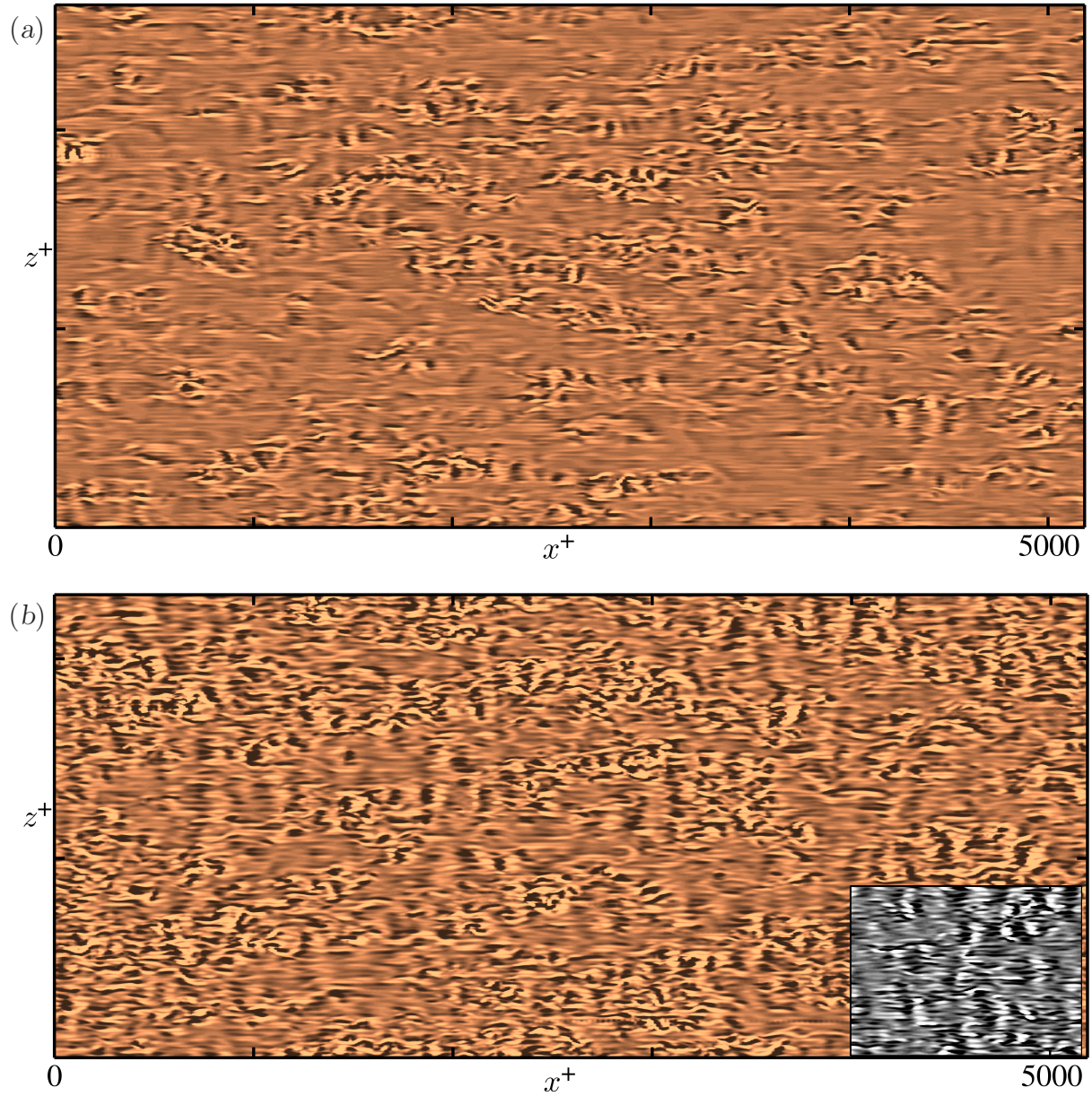

Figure 6.10: Instantaneous realizations of the wall-normal velocity in riblet channels with $\mathrm{Re}_\tau \approx 550$, at the plane $y^+ \approx 4$. The clear regions represent negative velocities, or flow towards the wall, and the dark regions positive ones. (*a*) Case 13L. (*b*) Case 20L. For comparison with the channels at $\mathrm{Re}_\tau \approx 185$, figure 5.15(*b*) for case 17S has been reproduced in the lower right corner, with the same scale for the wall unit of length ν/u_τ.

Chapter 7

A linear stability model

In this chapter we propose a simplified model for the Kelvin–Helmholtz-like instability introduced in chapter 5, which captures the essential physics involved, including the effect of the riblet geometry on the instability. This model does not intend to capture the precise stability characteristics of any particular flow over any particular geometry, but rather to provide a simple tool with which the key features of the instability can be identified in a general fashion. The precise analysis of a particular case would require a finer model, but the general character would be lost with the refinement.

Since the spanwise rollers are quasi-two-dimensional in x–y, we restrict ourselves to two-dimensional solutions of the linearized Navier–Stokes equations. Denoting by prime superscripts the derivatives with respect to y of the base flow U, we have

$$\frac{\partial u}{\partial t} + U\frac{\partial u}{\partial x} + v\,U' = -\frac{\partial p}{\partial x}, \tag{7.1}$$

$$\frac{\partial v}{\partial t} + U\frac{\partial v}{\partial x} = -\frac{\partial p}{\partial y}, \tag{7.2}$$

where lower-case symbols are perturbations. The viscous terms are omitted for simplicity, since we are looking for essentially inviscid Kelvin–Helmholtz-like instabilities, on which viscosity would only have a damping effect. Imposing incompressibility, the Rayleigh equation for v is,

$$\left(\frac{\partial}{\partial t} + U\frac{\partial}{\partial x}\right)\nabla^2 v = U''\frac{\partial v}{\partial x}, \tag{7.3}$$

for which we seek solutions of the form $v = \widehat{v}(y)\mathrm{e}^{\mathrm{i}\alpha(x-ct)}$.

The problem is solved in a notional domain between the two planes of the riblet tips, $y \in (0, 2\delta)$, and the two-dimensionality is preserved by using z-independent boundary conditions that account for the presence of riblets in a spanwise-averaged sense.

Consider the lower wall. The first step is to describe the flow along the grooves, where variables will be denoted by the subscript 'g'. This part of the problem takes place in the

real groove geometry in $y \in (-h, 0)$. Since we are interested in the onset of the instability, we will assume that the effective Reynolds number is low, and that the longitudinal flow along the grooves satisfies approximately the viscous Stokes equations. Note that this approximation is consistent with the behavior of the conditioned average streamwise velocity in the direct simulations, as discussed in §5.1. We also assume that the longitudinal velocity gradients within the grooves are small with respect to the transverse ones, and that the dynamical effect of the transverse velocities can be neglected. In particular, we neglect the variation across the groove of the streamwise pressure gradient, and the streamwise contributions of the viscous term. The streamwise momentum equation within the groove is then,

$$\frac{\partial^2 u_g}{\partial y^2} + \frac{\partial^2 u_g}{\partial z^2} \equiv \nabla^2_{yz} u_g = \frac{1}{\nu} \frac{\mathrm{d}p_g}{\mathrm{d}x}. \tag{7.4}$$

The velocity satisfies $u_g = 0$ at the groove walls, and we will assume that $\partial u_g/\partial y = 0$ at the plane of the riblet tips. Note that the last boundary condition refers to the perturbations, and is not equivalent to assuming that the mean velocity gradient vanishes at $y = 0$. The assumption is that the streamwise pressure gradient is predominantly balanced by the viscous stresses at the groove walls, rather than by those at the interface with the outer flow. That assumption is especially adequate for small riblets, but has to be justified *a posteriori*. For example, consider the solutions in figure 7.4, which are obtained by coupling the outer flow perturbations to grooves with the no-slip condition at their top interface. The length scales of the perturbations at $y = 0$ scale in wall units, essentially because the true outer boundary condition for the flow within the grooves, $\partial u_g/\partial y = 0$, should have been applied at $y \to \infty$, and involves the overlying velocity profile. In the particular case of the figure, $(\partial u/\partial y)^+ \approx 0.10 u^+|_{y=0}$. On the other hand, the gradients over the walls of the grooves, not shown in the figure, are inversely proportional to the groove diameter. For a typical groove, $(\partial u_g/\partial n)^+ \approx 4u^+|_{y=0}/\ell_g^+$. The assumption that the shear at the groove top can be neglected with respect to that at the walls is valid as long as $\ell_g^+ \ll 40$, which is enough to explore the onset of the instability. The same assumption also allows us to use an inviscid approximation for the outside flow, even while using a Stokes model for the flow in the groove.

The coupling of the grooves and the body of the channel is made by assuming that the outside pressure drives the flow along the grooves, and that the transpiration velocity at $y = 0$ is due to the longitudinal variations of the volumetric flux of u_g.

Since the right-hand side of equation (7.4) is only a function of x and t, we can write

$$u_g = -\left(\frac{1}{\nu}\frac{\mathrm{d}p_g}{\mathrm{d}x}\right) f(y, z)\,, \tag{7.5}$$

where $f(y,z)$ verifies

$$\nabla^2_{yz} f = -1, \tag{7.6}$$

with boundary conditions identical to those for u_g, so that f depends only on the groove geometry. The streamwise variation of u_g is related to the z-averaged transpiration velocity v at $y=0$ by integrating the continuity equation over the groove cross-section:

$$\frac{\partial}{\partial x}\iint_{A_g} u_g \,\mathrm{d}y\,\mathrm{d}z + \int_s v_g|_{y=0}\,\mathrm{d}z = 0, \tag{7.7}$$

$$v|_{y=0} = -\frac{1}{s}\frac{\partial}{\partial x}\iint_{A_g} u_g \,\mathrm{d}y\,\mathrm{d}z. \tag{7.8}$$

Note that s in (7.8) is the distance between neighboring riblets, not the width of the groove, because v needs to be averaged over the whole $y=0$ plane to be used as a boundary condition for (7.3). Introducing (7.5) into (7.8), and assuming that $p|_{y=0}=p_g$, we obtain

$$\left.\frac{\partial^2 p}{\partial x^2}\right|_{y=0} = \frac{\nu}{L_w^3}\, v|_{y=0}\,, \tag{7.9}$$

where

$$L_w^3 = \frac{1}{s}\iint_{A_g} f \,\mathrm{d}y\,\mathrm{d}z \tag{7.10}$$

Using (7.9) to eliminate the pressure from the longitudinal momentum equation (7.1), yields the boundary condition

$$\left(\frac{\partial}{\partial t} + U\frac{\partial}{\partial x}\right)\frac{\partial v}{\partial y} = U'\frac{\partial v}{\partial x} \mp \frac{\nu}{L_w^3} v, \tag{7.11}$$

where the two signs of the last term apply respectively to the upper and lower walls. If we denote the values of the mean profile at $y=0$ by U_0 and U_0', (7.11) can be rewritten as

$$(U_0 - c)\frac{\partial \widehat{v}}{\partial y} = \left(U_0' \pm \mathrm{i}\frac{\nu}{\alpha L_w^3}\right)\widehat{v}. \tag{7.12}$$

Equation (7.12) shows that U_0 changes only the real part of the advection velocity by a fixed amount. From the point of view of the stability characteristics of the flow, it can be assumed to be zero. The solutions of the system (7.3)–(7.12) depend only on the base flow profile $U(y)$ and on the characteristic penetration length L_w, which is linked to the groove cross-section through the integral in (7.10). The viscosity can be eliminated by expressing everything in wall units. It turns out that, for conventional geometries, L_w is closely linked to the empirical parameter $\ell_g = \sqrt{A_g}$ proposed in §2.2. For example, figure 7.1 compiles values of L_w computed for triangular, rectangular, and scalloped riblets, with

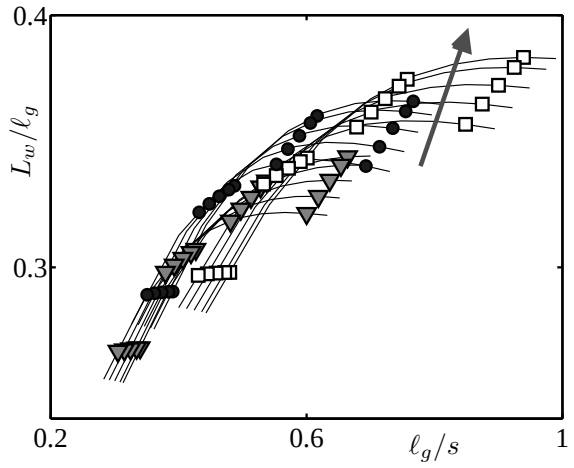

Figure 7.1: Value of the parameter L_w in (7.10), compared with ℓ_g, for ▼, triangular, ●, scalloped, and □, blade riblets. The solid lines connect riblets of the same type with equal tip width and variable depth-to-width ratio, ranging from $h/s = 0.2$ to 1.0, while the arrow indicates decreasing tip width, from $t_r/s = 0.5$ to 0.02.

depth-to-width ratios between 0.2 and 1.0, and tip widths between 2% and 50% of their spacing. The figure shows that, at least within that range of geometries, ℓ_g and L_w are essentially proportional to each other, with the approximation $L_w/\ell_g \approx 0.36$, or

$$\ell_g \approx 2.8\, L_w \tag{7.13}$$

having less than 10% error for conventional sharp riblets with $h/s \geq 0.4$. This result connects the present stability analysis with the discussion on the scaling of the viscous breakdown with ℓ_g^+ of §2.2, providing some theoretical justification for that empirically-deduced scaling.

7.1 The piecewise-linear profile

Before turning our attention to the quantitative analysis of the instability induced by the riblets on a turbulent velocity profile, it is useful to apply the previous formulation to a piecewise-linear base flow

$$U(y) = \begin{cases} U_\infty\, y/H & \text{for } y < H, \\ U_\infty & \text{for } y \geq H, \end{cases} \tag{7.14}$$

where the basic mechanisms are more easily understood. The solutions of (7.3) can then be expressed as combinations of exponentials, $\exp(\pm\alpha y)$, which are continuous everywhere,

vanish at infinity, and satisfy a jump condition for their derivatives at the singularity of U'' at $y = H$. The wall boundary condition (7.11) becomes a second order equation for the temporal eigenvalue,

$$-2\Lambda\sigma^2 + \left[-2\mathrm{i} + \Lambda\left(1 + 2\widetilde{\alpha} - \mathrm{e}^{-2\widetilde{\alpha}}\right)\right]\sigma + (\Lambda - \mathrm{i})\left(1 - 2\widetilde{\alpha} - \mathrm{e}^{-2\widetilde{\alpha}}\right) = 0, \qquad (7.15)$$

where $\widetilde{\alpha} = \alpha H$, $\sigma = (c/U_\infty)\,\widetilde{\alpha}$, and $\Lambda = (L_w/H)^3(U_\infty H/\nu)\,\widetilde{\alpha}$. Instability requires that the imaginary part, σ_I, of the eigenvalue be positive.

The smooth wall is recovered for $\Lambda = 0$ and has no unstable modes. For $0 < \Lambda \ll 1$, all the wavenumbers are weakly unstable, with a maximum growth rate, $\sigma_I \approx 0.081\Lambda$, at $\widetilde{\alpha} = 0.80$. In the opposite limit, $\Lambda \gg 1$, the eigenvalues become independent of Λ, and the unstable modes are restricted to the band $0 < \widetilde{\alpha} \lesssim 1.83$. The maximum growth rate is $\sigma_I \approx 0.25$ at $\widetilde{\alpha} \approx 1.23$. The growth rates and phase velocities of the unstable modes for intermediate values of Λ are given in figure 7.2.

The limit $L_w \gg H$ provides a physical interpretation of the nature of the instability. In this limit, which is essentially $\nu/L_w^3\alpha \ll U_0'$, the boundary condition (7.9) loses the term coming from the wall, and the mean velocity profile can be extended anti-symmetrically to $y < 0$, to become a piecewise-linear free shear layer. The problem then has symmetric and antisymmetric eigenfunctions with respect to $y = 0$, of which the symmetric one, $\widehat{v} = \cosh(\alpha y)$ is the well-known unstable Kelvin–Helmholtz sinuous deformation of the free shear layer (Drazin & Reid, 1981). The intermediate values of L_w connect these Kelvin–Helmholtz solutions with the stable ones of the impermeable case.

7.2 The turbulent channel profile

Although the analysis of the piecewise-linear profile provides qualitative information on the nature of the instability, quantitative comparison with the direct simulations requires more realistic velocity profiles. Following Reynolds & Hussain (1972), we have used the approximate profiles of Cess (1958) for turbulent channels at $\delta^+ = 185$, 550, 950 and 2000. The resulting growth rates and phase velocities are portrayed in figures 7.3(a) and 7.3(b) for different values of L_w. The results for the different Reynolds numbers are virtually indistinguishable when expressed in wall units, except perhaps for the $\delta^+ = 185$ case, for which the Cess approximation is less accurate. This is consistent with the scaling in wall units of the spanwise rollers discussed in §6.2. There is a sharp transition in the flow stability for $L_w^+ \approx 4$, below which the eigenmodes are quasi-neutral, and above which the maximum growth rate is nearly constant, as shown in figure 7.3(c). Using

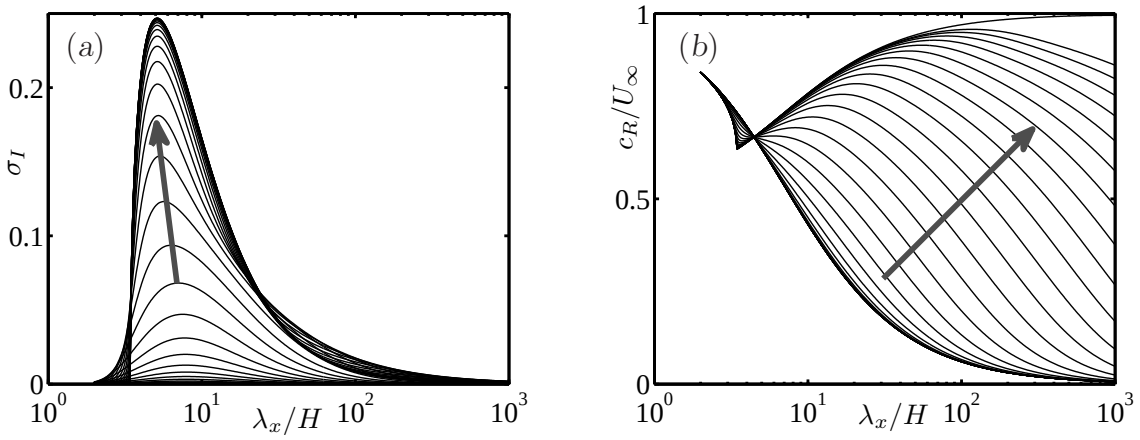

Figure 7.2: (*a*) Growth rate $\sigma_I = \mathbb{I}\mathrm{m}(\sigma)$ of the unstable modes given by equation (7.15), as a function of $\lambda_x/H = 2\pi/\widetilde{\alpha}$. (*b*) Corresponding phase velocities, $c_R/U_\infty = \mathbb{R}\mathrm{e}(\sigma)/\widetilde{\alpha}$. Curves are shown for values of $\Lambda = (L_w^3/\nu)(U_\infty\widetilde{\alpha}/H^2) = 10^{[-2(.2)3]}$ and 10^6, with the arrows indicating increasing Λ.

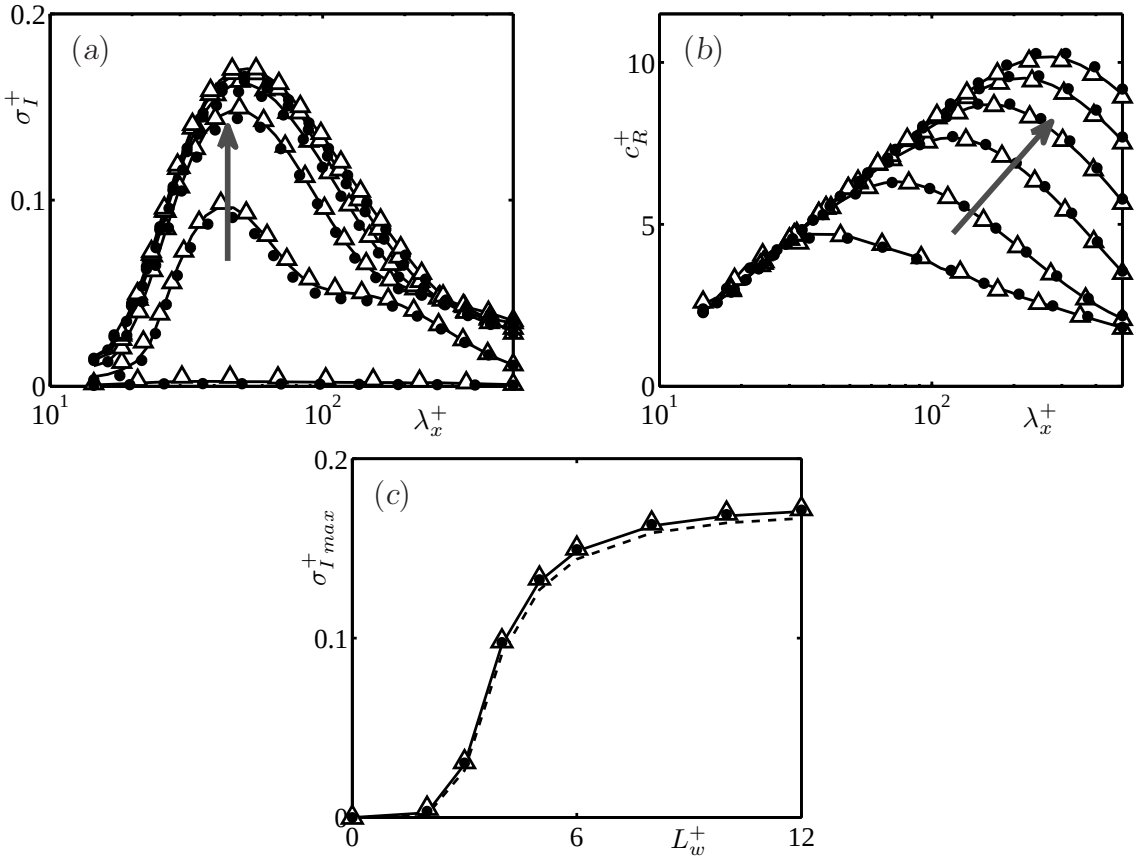

Figure 7.3: (*a*) Growth rate $\sigma_I^+ = \alpha^+\mathbb{I}\mathrm{m}(c^+)$ of the unstable modes of turbulent profiles with the boundary condition of equation (7.11). (*b*) Corresponding phase velocity, $\mathbb{R}\mathrm{e}(c^+) = c_R^+$. ●, $\delta^+ = 185$; ——, 550; △, 2000. Curves are shown for $L_w^+ = 2(2)12$, with arrows indicating increasing L_w^+. (*c*) Maximum growth rate as a function of L_w^+; - - - -, $\delta^+ = 185$; ——, 550; ●, 950; △, 2000.

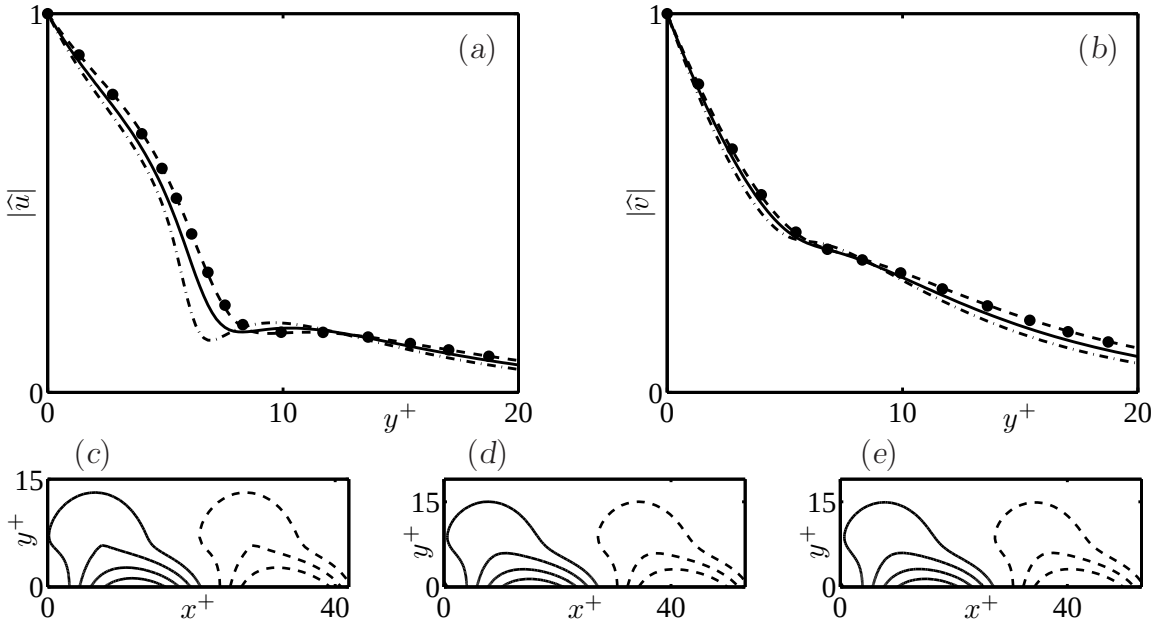

Figure 7.4: (a) $|\widehat{u}|$ and (b) $|\widehat{v}|$ profiles of the most amplified modes for a turbulent channel profile with $\delta^+ = 550$. -·-·-, $L_w^+ = 4$; ——, 6; - - - -, 8; ●, 14. (c–e) u–v perturbation streamlines of those modes, for (c) $L_w^+ = 4$, (d) 8, and (e) 14. The solid lines correspond to clockwise rotation.

the approximate relation (7.13), this transition roughly corresponds to $\ell_g^+ \approx 11$, which is close to the limit found in §2.2 for the breakdown of the viscous regime in the riblet experiments. The empirical collapse for ℓ_g^+ can thus be explained by the theoretical model for the instability, with the breakdown actually corresponding to the onset of the instability at $L_w^+ \approx 4$.

The growth rate and phase velocity curves of figure 7.3 are qualitatively similar to those for the piecewise-linear profile in figure 7.2, except for the shortest streamwise wavelengths at the largest L_w^+, which are stable in the piecewise-linear case, and weakly unstable in the channels. The reason is probably that those wavelengths are too short in the piecewise-linear case to interact with the singularity at $y = H$ of the profile of U'', which is the key energy-producing term in the Rayleigh equation (7.3). In the turbulent channels, U'' is non-zero everywhere .

On the other hand, the similarity of the eigenvalues for longer wavelengths suggests that the channels behave approximately as a piecewise-linear profile in which $H^+ \approx 10$. That is interesting, because it is slightly surprising that an instability derived from the inviscid Rayleigh equation should scale in viscous wall units. In fact, wall units are not only a measure of the Reynolds number of the perturbations, but they also encode the shape of the mean profile. Specifically, the energy-producing term, U'', has a fairly sharp

maximum between $y^+ = 5$ and 20 in channels, peaking near $y^+ = 7$, which plays the same role as the singularity at $y = H$ of the piecewise-linear profile. That peak scales in wall units and, in all probability, is responsible for the wall-scaling of the observed instability.

The most amplified modes for L_w^+ in the range of the onset of strong instability are portrayed in figure 7.4 for $\delta^+ = 550$, and are practically identical for the other Reynolds numbers. The rollers have heights of $y^+ \approx 15$, which agree well with the observations from our DNSs, and convection velocities $\mathbb{R}\mathrm{e}(c^+) \approx 6$, which are also in reasonable agreement with the observed $U_C^+ \approx 6-8$. Figure 7.4(c) shows how the perturbations penetrate below $y = 0$, as some of the DNS rollers of figure 5.15 do. On the other hand, the predicted streamwise wavelengths are twice shorter than the observed $\lambda_x^+ \approx 150$, probably because viscosity, which is absent in the model, damps the shorter wavelengths in the channel, shifting the maximum amplification towards longer waves.

7.3 Application to the optimization of fiber riblets

We mentioned in §2.2 that the scaling with ℓ_g^+ should not be expected to hold for unconventional geometries like the fibers proposed in §4.1.4. Indeed, the experiments of Bruse *et al.* (1993) with a single row of fibers, although inconclusive with respect to the size of breakdown, seem to suggest that s_{opt}^+ is much smaller than for conventional riblets. This agrees qualitatively with the scaling proposed in the present chapter with L_w. For a set of fibers with $h/s \approx 0.2$, the results of Bruse *et al.* suggest $s_{\mathrm{opt}}^+ \lesssim 10$, while for thin blades with roughly the same ratio $\ell_g/s \approx 0.45$, the optimum size is $s_{\mathrm{opt}}^+ \approx 25$ (Bechert *et al.*, 1997*b*). This difference is probably related to the disparity of L_w for the two geometries. The presence of full fences would offer more resistance to the longitudinal flow within the grooves than the fibers, leading to smaller penetration lengths. However, more detailed results on the breakdown sizes for fibers would be required to confirm this hypothesis.

Still, if we assume that the scaling with L_w^+ holds, we can determine from simple viscous simulations what the optimum arrangement of the fibers would be, whether they should be packed more densely in the spanwise or the wall normal direction. We have shown in §2.2, and illustrated in §4.1.1, that the protrusion height can provide a good estimate for $DR_{\max}$ when scaled with ℓ_g, at least for conventional riblets. According to the present discussion, the quantity to optimize would in fact be $\Delta h/L_w$. This is particularly useful for unconventional riblets like the fibers now considered, for which the scaling with ℓ_g^+ is not expected to hold. We can now use $\Delta h/L_w$ to improve the gross assumption

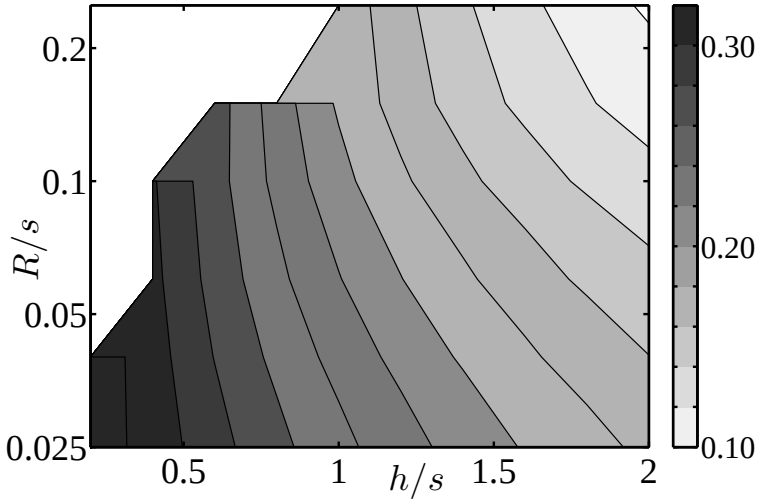

Figure 7.5: Protrusion height $\Delta h/L_w$ of fiber riblets as a function of the packing aspect ratio h/s and the fiber radius R/s.

that the optimum arrangement of the fibers would be for $h/s = 0.5$, made in §4.1.4 in the absence of tools for a finer estimation.

Before analyzing the optimum h/s, we must reconsider the optimum number of rows in the fiber layer. For $h/s = 0.5$, it was shown in §4.1.4 that $\Delta h/s$ remains mostly unaffected as the number of fiber rows increases, but the same is evidently not true for $\Delta h/L_w$. The pressure gradient of (7.5) would act across the full 'groove' cross-section, so fibers would not be as effective isolating the layer bottom as they are in the case of an outer shear. The penetration length L_w/s would then increase with the lining depth so, if $\Delta h/s$ remains essentially constant, $\Delta h/L_w$ must necessarily decrease. We can therefore conclude that the number of rows should be small to yield a significant $\Delta h/L_w$. Since a single row of fibers was shown by Bruse *et al.* (1993) to give modest drag reductions, we have assumed that two staggered rows of fibers would be closer to the optimum, and have restricted our analysis to these setups.

The results for a range of fiber radii R/s and packing aspect ratios h/s are compiled in figure 7.5. The figure shows that the highest $DR_{\max}$, which should be directly proportional to $\Delta h/L_w$, would be achieved for low h/s, and in that case the influence of the fiber radius is surprisingly small. From our analysis, we conclude that a good compromise between feasible fibers and good performance would be $h/s = 0.4 - 0.5$ and $R/s = 0.1$, yielding a protrusion height $\Delta h/L_w \approx 0.30$. This would be less than the value for the optimal blades of Bechert *et al.* (1997*b*), $\Delta h/L_w \approx 0.42$, but similar to that for their optimal trapezes. However, fibers would not be as sensitive to erosion as conventional sharp riblets, for which the effect of tip rounding was discussed in §4.1.2.

Chapter 8

Conclusions and future work

The present thesis has analyzed the interaction of a riblet surface with the overlying turbulent flow, and its impact on drag reduction. It was already known that the reduction scales with the riblet size, expressed in wall units. The limit of vanishing riblet spacing, or 'viscous regime', in which the drag reduction produced by the riblets is proportional to their size, had also been well understood. However, the nature of the breakdown of that regime for larger sizes, which ultimately limits the optimum performance of a given riblet, had up to now remained an open question. The physics involved in that breakdown have been the central subject of our study.

To approach the problem, we have first reviewed and reassessed the available experimental data and theoretical understanding. This analysis has led to two conclusions. The first is that the drag reduction curve of a given riblet is not universal, since it is modulated by the Reynolds number of the overlying flow. According to the classical theory of turbulence, the direct effect of any surface manipulation on the flow is not a change in friction, but a shift in the mean velocity profile, provided that the manipulations do not protrude into the flow a distance comparable to its thickness. The change in the friction is actually derived from this shift with some elemental algebra. If both are small, as is the case of riblets, a proportional law can be derived, but the coefficient of proportionality turns out to depend, though weakly, on the Reynolds number, through the friction coefficient of the unperturbed flow. This effect should be considered when comparing results from different experiments, or when trying to reduce laboratory data for its industrial application.

The relationship between the shift in the velocity profile and the drag reduction enables the connection of experimental results in the viscous regime with the concept of protrusion height, first proposed by Bechert & Bartenwerfer (1989) and later refined by Luchini *et al.* (1991). These authors proposed that, for vanishingly small riblets, their effect on the flow

is an offset between the 'virtual' origins that the mean streamwise flow and the secondary crossflow see. That offset was proven by Jiménez (1994) to be proportional to the shift in the velocity profile, with a constant of proportionality that can be assumed universal. The offset, or protrusion height, is a geometrical property of each riblet design, and can be calculated from two-dimensional, steady, Stokes-flow simulations, which are both simple and inexpensive.

Thus, the performance of riblets in the viscous regime can be easily predicted solely from their geometry and the flow Reynolds number. The problem of such predictions is that they are not directly extrapolable to the regime of optimum performance, which roughly coincides with the viscous breakdown, and which is after all the interesting regime from a technological perspective. The reason is that the size of breakdown, traditionally given in terms of the peak-to-peak spacing s^+, varies greatly from one geometry to another.

The second conclusion from the analysis of the data in the literature is that s^+ is probably not the best scale for the riblet size. The wide range of optimum spacings for the different geometries reviewed, $s^+ = 10-20$, implies that the spacing is only weakly related to the mechanism of the breakdown. We have examined other possible scales for the riblet dimension, finding that the scaling with the square root of the groove cross-section, $\ell_g^+ = \sqrt{A_g^+}$, produces a significantly better collapse of the different regimes in the drag curves of different riblets. In particular, the optimum is achieved for a common $\ell_g^+ \approx 11$. This result suggests that the groove cross-section is somehow related to the breakdown, at least for the conventional geometries for which most experiments are available.

The collapse of the drag regimes with ℓ_g^+ permits the extrapolation of viscous regime results into the optimum range. For instance, the rounding of riblet peaks can greatly alter the viscous performance, but it does not modify the groove cross-section significantly. Therefore, the optimum size of a riblet should be independent of the rounding, and the variation in the optimum performance would be exclusively due to the variation in the protrusion height. Surprisingly, blade riblets with thick, flat-top fences experience a slight improvement in performance when the corners of their tips are eroded.

In general, if the protrusion heights are normalized with ℓ_g instead of s, they should be directly proportional to the maximum drag reduction. From the fit of experiments we propose $DR_{\max} \approx 8.9\, m_\ell$, where m_ℓ is the slope of the drag curve in the viscous regime, related to the protrusion height by equation (2.10). The new scaling presents a great advantage from a design perspective, since it enables the approximate prediction of $DR_{\max}$ solely from Stokes regime computations. For instance, the protrusion heights $\Delta h/s$ of trapezoidal and blade riblets increase asymptotically with the aspect ratio of the

riblets, h/s, while $DR_{\max}$ reaches a maximum for $h/s \approx 0.5$. With the rescaling $\Delta h/\ell_g$, the protrusion heights follow closely the behavior of $DR_{\max}$, and also reach a maximum for $h/s \approx 0.5$. The riblet designer should then simply aim at maximizing $\Delta h/\ell_g$.

Beyond the analysis of the available experiments, the DNS of channels with riblet-covered walls has proven an invaluable tool to unravel the physical processes involved in the breakdown. Following Choi *et al.* (1993) and Goldstein *et al.* (1995), we have calculated the mean flows conditioned to the position above the riblet unit. From them, we have obtained some interesting conclusions. The first one is that vortices do not begin to lodge within the grooves past the riblet size of breakdown. That lodging was proposed by some authors (Choi *et al.*, 1993; Lee & Lee, 2001) as the cause for the increase in drag for large riblets. We have found that, although some lodging may appear for very large riblets, it is clear from our DNSs that it is not the cause of the breakdown, and could rather be a consequence of it. Nevertheless, we have observed that vortices tend to be localized above the riblet valleys, and more so with increasing ℓ_g^+. The localization is only significant for sizes past the viscous regime, which would contradict the assertion that it is part of the drag reduction mechanism (Choi, 1989; Goldstein *et al.*, 1995; Goldstein & Tuan, 1998). The other interesting conclusion is that the crossflow within the grooves is always weak, and the mean streamwise velocity follows very closely that of the viscous limit. This result has later been used to develop a linear stability model for the outer flow. Since the flow within the grooves remains essentially unperturbed throughout the whole drag reducing range of ℓ_g^+, all the changes must take place above the riblet peaks. In particular, we have measured the Reynolds stress immediately above the riblets, and have detected strong increases once the size is larger than the optimum.

The most interesting conclusions from the DNS results have been obtained by spectral analysis. We have found coherent spanwise structures, immediately above the riblets and with y-heights not longer than 20 wall units, that begin to appear for sizes near the optimum. Once the riblet size is large enough to trigger the appearance of these structures, they grow in intensity with ℓ_g^+, but their size is essentially constant and scales in wall units. The typical streamwise wavelengths are $\lambda_x^+ \approx 150$, and in the spanwise direction they extend over several riblets, with wavelengths ranging from $\lambda_z^+ \approx 100$ to ≈ 2000. These are the structures responsible for the extra Reynolds stress mentioned in the previous paragraph.

The change in drag can be separated into three contributions. One is related to the apparent slip at the riblet-peak plane. Because of the self similarity of the flow within the grooves, this term is proportional to the riblet size, and always produces a drag

decrease. The second term is a factor owing to the different flow conditions in the different simulations. Its contribution is small, and should vanish for large Reynolds number. The final term is related to the additional Reynolds stress across the whole channel due to the presence of the riblets. This term is negligible for riblet sizes smaller than the optimum, and increases rapidly for larger ones. The spanwise structures contribute to roughly 70% of it, suggesting that they are indeed responsible for the viscous breakdown.

The structures appear in the flow as rollers, similar to those reported over plant canopies (Raupach *et al.*, 1996; Finnigan, 2000), and over permeable (Jiménez *et al.*, 2001) and porous walls (Breugem *et al.*, 2006). They have been typically attributed to Kelvin–Helmholtz-like instabilities of the mean streamwise flow, due to the relaxation of the impermeability condition at the wall.

Based on the above results, we have developed a simplified stability model that attempts to capture the essential physics involved, including the effect of the riblet geometry on the instability. The details of the method deserve some comment. Since the spanwise rollers are quasi-two-dimensional in the streamwise and wall-normal directions, the model omits the spanwise component. The viscous terms are also neglected, because Kelvin–Helmholtz-like solutions are expected to be essentially inviscid instabilities, on which viscosity would only have a damping effect. The presence of the riblets is reproduced in a spanwise-averaged sense by z-independent boundary conditions, thus preserving the two-dimensionality of the model. The boundary conditions are constructed based on the character of the flow within the grooves observed in the DNSs, which as we have mentioned follows very closely the Stokes approximation, even for the larger riblets. We therefore suppose a Poiseuille-like flow, induced by streamwise pressure oscillations that are uniform in the groove section. The connection with the outer flow is derived from the streamwise variation of the mass-flow, which must be compensated by the exchange of mass at the riblet-peak plane. This plane represents the interface between the flow within the grooves and the outer one, and is also where the boundary conditions for the inviscid model are imposed. The exchange of mass, together with the other flow variables, is averaged over the plane to obtain the boundary condition sought. The resulting equation introduces a new parameter into the stability equations. The parameter is a 'penetration length' that measures how easily can the flow advance through the grooves.

According to this simplified inviscid model, it would appear that all the viscous effects are confined to the grooves, but that is not entirely true. The relative importance of viscosity in the outer flow expresses itself through the mean velocity profile, determining the length scales of the instability. That is the reason for the scaling of the spanwise

rollers in wall units.

The model can be applied to a piecewise linear profile which, although unphysical, produces pseudo-analytical solutions for the instability. These solutions allow for a qualitative analysis of the system, and provide some interesting general conclusions. Specifically, it is shown that for very large values of the penetration length the original Kelvin–Helmholtz equations are recovered. This proves that the instability over the riblets is indeed related to the canonical free-shear instability. When the model is applied to more realistic turbulent profiles, the unstable modes obtained agree reasonably well with the observed wavelengths and shapes of the perturbation.

The most interesting result of the stability analysis is that the onset of the instability depends critically on the value of the penetration length, measured in wall units. For conventional riblets, that parameter turns out to be essentially proportional to the empirical parameter ℓ_g^+, which was previously found to characterize the breakdown. Even more, the value for which the instability sets on corresponds to the value of ℓ_g^+ observed in experiments for the viscous breakdown. Such a precise coincidence in the results may however be accidental, given the simplicity of the instability model that we propose. A vaguer agreement was to be expected, and would also have been satisfactory.

The identification of the breakdown of the viscous regime as an effect of an instability of the outer flow, triggered by its ability to penetrate the riblet grooves, and with well defined streamwise wavelengths, opens some promising paths for the design of novel configurations, with delayed breakdowns and higher $DR_{\max}$. For instance, geometries that are relatively permeable to the shear flow that defines the protrusion height, but offer more resistance to pressure-driven ones, should be investigated.

Another interesting path for research are sinusoidal riblets. So far, such riblets have not been able to yield better performances than their streamwise-uniform counterparts (Kramer *et al.*, 2010), but that is probably because they have been designed attempting to emulate the drag-reducing properties of oscillating walls (Viotti *et al.*, 2009). The oscillation induced by sinusoidal riblets on the flow is too weak to produce an oscillating-wall effect. However, sinusoidal riblets could also be designed with shorter wavelengths, comparable to those of the rollers. That way, they could probably be able to interfere with the onset of the instability and delay the formation of rollers, and the breakdown of the viscous regime, with a mechanism completely different to that of the oscillating wall.

References

del Álamo, J. C. & Jiménez, J. 2003 Spectra of the very large anisotropic scales in turbulent channels. *Phys. Fluids* **15**, L41–L44.

del Álamo, J. C. & Jiménez, J. 2009 Estimation of turbulent convection velocities and corrections to Taylor's approximation. *J. Fluid Mech.* **640**, 5–26.

Batchelor, G. K. 1994 *An Introduction to Fluid Dynamics*. Cambridge University Press.

Bechert, D. W. & Bartenwerfer, M. 1989 The viscous flow on surfaces with longitudinal ribs. *J. Fluid Mech.* **206**, 105–129.

Bechert, D. W., Bruse, M., Hage, W. & Meyer, R. 1997*a* Biological surfaces and their technological application – Laboratory and flight experiments on drag reduction and separation control. *AIAA Paper* 97-1960.

Bechert, D. W., Bruse, M., Hage, W., Van der Hoeven, J. G. T. & Hoppe, G. 1997*b* Experiments on drag-reducing surfaces and their optimization with adjustable geometry. *J. Fluid Mech.* **338**, 59–87.

Breugem, W. P., Boersma, B. J. & Uittenbogaard, R. E. 2006 The influence of wall permeability on turbulent channel flow. *J. Fluid Mech.* **562**, 35–72.

Bruse, M., Bechert, D. W., Van der Hoeven, J. G. T., Hage, W., & Hoppe, G. 1993 Experiments with conventional and with novel adjustable drag-reducing surfaces. In *Near-Wall Turbulent Flows* (ed. R. M. C. So, C. G. Speziale & B. E. Launder), pp. 719–738. Elsevier.

Bushnell, D. M. 2003 Aircraft drag reduction – A review. *Proc. Instn Mech. Engrs* **217** (G1), 1–18.

Cess, R. D. 1958 A survey of the literature on heat transfer in turbulent tube flow. Report 8-0529-R24. Westinghouse Research.

Choi, H., Moin, P. & Kim, J. 1992 Turbulent drag reduction: studies of feedback control and flow over riblets. PhD thesis, Stanford University.

Choi, H., Moin, P. & Kim, J. 1993 Direct numerical simulation of turbulent flow over riblets. *J. Fluid Mech.* **255**, 503–539.

Choi, H., Moin, P. & Kim, J. 1994 Active turbulence control and drag reduction in wall-bounded flows. *J. Fluid Mech.* **262**, 75–110.

Choi, K.-S. 1989 Near-wall structure of a turbulent boundary layer with riblets. *J. Fluid Mech.* **208**, 417–458.

Choi, K.-S. 2000 European drag-reduction research – Recent developments and current status. *Fluid Dynamics Research* **26**, 325–335.

Chu, D. C. & Karniadakis, G. E. M. 1993 A direct numerical simulation of laminar and turbulent flow over riblet-mounted surfaces. *J. Fluid Mech.* **250**, 1–42.

Clauser, F.H. 1956 The turbulent boundary layer. *Adv. Appl. Mech.* **4**, 1–51.

Coustols, E. & Savill, A. M. 1992 Turbulent skin-friction drag reduction by active and passive means: Part I. In *Skin friction drag reduction*, *AGARD Rep.* 786, pp. 8.1–8.53.

Dean, R. B. 1978 Reynolds number dependence of skin friction and other bulk variables in two-dimensional rectangular duct flow. *J. Fluids Engineering* **100**, 215–223.

Debisschop, J. R. & Nieuwstadt, F. T. M. 1996 Turbulent boundary layer in an adverse pressure gradient: Effectiveness of riblets. *AIAA J.* **34** (5), 932–937.

Drazin, P. G. & Reid, W. H. 1981 *Hydrodinamic Stability*. Cambridge University Press.

El-Samni, O. A., Chun, H. H. & Yoon, H. S. 2007 Drag reduction of turbulent flow over thin rectangular riblets. *Int. J. Eng. Sci.* **45**, 436–454.

Fadlun, E. A., Verzicco, R., Orlandi, P. & Mohd-Yusof, J. 2000 Combined immersed-boundary finite-difference methods for three-dimensional complex flow simulations. *J. Comput. Phys.* **161**, 35–60.

Ferziger, J. H. & Perić, M. 1996 *Computational Methods for Fluid Dynamics*. Springer.

Finnigan, J. 2000 Turbulence in plant canopies. *Ann. Rev. Fluid Mech.* **32**, 519–571.

García-Mayoral, R. & Jiménez, J. 2007 On the effect of riblet geometry on drag reduction. *Tech. Rep.* ETSIA/MF-072. School of Aeronautics, Universidad Politécnica de Madrid.

García-Mayoral, R. & Jiménez, J. 2011*a* Drag reduction by riblets. *Phil. Trans. R. Soc. A* **369**, 1412–1427.

García-Mayoral, R. & Jiménez, J. 2011*b* Hydrodynamic stability and breakdown of the viscous regime over riblets. *J. Fluid Mech.* doi: 10.1017/jfm.2011.114.

Ghisalberti, M. 2009 Obstructed shear flows: similarities across systems and scales. *J. Fluid Mech.* **641**, 51–61.

Goldstein, D. B., Handler, R. & Sirovich, L. 1995 Direct numerical simulation of turbulent flow over a modeled riblet covered surface. *J. Fluid Mech.* **302**, 333–376.

Goldstein, D. B. & Tuan, T. C. 1998 Secondary flow induced by riblets. *J. Fluid Mech.* **363**, 115–151.

Grüneberger, R. & Hage, W. 2011 Drag characteristics of longitudinal and transverse riblets at low dimensionless spacings. *Exp. in Fluids* **50**, 363–373.

Hage, W., Bechert, D. W. & Bruse, M. 2000 Yaw angle effects on optimized riblets. In *Proc. of the CEAS/DragNet European Drag Reduction Conf.* (ed. P. Thiede), pp. 278–285. Potsdam, Germany: Springer-Verlag.

Hahn, S., Je, J. & Choi, H. 2002 Direct numerical simulation of a turbulent channel flow with permeable walls. *J. Fluid Mech.* **450**, 259–285.

Hoyas, S. & Jiménez, J. 2006 Scaling of the velocity fluctuations in turbulent channels up to $\mathrm{Re}_\tau = 2003$. *Phys. Fluids* **18**, 011702.

Hoyas, S. & Jiménez, J. 2008 Reynolds number effects on the Reynolds-stress budgets in turbulent channels. *Phys. Fluids* **20**, 101511.

Iaccarino, G. & Verzicco, R. 2003 Immersed boundary technique for turbulent flow simulations. *Appl. Mech. Rev.* **56** (3), 331–347.

Itoh, M., Tamano, S., Iguchi, R., Yokota, K., Akino, N., Hino, R. & Kubo, S. 2006 Turbulent drag reduction by the seal fur surface. *Phys. Fluids* **18** (6), 065102.

Jiménez, J. 1992 Wall friction and the structure of near-wall turbulence. In *11th Australasian Fluid Mech. Conf.* (ed. M.R. Davis & G.J. Walker), pp. 813–816. Hobart, Australia.

Jiménez, J. 1994 On the structure and control of near wall turbulence. *Phys. Fluids* **6** (2), 944–953.

Jiménez, J. 2004 Turbulent flows over rough walls. *Ann. Rev. Fluid Mech.* **36**, 173–196.

Jiménez, J. & Moin, P. 1991 The minimal flow unit in near-wall turbulence. *J. Fluid Mech.* **225**, 213–240.

Jiménez, J. & Pinelli, A. 1999 The autonomous cycle of near wall turbulence. *J. Fluid Mech.* **389**, 335–359.

Jiménez, J., Uhlman, M., Pinelli, A. & G., Kawahara 2001 Turbulent shear flow over active and passive porous surfaces. *J. Fluid Mech.* **442**, 89–117.

Jung, W.J., Mangiavacchi, N. & Akhavan, R. 1992 Suppression of turbulence in wall-bounded flows by high-frequency spanwise oscillations. *Phys. Fluids A* **4**, 1605–1607.

Kim, J., Moin, P. & Moser, R. D. 1987 Turbulence statistics in fully developed channel flow at low Reynolds number. *J. Fluid Mech.* **177**, 133–166.

Kong, F.Y. & Schetz, J.A. 1982 Turbulent boundary layer over porous surfaces with different geometries. *AIAA Paper* 82-0030.

Kramer, F., Grüneberger, R., Thiele, F., Wassen, E., Hage, W. & Meyer, R. 2010 Wavy riblets for turbulent drag reduction. In *Proc. of 5th AIAA Flow Control Conf*. Chicago, Illinois, USA: AIAA.

Kramer, M. O. 1937 Einrichtung zur Verminderung des Reibungswiderstandes, Patentschrift 669897, Klasse 62b, Gruppe 408. March 17 .

Krieger, K. 2004 Do pool sharks really swim faster? *Science* **305**, 636–637.

Le, H. & Moin, P. 1991 An improvement of fractional step methods for the incompressible Navier-Stokes equations. *J. Comput. Phys.* **92** (2), 369–379.

Lee, S.-J. & Jang, Y.-G. 2005 Control of flow around a NACA 0012 airfoil with a micro-riblet film. *J. Fluids Struct.* **20**, 659–672.

Lee, S.-J. & Lee, S.-H. 2001 Flow field analysis of a turbulent boundary layer over a riblet surface. *Exp. Fluids* **30**, 153–166.

Linnick, M. N. & Fasel, H. F. 2005 A high-order immersed interface method for simulating unsteady incompressible flows on irregular domains. *J. Comput. Phys.* **204** (1), 157–192.

Luchini, P. 1995 Asymptotic analysis of laminar boundary-layer flow over finely grooved surfaces. *Eur. J. Mech. B/Fluids* **14**, 169–195.

Luchini, P., Manzo, F. & Pozzi, A. 1991 Resistance of a grooved surface to parallel flow and cross-flow. *J. Fluid Mech.* **228**, 87–109.

Marinho, D. A., Reis, V. M., Alves, F. B., Vilas-Boas, J. P., Machado, L., Silva, A. J. & Rouboa, A. I. 2009 The hydrodynamic drag during gliding in swimming. *J. Appl. Biomech.* **25**, 253–257.

Matthews, J. N. A. 2008 Low-drag suit propels swimmers. *Physics Today* **August**, 32–33.

Mohd-Yusof, J. 1997 Combined immersed-boundary/B-spline methods for simulations of flow in complex geometries. *Annual Research Briefs CTR* pp. 317–328.

Moser, R. D., Kim, J. & Mansour, N. N. 1999 Direct numerical simulation of turbulent channel flow up to $\mathrm{Re}_\tau = 590$. *Phys. Fluids* **11**, 943.

Nördstrom, J., Mattsson, K. & Swanson, C. 2007 Boundary conditions for a divergence free velocity-pressure formulation of the Navier-Stokes equations. *J. Comput. Phys.* **225**, 874–890.

Orlandi, P. 2000 *Fluid Flow Phenomena – A Numerical Toolkit*. Kluwer Academic Publishers.

Orlandi, P. & Jiménez, J. 1994 On the generation of turbulent wall friction. *Phys. Fluids* **6**, 634–641.

Orlandi, P., Leonardi, S. & Antonia, R. A. 2006 Turbulent channel flow with either transverse or longitudinal roughness elements on one wall. *J. Fluid Mech.* **561**, 279–305.

Park, S.-R. & Wallace, J. M. 1994 Flow alteration and drag reduction by riblets in a turbulent boundary layer. *AIAA J.* **32** (1), 31–38.

Peskin, C. S. 1972 Flow patterns around heart valves: A numerical method. *J. Comput. Phys.* **10** (2), 252–271.

Py, C., de Langre, E. & Moulia, B. 2006 A frequency lock-in mechanism in the interaction between wind and crop canopies. *J. Fluid Mech.* **568**, 425–449.

Raupach, M. R., Finnigan, J. & Brunet, Y. 1996 Coherent eddies and turbulence in vegetation canopies: the mixing-layer analogy. *Boundary-Layer Meteorol.* **78**, 351–382.

Reynolds, W. C. & Hussain, A. K. M. F. 1972 The mechanics of an organized wave in turbulent shear flow. Part 3. Theoretical models and comparisons with experiments. *J. Fluid Mech.* **54**, 263–288.

Robert, J. F. 1992 Drag reduction: an industrial challenge. In *Skin friction drag reduction*, *AGARD Rep.* 786, pp. 2.1–2.15.

Roshko, A. 1953 On the development of turbulent wakes from vortex streets. NACA Tech. Note 2913.

Roskam, J. 1987 *Airplane design. Part VI: Preliminary calculation of aerodynamic, thrust and power characteristics*. Roskam Aviation and Engineering Corporation.

Sha, T., Itoh, M., Tamano, S., Yokota, K. & Akino, N. 2005 Experimental study on drag reduction in turbulent flow on zigzag riblet surface. *Fluids Eng. Conf./Ryutai Kogaku Bumon Koenkai Koen Ronbunshu* **83**, 207.

Simens, M. P., Jiménez, J., Hoyas, S. & Mizuno, Y. 2009 A high-resolution code for turbulent boundary layers. *J. Comput. Phys.* **228**, 4218–4231.

Smits, A. J. & Wood, D. H. 1985 The response of turbulent boundary layers to sudden perturbations. *Ann. Rev. Fluid Mech.* **17**, 321–358.

Spalart, P. R. & McLean, J. D. 2011 Drag reduction: enticing turbulence, and then an industry. *Phil. Trans. R. Soc. A* **369**, 1556–1569.

Stalio, E. & Nobile, E. 2003 Direct numerical simulation of heat transfer over riblets. *Int. J. Heat Fluid Flow* **24**, 356–371.

Suzuki, Y. & Kasagi, N. 1994 Turbulent drag reduction mechanism above a riblet surface. *AIAA J.* **32** (9), 1781–1790.

Szodruch, J. 1991 Viscous drag reduction on transport aircraft. *AIAA Paper* 91-0685.

Tennekes, H. & Lumley, J. L. 1972 *A First Course in Turbulence*. MIT Press.

Tseng, Y.-H. & Ferziger, J. H. 2003 A ghost-cell immersed boundary method for flow in complex geometry. *J. Comput. Phys.* **192** (2), 593–623.

Viotti, C., Quadrio, M. & Luchini, P. 2009 Streamwise oscillation of spanwise velocity at the wall of a channel for turbulent drag reduction. *Phys. Fluids* **21**, 115109.

Viswanath, P. R. 2002 Aircraft viscous drag reduction using riblets. *Progress in Aerospace Sciences* **38**, 571–600.

Vukoslavcevic, P., Wallace, J. M. & Balint, J.-L. 1992 Viscous drag reduction using streamwise aligned riblets. *AIAA J.* **30**, 1119–1122.

Walsh, M. J. 1982 Turbulent boundary layer drag reduction using riblets. *AIAA Paper* 82-0169.

Walsh, M. J. 1990*a* Effect of detailed surface geometry on riblet drag reduction performance. *J. Aircraft* **27** (6), 572–573.

Walsh, M. J. 1990*b* Riblets. In *Viscous Drag Reduction in Boundary Layers* (ed. D. M. Bushnell & J. N. Hefner), pp. 203–261. AIAA.

Walsh, M. J. & Lindemann, A. M. 1984 Optimization and application of riblets for turbulent drag reduction. *AIAA Paper* 84-0347.

Wassen, E., Grueneberger, R., Kramer, F., Hage, W., Meyer, R. & Thiele, F. 2008 Turbulent drag reduction by oscillating riblets. In *Proc. of 4th AIAA Flow Control Conf*. Seattle, Washington, USA: AIAA.

Williamson, C. H. K. 1989 Oblique and parallel modes of vortex shedding in the wake of a circular cylinder at low Reynolds numbers. *J. Fluid Mech.* **206**, 579–627.